

THE EFFECTS OF INLET TEMPERATURE AND TURBULENCE  
CHARACTERISTICS ON THE FLOW DEVELOPMENT INSIDE A GAS  
TURBINE EXHAUST DIFFUSER

by

Christian Loangola Bomela

A dissertation submitted to the faculty of  
The University of North Carolina at Charlotte  
in partial fulfillment of the requirements  
for the degree of Doctor of Philosophy in  
Mechanical Engineering

Charlotte

2014

Approved by:

---

Dr. Mesbah Uddin

---

Dr. Peter T. Tkacik

---

Dr. Edward B. Stokes

---

Dr. Russell G. Keanini

---

Dr. Kimberly Warren

©2014  
Christian Loangola Bomela  
ALL RIGHTS RESERVED

## ABSTRACT

CHRISTIAN LOANGOLA BOMELA. The effects of inlet temperature and turbulence characteristics on the flow development inside a gas turbine exhaust diffuser. (Under the direction of DR. MESBAH UDDIN)

The overall industrial gas turbine efficiency is known to be influenced by the pressure recovery in the exhaust system. The design and, subsequently, the performance of an industrial gas turbine exhaust diffuser largely depend on its inflow conditions dictated by the turbine last stage exit flow state and the restraints of the diffuser internal geometry. Recent advances in Computational Fluid Dynamics (CFD) tools and the availability of computer hardware at an affordable cost made the virtual tool a very attractive one for the analysis of fluid flow through devices like a diffuser. In this backdrop, CFD analyses of a typical industrial gas turbine hybrid exhaust diffuser, consisting of an annular diffuser followed by a conical portion, have been carried out with the purpose of improving the performance of these thermal devices using an open-source CFD code "OpenFOAM". The first phase in the research involved the validation of the CFD approach using OpenFOAM by comparing CFD results against published benchmark experimental data. The numerical results closely captured the flow reversal and the separated boundary layer at the shroud wall where a steep velocity gradient has been observed. The standard  $k - \epsilon$  turbulence model slightly over-predicted the mean velocity profile in the casing boundary layer while slightly under-predicted it in the reversed flow region. A reliable prediction of flow characteristics in this region is very important as the presence of the annular diffuser inclined wall has the most dominant effect on the downstream flow development. The

core flow region and the presence of the hub wall have only a minor influence as reported by earlier experimental studies. Additional simulations were carried out in the second phase to test the veracity of other turbulence models; these include RNG  $k-\epsilon$ , the SST  $k-\omega$ , and the Spalart-Allmaras turbulence models. It was found that a high resolution case with 47.5 million cells using the SST  $k-\omega$  turbulence model produced a mean flow velocity profile at the middle of the annular diffuser portion that had the best overall match with the experiment. The RNG  $k-\epsilon$ , however, better predicted the diffuser performance along the exhaust diffuser length by means of the pressure recovery coefficient. These results were obtained using uniform inflow conditions and steady-state simulations. As such, the last phase of our investigations involved varying the inflow parameters like the turbulence intensity, the inlet flow temperature, and the flow angularity, which constitute important characteristics of the turbine blade wake, to investigate their impact on the diffuser design and performance. These isothermal CFD simulations revealed that changing the flow temperature from 15 to 427°C did not affect the pressure recovery coefficient. Furthermore, it has been shown that the increase of temperature had no effects on the size of the reversed flow region and the thickness of the separated casing boundary layer, although the flow appears to be more turbulent. It has been established that an optimum turbulence intensity of about 4% produced comparable diffuser performance as the experiment. We also found that a velocity angle of about 2.5° at the last turbine stage will ensure a better exhaust diffuser performance for the investigated diffuser.

## ACKNOWLEDGMENTS

I would like first and foremost to thank my advisor, Professor Dr. Mesbah Uddin, for his guidance, continued support, professional expertise, and for introducing me to the scientific research world. It has been a great pleasure to be his first Ph.D. student. His advice on both academic and personal levels have been invaluable, for which I am extremely grateful. I would also like to thank my committee members, starting with Professor Dr. Russell Guy Keanini, who impacted my graduate school experience and shaped my character with his advices, Professor Dr. Peter T. Tkacik for his academic support, Professor Dr. Edward B. Stokes, and Professor Dr. Kimberly Warren for serving as my committee members despite their multiple occupations.

This dissertation would not have been possible without the generous funding supports from the Energy Production and Infrastructure Center (EPIC) for its 2012-13 Research Assistantship, and would like to personally thank its director, Professor Dr. Johan Enslin for his support, and the graduate school through the Lucille P. and Edward C. Giles Dissertation-Year Graduate Fellowship that allowed me to focus on my dissertation writing. I would like also to acknowledge the financial, academic and technical support of the William States Lee College of Engineering through its Mechanical Engineering and Engineering Science department. I would like also to extend my gratitude to Professor Dr. Robin N. Coger, Professor Dr. Gloria D. Elliot, and Professor Dr. Terence J. Fagan for their invaluable advice and mentorship.

A special thanks to my whole family. Words cannot express how grateful I am to my wife, Irene Kalongo Lumba-Bomela, for her patience, unremitting support,

and sacrifices during these years, and for giving me two beautiful girls, Chrissie Lumba Bomela and Chrissabella Naomie-Zaga Bomela. I would like also to thank my smartest girl Kerene Tolongi Bomela for being a good example for her sisters, Nadia Asongila Bomela, Walter Botongo Bomela, and Yalinde-Olga Zaga Bomela for the love and support they share every day. Big thanks to my parents, Maman Naume Zaga Angwele and my father Papa Mathias Botongo Bomela, for all of the sacrifices that you have made on my behalf, your love, education, and prayer that sustained me during all these years and shaped my life today.

Lastly but not least, I would like to thank God, the Almighty, for the strength and wisdom he has bestowed on me. He is always there when big changes come to my life and when I need him the most.

## TABLE OF CONTENTS

LIST OF FIGURES	x
LIST OF TABLES	xiv
CHAPTER 1: INTRODUCTION	1
1.1. Research Problem	1
1.2. Research Motivation and Background	2
1.3. The Value of Numerical Methods in CFD Applications	6
1.4. Goals and Objectives	7
1.5. Outcomes	9
1.6. Thesis Outline	11
CHAPTER 2: LITERATURE REVIEW	13
CHAPTER 3: THEORETICAL FRAMEWORK	34
3.1. Governing Equations of Fluid Flow	34
3.1.1. Introduction	34
3.1.2. Incompressible Flow	36
3.1.3. Viscous Fluid Flow Boundary Conditions	38
3.2. Gas Turbines	38
3.2.1. Gas Turbine Composition	38
3.2.2. Diffusers	39
3.3. Boundary Layer Characteristics	50
3.3.1. Boundary Layer Separation or Stall	50
3.3.2. Diffuser Flow Regimes	52

3.4. The Effects of Diffuser Inlet Flow Conditions	53
3.4.1. The Influence of Swirl	53
3.4.2. The Reynolds Number Influence	54
3.4.3. The Turbulence Influence	54
3.4.4. The Mach Number Influence	55
3.5. The Engineering Design Process	55
3.5.1. Design General Considerations	55
3.5.2. Diffuser Types	59
3.5.3. The Analysis Phase	62
3.6. Turbulence Modeling	63
3.6.1. Turbulence Definition	63
3.6.2. Time-Averaged N.-S. Equations	64
3.6.3. The Modeling of Turbulence	65
3.7. Numerical Modeling	79
3.7.1. Mesh Generation	80
3.7.2. Discretization	81
3.7.3. Solution of Discretized Equations	86
CHAPTER 4: METHODOLOGY	90
4.1. Research Workflow Procedure	90
4.2. Simulation Implementation	91
4.2.1. Pre-processing	92
4.2.2. Analysis or Solution	102
4.2.3. Post-processing	105

4.3. Additional Simulations with Selected Inflow Characteristics	108
CHAPTER 5: RESULTS AND DISCUSSION	111
5.1. Flow Development	112
5.2. The Effects of Mesh Resolution on the Flow Characteristics	127
5.3. The Effects of Turbulence Model on the Flow Characteristics	131
5.4. The Effects of Inlet Turbulence Intensity Variations on the Flow Characteristics	148
5.5. The Effects of Inlet Temperature on the Flow Characteristics	153
5.6. The Effects of Velocity Inlet Angle on the Flow Characteristics	160
CHAPTER 6: CONCLUSIONS	167
6.1. Research Limitations	169
6.2. Key Findings and Concluding Remarks	170
6.3. Recommendations for Future Research	175
REFERENCES	178

## LIST OF FIGURES

FIGURE 1: Natural gas price trend (US Energy Information Administration, eia)	3
FIGURE 2: History of energy consumption in the US from 1776-2012 (US Energy Information Administration, eia)	4
FIGURE 3: Energy consumption by source in US (US Energy Information Administration, eia)	4
FIGURE 4: Gas turbine components (Courtesy of GE)	39
FIGURE 5: Two-dimensional, conical, and annular straight-walled diffuser characterizations [2]	41
FIGURE 6: Diffuser energy conversion	43
FIGURE 7: Diffuser pressure loss function of divergence angle [17]	47
FIGURE 8: Typical diffuser performance curves: Rectangular diffuser, Cochran [13]	56
FIGURE 9: Solutions to two common design problems: Static pressure recovery coefficient $C_p$ [2]	58
FIGURE 10: Flow mechanisms of vortex control, Adkins et al. [1]	62
FIGURE 11: Physical insights: Main characteristics of diffuser high $Re$ flows [27]	81
FIGURE 12: Overview of OpenFOAM structure	92
FIGURE 13: Analyzed gas turbine typical exhaust diffuser geometry	93
FIGURE 14: Analyzed GT exhaust diffuser dimensions	94
FIGURE 15: SST $k - \omega$ best case mesh	109
FIGURE 16: SST $k - \omega$ annular diffuser closeup mesh	109
FIGURE 17: $k - \omega$ annular diffuser hub 17-cells boundary layer mesh	109

FIGURE 18: $k - \omega$ annular diffuser shroud 18-cells boundary layer mesh	110
FIGURE 19: Sampling stations along the exhaust diffuser length	113
FIGURE 20: Pressure contour prediction using RNG $k - \epsilon$ turbulence model	114
FIGURE 21: Flow development pressure profiles at different sampling stations	114
FIGURE 22: Flow field prediction from RNG $k - \epsilon$ turbulence model	117
FIGURE 23: Flow field obtained from the standard $k - \epsilon$ turbulence model	118
FIGURE 24: Flow development velocity profiles from the standard $k - \epsilon$ turbulence model	119
FIGURE 25: Flow field predicted by the SST $k - \Omega$ turbulence model	120
FIGURE 26: Higher resolution streamline predictions from the RNG $k - \epsilon$ turbulence model	120
FIGURE 27: $k - \omega$ predictions of streamlines	121
FIGURE 28: Low resolution $U_x$ velocity vector from the RNG $k - \epsilon$ turbulence model	121
FIGURE 29: High resolution $U_x$ velocity vector from the RNG $k - \epsilon$ turbulence model	122
FIGURE 30: Vorticity magnitude variation along the exhaust diffusion length as a function of turbulence models	124
FIGURE 31: Sampling stations in the shroud reversed flow region and separated boundary layer	124
FIGURE 32: Vorticity variations in the reversed flow region versus diffuser reduced length	124
FIGURE 33: TKE variations in the reversed flow region versus diffuser reduced length	125
FIGURE 34: TKE variations along diffuser length at different stations	126

FIGURE 35: Vorticity variations along diffuser length at different stations	126
FIGURE 36: Axial distribution of velocity varying cell count	129
FIGURE 37: Axial distribution of pressure recovery coefficient varying cell count	130
FIGURE 38: Combined normalized axial velocities at $x/h_1 = 1.01$ , 50 % annular diffuser varying turbulence models	134
FIGURE 39: Normalized $U_x$ at $x/h_1 = 1.01$ , 50 % annular diffuser	135
FIGURE 40: Normalized RNG $k - \epsilon$ $U_x$ at $x/h_1 = 1.01$ , 50% annular diffuser	135
FIGURE 41: Normalized SST $k - \omega$ $U_x$ at $x/h_1 = 1.01$ , 50% annular diffuser	136
FIGURE 42: Normalized $k - \epsilon$ turbulent kinetic energy at $x/h_1 = 1.01$ , 50% annular diffuser	138
FIGURE 43: Normalized turbulent kinetic energies at $x/h_1 = 1.01$ , 50% annular diffuser	139
FIGURE 44: Normalized turbulence intensities at $x/h_1 = 1.01$ , 50% annular diffuser	140
FIGURE 45: Axial velocities at $x/h_1 = 1.92$ , 10 % conical diffuser length	142
FIGURE 46: Normalized turbulent kinetic energy at $x/h_1 = 1.92$ , inlet conical diffuser	143
FIGURE 47: Normalized turbulent kinetic energy at $x/h_1 = 18.69$ , exit conical diffuser	144
FIGURE 48: Reduced pressure distributions at station 04 function of turbulence models	147
FIGURE 49: Axial distributions of pressure recovery coefficients varying turbulence models	147
FIGURE 50: Axial velocities at $x/h_1 = 1.01$ , 50 % annular diffuser varying inlet turbulence intensity	150

FIGURE 51: RNG k- $\epsilon$ normalized turbulent kinetic energy distributions at $x/h_1 = 1.01$ , 50 % annular diffuser varying inlet turbulence intensity	151
FIGURE 52: RNG k- $\epsilon$ normalized turbulence intensity distributions at $x/h_1 = 1.01$ , 50 % annular diffuser varying inlet turbulence intensity	152
FIGURE 53: Axial distribution of pressure recovery coefficients varying turbulence intensities	154
FIGURE 54: RNG k- $\epsilon$ normalized axial velocity distributions at $x/h_1 = 1.01$ , 50 % annular diffuser varying inlet temperature	155
FIGURE 55: RNG k- $\epsilon$ axial velocity distributions at $x/h_1 = 1.01$ , 50 % annular diffuser varying inlet temperature	156
FIGURE 56: RNG turbulent kinetic energy distributions at $x/h_1 = 1.01$ , 50 % annular diffuser varying inlet temperature	157
FIGURE 57: Axial distributions of pressure recovery coefficient varying inlet temperature	159
FIGURE 58: Axial variations of the TKE varying the turbulence models	160
FIGURE 59: Normalized axial velocity distributions at $x/h_1 = 1.01$ , 50% annular diffuser length by adding radial inlet velocity components	161
FIGURE 60: Normalized turbulence kinetic energy at $x/h_1 = 1.01$ , 50 % annular diffuser length adding radial inlet velocity components	162
FIGURE 61: Axial distribution of pressure recovery coefficients adding radial inlet velocity components	163
FIGURE 62: Axial distribution of pressure recovery coefficients considering one radial velocity component	164
FIGURE 63: Axial distribution of pressure recovery coefficients considering both radial velocity component	165
FIGURE 64: Axial distribution of pressure recovery coefficients varying inlet velocity angle	166

## LIST OF TABLES

TABLE 1: Summary of the Main Keywords in fvSchemes	85
TABLE 2: Overview of Solution Tools	87
TABLE 3: $k - \epsilon$ Baseline Boundary Conditions	102

## CHAPTER 1: INTRODUCTION

### 1.1 Research Problem

When the exhaust gas leaves the last stage of expansion of an industrial gas turbine, GT, it is still moving with a high velocity; its total energy is not negligible and can be wasted. Adding an exhaust diffuser after the last stage of the turbine recovers the static pressure by decelerating the fast-moving outflow. The reduction in velocity head is converted to a rise in static pressure [17], causing the pressure at the turbine exit to be lower than the atmospheric pressure and ultimately increasing the turbine output work and efficiency. An exhaust diffuser is an aerodynamically designed duct-shaped element, with a continually increasing area, located downstream of the last stage of the gas turbine expander. It is one of the GT components for which the shape can still be optimized to obtain a better design, and maximize the GT overall efficiency. However, the industrial GT exhaust diffuser performance depends on an optimum internal angle and the flow conditions at the inlet of this thermal device (Research hypothesis). The flow pattern at the inlet of an exhaust GT diffuser is highly turbulent, i.e. three-dimensional, unsteady, and heavily distorted. It is characterized by circumferentially non-uniform properties, the intensity and the distribution of vortical motions in axial and radial directions. Therefore the purpose of this research is to investigate this dependency, by considering the effects of some inlet conditions for the development of a more efficient gas turbine exhaust diffuser design. A free open-source CFD code,

OpenFOAM was used to perform a systematic analysis to predict the exhaust diffuser flow field development, parameters field data, and take advantage of this readily available computational and design tool. Other quantities, such as the efficiency of the exhaust diffuser conversion process that takes into account any losses manifested as a fall in diffuser total pressure, were also investigated. The structure and instructive approach of this dissertation have been designed to allow a comprehensive insight of the CFD topic by carefully selecting the most relevant aspects of a CFD analysis. Like any analysis, it should give us a good feeling for the behavior of the phenomena occurring in a typical annular-conical diffuser flow, such as the turbulent boundary-layer development and separation.

## 1.2 Research Motivation and Background

The ever-increasing world energy demand challenges political authorities and research engineers to come up with high standards, best ways to provide a reliable power supply, and increased efficiency to ultimately reduce the impact of greenhouse gases on the environment. With increasing world population, the use of electricity is becoming more ubiquitous around the world, and gas turbines (GT) are widely used in electrical power generation. The use of natural gas in the USA has been growing due to its competitive cost and fewer adverse human-health and environmental effects compared to coal, and to the nuclear energy which is in decline due to concerns over reactor safety, unresolved radioactive waste-disposal issue, and construction costs [24]. Our interest in the GT performance improvement was dictated by interacting developments in the 1990s that lead to gas turbine success, and the use of the combined

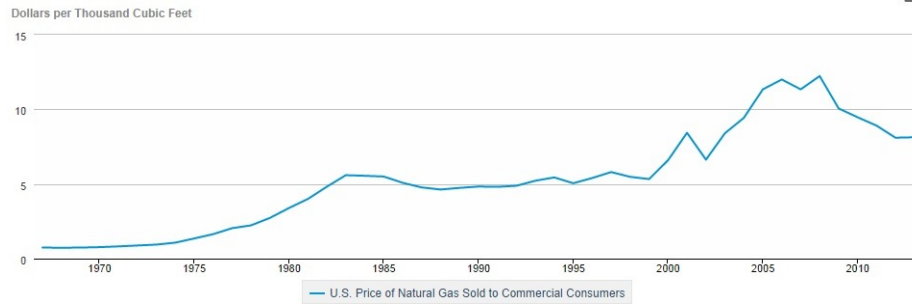


Figure 1: Natural gas price trend (US Energy Information Administration, eia)

cycles for power generation including the interactions of [34]:

- Advancements in research and development,
- The availability of fuel, i.e. natural gas,
- Growing environmental concerns, and
- Changing in the market conditions.

Natural gas availability and price stabilization in the mid-1980s, as shown in figure 1, played an important role in the renewed interest in GT by industries in the energy sector. Today, the same conditions are still applicable and the hydraulic drilling technique, fracking, is making natural gas even less expensive. Furthermore, the use of the natural gas in the US has been growing for year and is projected to grow for years to come compared to coal as shown in figures 2 and 3. Gas turbine power plants have two distinctive advantages over the coal-fueled power plants using steam turbines. Firstly, their thermal efficiency is much higher, a combined-cycle efficiency of more than 60% compared to about 35% for the coal-fired plants. Secondly, their carbon footprint or impact is much smaller. Currently researches are being conducted by universities and power industries around the world to push the combined cycle efficiency to about 65%. The GT exhaust diffuser is one of the components that can still im-

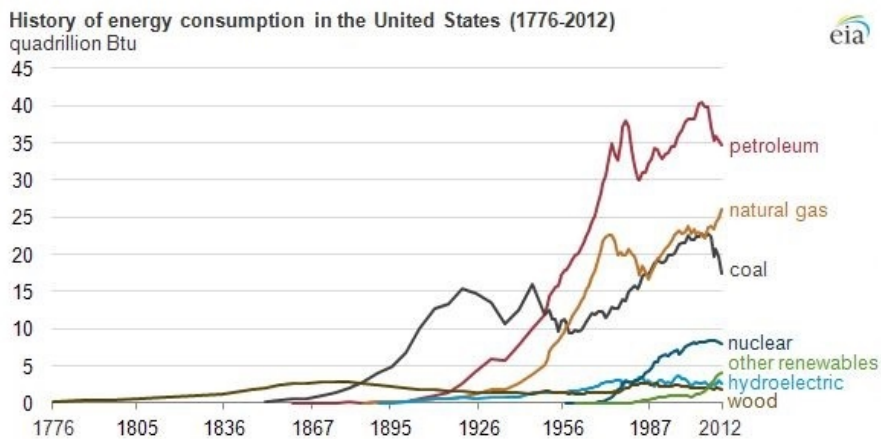
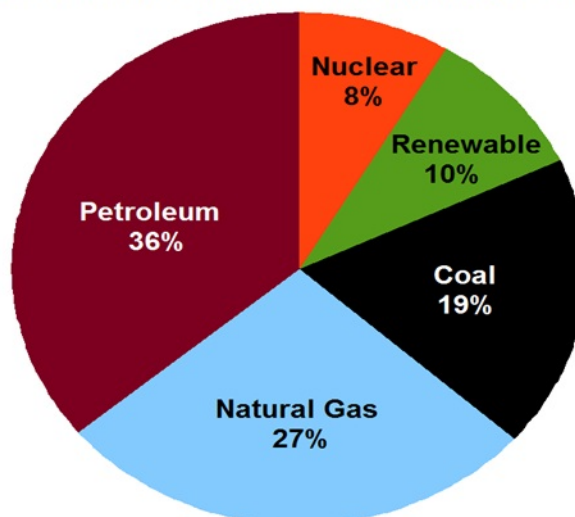


Figure 2: History of energy consumption in the US from 1776-2012 (US Energy Information Administration, eia)

United States Energy Consumption by Source



Data Source: US Energy Information Agency

Figure 3: Energy consumption by source in US (US Energy Information Administration, eia)

prove GT thermal efficiency as compared to components such as the compressor and the combustion chamber. It has been shown that a better GT exhaust diffuser design will increase its performance, i.e. higher pressure recovery, and subsequently increase GT power output and thus the GT overall efficiency. Lefebvre [17] asserts that an ideal diffuser will achieve the design velocity reduction in the shortest possible length, with minimum loss in total pressure, symmetrical and not too peaked inlet velocity profile, and with uniform and stable outflow conditions. However, in real engines the diffuser inlet velocity profile can vary with changes in engine operating conditions and secondary flows such as tip-clearance flows. Moreover, the total loss in pressure inside a diffuser consists of the sum of friction loss and stall loss, and pressure loss in long diffusers, with low divergence angle, is high due to skin friction along the walls. On many industrial engines and all aircraft engines, length is critical due to space occupation requirements. Therefore, designing a diffuser with a high divergence angle would reduce the diffuser length, as well as wall friction losses, and increase the diffuser performance. However, since stall losses stemming from boundary layer separation will increase with a shorter diffuser, it is essential to investigate ways of reducing this loss component. These considerations lead us to use the typical annular-conical difuser geometry configuration, with a high apex angle producing a strong separation of the inlined wall boundary layer, and tested by Sieker and Seume [27], in an experimental test rig at the Leibniz University Hannover, in Germany. More importantly, since annular diffuser lack available comprehensive data, compared to conventional conical diffusers [17], this experiment provided us with measurement data to validate our CFD approach in investigating the effects of some inflow characteristics on the dif-

fuser flow development. Besides, existing performance charts on annular diffusers are boundary-layer-type inlet flows, which are different from the turbine-generated flows in exhaust diffusers [17]. Since it is known that the GT exhaust diffuser performance depends on the diffuser inlet flow conditions, the experimental test rig, equipped with cylindrical spokes to generate the wake behind the wheel, simulated a more realistic GT exit flow environment allowing to numerically investigate inlet flow characteristics such as the turbulence intensity and the inlet flow velocity angle.

### 1.3 The Value of Numerical Methods in CFD Applications

The study of fluid dynamics evolved through three synergic predictions tools, i.e. pure experiment or physical insight relying on measurements, pure theory or mathematical analysis, and computational fluid dynamics, or CFD. The latter is the modern practical mechanism for solving flow problems that cannot be solved by known methods, and therefore do not have known analytical solutions. Currently, there is no completely general and accurate method for predicting GT exhaust diffuser performance [17]. Flows involving complicated three-dimensional effects, i.e. complex viscous flows such as that of industrial GT exhaust diffusers, are studied either experimentally or by computational fluid dynamics and not by traditional boundary-layer methods. CFD, provides a qualitative and quantitative predictions of fluid flow fields by means of numerical methods, i.e. the discretization of the governing equations of fluid flow and their solutions by iterative methods. Therefore, CFD is the art of replacing the system of the governing equations of fluid flow, representing the conservation laws for mass, momentum, and energy, by a set of algebraic equations

that can be solved on digital computers. It enables scientists and engineers to perform numerical experiments, i.e. computer simulations in a virtual flow laboratory, where it can simultaneously simulate, for example, higher Mach numbers and high flow-field temperatures encountered by transatmospheric vehicles. However, experimentation remains a strong component of fluid flow research since the fine details of high Reynolds number flows cannot be resolved at the present time, even by the largest supercomputer. CFD still needs to be improved to accurately and reliably compute all the details of a high Reynolds number turbulent flow in a record time. As a research tool, CFD can work with experiment to provide comparison as well as a means to interpret and understand basic phenomenological aspect of experimental conditions as well as the results of a theory [11].

#### 1.4 Goals and Objectives

The goals of this research were to:

- Conduct systematic CFD analyses of the exhaust diffuser turbulent flow considering selected inlet flow characteristics and flow field phenomena using OpenFOAM, a free open-source CFD code,
- Use the results to draw conclusions intended to improve the exhaust diffuser performance through an optimized diffuser shape that maximizes pressure recovery, and
- Establish best practice guidelines for CFD simulation of these flows; especially when using OpenFOAM.

Based on the above goals, the main objectives are summarized as follows:

- Complete literature review and define project scope,
- Complete OpenFOAM basic training,
- Select an experimental paper on an exhaust diffuser, and perform initial CFD analyses using the  $k - \epsilon$  turbulence model,
- Establish the fidelity of the CFD approach through results validation,
- Test the accuracy of additional selected turbulence models,
- Carry out additional simulations varying selected diffuser inflow parameters.

However, the objective of most engineering analyses, closed form or otherwise, is a quantitative description of the problem through its describing properties, in contrast to a closed-form analytical solution for which the solution is a continuous mathematical function. The computation results from the diffuser numerical analysis were found to be in reasonable agreement with measurements from a benchmark experiment carried out at the University of Hannover, Germany. One of the goals is to correctly predict the diffuser flow-field in the presence of an adverse pressure gradient, and the numerical results provided performance data and some guidelines used in the diffuser design process. The test rig is supposed to simulate or reproduce the conditions or characteristics of the diffuser flow. A comparison with CFD results should show the level of qualitative and quantitative agreement with the measurements. A treatment of the flow physics, i.e. physical properties, interactions, processes, and laws, highlights the basic concepts underpinning fluid mechanics, CFD topic, and turbulence predicting techniques. Besides turbulence models, other physical and chemical processes models may be invoked, such as radiative heat transfer and combustion models.

Various processes tending to increase or decrease flow variables and the conservation of the latter can be expressed as a balance of these processes.

### 1.5 Outcomes

The current investigations revealed that in increasing the inlet turbulence intensity and considering high flow-field temperature, both lead to the increase of the kinetic energy of turbulence,  $k$ , in the separated boundary layer, with an increase in the pressure recovery coefficient for a specific inlet turbulence intensity. For a given area ratio, it was found that there exists an optimum turbulence intensity for which the diffuser performance is maximum. In our case that optimum was found to be around 7.5%, and investigated value above it decreased the pressure recovery coefficient. A performance increase of about 37% has been observed at the annular diffuser exit and 7% at the conical diffuser exit. However, turbulence intensity value of 4% matched the experimental pressure recovery results. It was also found that the kinetic energy of turbulence in the separated boundary layer was drawn from the high vorticity generated at the diffuser kink. The peak of turbulent kinetic energy, TKE, along the diffuser length became maximum at the boundary layer velocity profile point of inflection, located inside the separated boundary layer, when the peak of the vorticity reached its minimum at the same point of inflection. Therefore, generating higher vorticity close to the casing wall will increase the TKE in the separated boundary layer that will suppress flow separation and reversal and improve diffuser performance. One practical way of implementing this would be to induce a shear layer at this location, for example by injecting air of a different speed, that will generate high

vorticity. Also, the backward-facing step generated high shear in the neighboring region. To avoid related adverse effects, the hub geometry profile at this location should decrease more smoothly so that combined with the effects of induced wall turbulence, uniform flow conditions may be obtained at the exit of the annular portion of the diffuser. The investigations of the inlet velocity angle showed that an angle of about  $2^\circ$  matched the performance obtained experimentally. The following list is a summary of expected outcomes that would be obtained in implementing the results of the current investigations:

- Increased exhaust diffuser performance through increased pressure recovery,
- Appropriate diffuser internal geometry by the design of more optimized, short diffusers with minimum pressure loss,
- Better understanding of the influence, on the diffuser flow, of inlet conditions like turbulence intensity, flow angularity, and temperature.
- Additional scientific knowledge in this field leading to gas turbine technology improvement, and improved ways of increasing efficiency by reducing fuel consumption
- Increasing technical capability to produce more mechanical power with a target of 64% combined-cycle gas turbine overall efficiency,
- Reduced environmental impact,
- Complement other technical improvements such as material advancements and cooling innovations allowing increased temperatures and efficiency of the gas turbine,

- Strengthen energy research and development role in furthering above advantages

## 1.6 Thesis Outline

This PhD thesis is divided into six chapters. The first chapter introduces the problem area by spelling out the reason for which an exhaust diffuser is needed at the gas turbine exit, making explicit the research hypothesis, and why the CFD analysis is most suited to predict the flow behavior through this thermal device. It goes on by motivating and emphasizing the importance of research in this area with respect to the increasing world demand in the energy use and increased efficiency of gas turbines and other technical devices. After defining the research goals and objectives, the introduction chapter also details the contributions of the present work and finish with an outline of the thesis. Chapter 2 extensively expands on the review of the available literature on the subject, giving an overview of the level of knowledge and development achieved at present as a result of using modern methods. The chapter concludes with the identification of an area of research not much investigated, i.e. the effects of turbulence characteristics and temperature on the flow development inside a gas turbine exhaust diffuser. In chapter 3, the continuum concepts and summary of the treatment of the physics of fluid flows, including the conservation laws of fluid motion, elementary physical processes, the boundary conditions are introduced. The gas turbine and its components are described here, with an emphasis on the diffuser, its performance characteristics, existing diffuser types are also introduced. A section about the engineering design process examines different aspects of a diffuser design. Chapter 3 also gives a treatment of turbulence and its modeling, summarizing the different different turbulence models tested in our investigations and finishes with the

relevant numerical solution methods.

Chapter 4 talks about the research methodology by giving basic procedures used to gain additional insights in the diffuser flow predictions using the CFD analysis tool. It describes the basic steps required to perform the analysis using the free CFD software package OpenFOAM, and the different methods of solving the problem at hand. Chapter 5 delves into the extensive simulation result data for the analysis of the effects of selected diffuser inlet flow characteristics. The veracity of various turbulence models, the effects of turbulence characteristics, temperature, flow angularity of the flow development, velocity profiles, and the diffuser pressure recovery coefficient are examined. Chapter 6 wraps up the research thesis by drawing overall conclusions and discussing the limitations and potential for future works that can answer other important questions in the same line of research inquiry.

## CHAPTER 2: LITERATURE REVIEW

The design of high-performance GT exhaust diffuser has been an area of extensive research due to the ever-increasing demand of high-performance GT, the growing market in power-generation, and industrial and marine applications [38]. Moreover, the GT exhaust diffuser is a critical component in combined-cycle power plants connecting the Brayton cycle used in gas turbines to the Rankine cycle used in steam turbines. Combined-cycle applications, in which the GT exhaust is used to generate steam that is subsequently expanded in the steam turbine are known to have higher cycle efficiencies; the GT exhaust diffuser is considered as the only component that can still further significantly enhance the efficiency of the combined cycle power plants since it is hard to obtain more efficiency improvements from the other major gas turbine components, i.e. compressor, combustor, and the expansion turbine. In general, the ultimate goals of some experimental and numerical analyses performed were twofold: identify the potential of diffuser improvements and verify engineering models. The purpose of any engineering analysis is to predict a system's behavior through its describing properties, including the flow structure, configuration, and important features. Experimental investigations for the purpose of designing diffusers were based mainly on performance charts or maps. Vassiliev et al. in their work on CFD analysis of industrial gas turbine exhaust diffusers concluded that today's CFD methods are capable of capturing the basic flow structures in GT exhaust dif-

fusers even though the quantitative agreement with measurements are considered only satisfactory due to inaccuracies of turbulence models and uncertainties in boundary conditions. These issues along with shortcomings related to complex geometries, i.e. the required time and manual work for mesh preparation, the limitations of computer capacity leading to compromises between required mesh sizes and resulting accuracy, are considered as key aspects needed for the reliable CFD modeling and design of high-performance exhaust diffusers [37]. However, for numerical predictions of a gas turbine exhaust diffuser performance with a reasonable accuracy, it is momentous not only to cover all essential features of the actual flowfield but also to consider essential parameters of the channel geometry including the definition of appropriate boundary conditions.

Numerous experimental, theoretical, and numerical investigations have been conducted on GT turbine exhaust diffusers with different configurations. The following is a collection of the main topics addressed in the existing literature:

- The use of different turbulence models to identify proper and practically adequate ones. Different wall functions are also considered for RANS turbulence models [37], [6], [39].
- The influence of diffuser inlet conditions on diffuser performance by varying geometry and flow parameters, and the boundary layer thickness at the diffuser inlet [31].
- The effect of rotor tip-clearance flow, wakes, and other secondary flows constituting the turbine exit flow environment causing perturbations or unstable

conditions, including the non-uniformity of the diffuser circumferential inlet flow; The turbine exit flow simulated using rotational wheel with cylindrical spokes or blades [14], [7], [26].

- The impact of inlet swirl on exhaust diffuser performance and its interaction with struts and the effect of the presence of struts on the diffusers performance. CFD is now critical in this aspect in order to gain more insight [26].
- The types of diffuser geometry configurations and important factors influencing their performance among which we have the area ratio and the length of the flow path along which diffusion occurs; no correlations exist for example for hybrid diffuser such as the one we are investigating made up of annular and conical parts.
- The minimization of exhaust diffuser losses. Numerical investigations providing insight into loss location and reduction mechanism [39], [35].
- The impact of 3-D effects on diffuser characteristic and the use of steady or unsteady state approaches
- Performance improvements through modified and improved aerodynamic profiles, i.e. airfoil shape design for an optimal passage channel resulting in lower loss coefficients, for an upgraded turbine, reduced radial clearances, etc. The use of aft-loaded profile technology significantly improved the overall performance [39], [26].
- Industrial Gas Turbine component optimization studies due to upgrades of other components and recourse to turbine re-design since the diffuser effectiveness

strongly hinges upon the turbine outflow parameters. Preliminary analyses of original turbine provide reference points and allow the identification of upgrade potential. A proper turbine outflow characteristics will favor pressure recovery and ultimately influences the overall turbine efficiency [39].

From this list, it can be observed that both aerodynamic and thermodynamic management of GT exhaust diffusers are considered in these investigations. David et al. [14] affirm that experiments have shown a positive effect of moderate inlet swirl on the performance of diffusers operating close to stall when swirl and tip-clearance are investigated. The tip-clearance flow can be simulated by a near-wall-jet injection that can reduce the separation zone at the diffuser outlet.

Although systematic investigations on diffuser flows took place in the first half of the twentieth century through Andres [1909], Gibson [1925], Nikuradse [1929], and Peters [1931], with the latter two showing the influence of inlet boundary layer thickness on diffuser performance [7], significant contributions were obtained during the first period of the second half of the twentieth century. Many researchers have investigated diffusers, including Kline and co-workers [1959] who mainly worked on conical and two-dimensional diffusers and established four flow regimes, viz., no appreciable stall, large transitory stall, fully developed stall, and jet-flow. The transitory stall is characterized by short-duration flow reversal propagating up and down of the diffuser walls. They also introduced performance maps based on non-dimensional geometrical parameters.

A. H. Gibson [1925] first established optimum divergence angle for given area ratio showing that certain geometries are inclined to greater losses than similar sudden

expansion ones. In order to determine appropriate configurations, Sovran and Klomp experimentally tested more than 100 annular rectilinear configurations from 15 diffuser geometry families and identified optimal combinations of aspect ratio of outlet and inlet areas and diffuser length. They also introduced a widely used chart displaying pressure recovery data of 2-D conical and annular diffusers. An important principle has been derived from these studies and subsequently used in other theoretical analyses is that the geometry of an ideal diffuser will maintain the flow at the edge of separation with the wall friction being zero along the diffuser wall [35]. The experimental data from these investigations are often used to evaluate numerical procedures and the predictions. These investigations also provided guidelines used today in the industry. For example, a value of  $4^\circ$  for the inclination of the diffuser wall with respect to horizontal direction.

Stevens and Williams [1980] experimentally investigated 2 configurations using a wide range of inflow boundary conditions. They conducted a number of experimental works trying to simulate or reproduce more realistic flow conditions at the exhaust diffuser inlet. To simulate the turbine last stage wake characterized by swirl and high level of turbulence, they built a scaled down model of the combined gas turbine - Exhaust diffuser including essential elements of a typical combination such as a ring of guide vanes or a wheel with cylindrical spokes or blades modeling the last turbine rotor generating the turbine unsteady exit wake flow environment that features swirls. The presence of struts in the exhaust diffuser plays different functions, i.e. support load, straighten the flow, provide passages for cooling, and lubrication. The diffuser flowfield configuration is affected by flow separation and unsteadiness. The most com-

prehensive depiction of the GT exit flow is the main flow featuring swirl combined with the tip flow, which in turn has its own swirl. These scaled down models were run with a Reynolds number above 100,000, high enough to ensure similar flow conditions with real diffusers which operate with a Reynolds number above 1,000,000, making negligible the effect of viscosity. Some of the test rigs used different size of grids to provide specific turbulence conditions and ensure rotational symmetry of the flow [7]. Measurement programs and required instrumentation were put in place to ensure sufficiently accurate flow measurements. Ubertini and Desideri showed in their experimental measurements of flow angles that they are below  $10^\circ$  producing a misalignment error of less than 1% in the measurements, small enough to conclude that the radial component of velocity can be neglected. These accurate test results could be used to validate numerical procedures.

Vassiliev, Irmisch, and Florjancic [37] made important contributions focusing on key aspects for the reliable CFD modeling of exhaust diffusers and presented an automated procedure for a time- and resource-efficient and accurate prediction of complex diffuser configuration based on unstructured hybrid meshes. Eighteen configurations out of 5 of the 15 families tested by Sovran and Klomp were used in their numerical analysis. They simulated a number of 2-D diffuser configurations using six different turbulence models based on the eddy-viscosity hypothesis, including one-equation models, standard and realizable k-epsilon models with wall functions or near-wall resolution of boundary layers. They also discussed the adequate boundary conditions definitions, and investigated the role of secondary flow on axial diffusers. They concluded that the realizable k-epsilon model with two-zone near wall treatment was

the most suitable model for diffuser flow simulations and the one with wall functions had results similar to standard  $k$ - $\epsilon$  which significantly overpredict pressure recovery. Comparing the calculated diffuser pressure loss coefficients of coupled and uncoupled turbine-diffuser, they found that all flow field features such as the turbulent kinetic energy and secondary flow have to be captured when estimating realistic inlet boundary conditions for CFD simulation of isolated diffuser flow field.

V. Vassiliev et al.[36], investigated experimentally and numerically the impact of swirl and Mach number on the performance of gas turbine exhaust diffuser. They used a scaled test rig to simulate and vary inlet parameters to obtain conditions similar to those existing in real engine using strutted annular diffusers. They subsequently proposed a fully automated procedure to perform a 3-D diffuser flow analysis by defining some recommended inflow turbulence variables correlations suitable for moderate turbulence levels of about 4%; this value is close the 3% we used in our initial analysis with a constant inlet total temperature. Their CFD results, using the  $k-\epsilon$  turbulence model with 4% turbulence intensity, show mostly good quantitative and qualitative agreement with measurements. The biggest discrepancy occurred with the strongest flow separation, and CFD overpredicted the separation zone. The prediction error in the pressure recovery coefficient is, however, less than 4%.

Feldcamp et al. [6] conducted cold flow experiments to investigate swirling flows in an annular diffuser with various strut configurations at 0, 20, and 40° of inlet swirl. They evaluated the diffuser and strut performance based on pressure recovery and detailed pressure distribution. CFD simulations with approximately 4 million control volumes were performed using several turbulence models and near wall treatments to

predict the performance of the same annular diffuser for both low and high Reynolds numbers. Their work was motivated by the need to correctly predict both the magnitude and trends in diffuser performance varying swirl conditions. The computational objective was to evaluate the ability of modest RANS based CFD models to reasonably predict the pressure recovery and major flow structures such as separation, vortices, and exit flow distortion without exactly resolving the details for the purpose of designing these types of devices. The authors investigated a range of inlet turbulence intensity (TI) and compared the predicted diffuser exit velocity profiles to experimentally measured ones. They found that for zero swirl the flow was best predicted with a TI of 2%; however, for 20 and 40 degrees of inlet swirl better predictions were obtained using a TI of 4% and concluded that using increased inlet turbulence intensity dampens the formation of horseshoe vortices leading to poor prediction of outlet flow distortions. This flow parameter is thus important to obtain an accurate flow prediction.

Vassiliev et al [39]. investigated the aerodynamic optimization of the GT26 exhaust diffuser following a major upgrade of the compressor which resulted in higher mass flow, power output, and efficiency. The performance of the original diffuser has been first assessed, in terms of exhaust loss, using measurements in a test engine before the compressor upgrade. The measurements using two 5-hole probes provided representative information about turbine outflow conditions or diffuser inflow conditions; the measured radial distributions of flow angle, total pressure, and total temperature were then considered as inflow boundary conditions for the numerical analysis. The increase in the mass flow rate significantly impacted the Mach number and the

residual swirl, with the latter increasing the original exhaust diffuser loss. Since the loss depends on the diffuser geometry and the inflow conditions, such as, the Mach number, the total pressure and temperature profiles, turbulence level, and residual swirl, these in turn depend upon the design of the expansion turbine, specifically that of the last turbine stage. However as stated earlier, the diffuser geometry can also be optimized based on existing inflow conditions by matching, for example, the diffuser strut to residual swirl. CFD analysis using an automated procedure allowed to perform calculations and helped to identify where the exhaust loss can be significantly reduced by diffuser optimization. The shape of the annular part was refined using CFD analysis which considered the impact of the struts. The turbulence at the inlet, which is the only input not available from measurements, was adjusted to calibrate the numerical model in order to achieve the best match with measured losses. This resulted in a choice of a turbulence intensity, TI, of 4.5% and a turbulence length scale of  $0.07D_h$ , where  $D_h$  is the hydraulic diameter and both parameters uniform across the inlet cross section. The realizable  $k - \epsilon$  turbulence model was used to calculate the flow inside the diffuser. The total loss comprises the strut loss, end wall loss, Carnot diffuser loss, and the residual dynamic head loss. The strut losses due to local flow separation were the most important ones leading to its redesign. The implementation of the improvements confirmed the expected results with a loss reduction of more than 30% with only low cost modification. Both the gas turbine and the diffuser tests performance showed an overall improvement confirming the positive effect of the diffuser redesign on the engine behavior.

In a recent paper, Vassiliev et al. [35] investigated the impact of inflow parameters, including Mach number level, total pressure distribution, flow angle, and turbulence, on the performance of a heavy-duty GT exhaust diffuser using CFD, experimental data from a test rig, and field measurements. They also discussed the minimization of the losses existing in this thermal component and showed that nonuniform pressure distribution and a moderate residual swirl can enhance diffuser performance. They investigated and implemented two approaches for exhaust losses reduction in retrofit engines, i.e.,

- Redesign the exhaust diffuser without modifying the expansion turbine to adapt it to inflow conditions
- Redesign at least the rotating blade row of the turbine last stage and keep the actual diffuser to fit the inflow conditions to the existing diffuser geometry.

The decision to opt for one or the other hinges on technical and economical considerations since for an existing GT, combining both options for a redesign is often economically not feasible; a proper choice can provide significant improvements as confirmed by field engine measurements of the implemented modifications. For the first option, modifications were aimed at the first strut that caused significant losses due to flow separation. As for the second option, their analysis showed that a change in inlet pressure distribution with local peak at the walls significantly reduced diffuser losses justifying the redesign of the turbine last row of rotating blades. However, for a completely new GT design both options can be considered for an optimal performance.

The effect of wakes and secondary flow on re-attachment of turbine exit annular diffuser flow was studied by David et al. [14] who simulated the turbine exit flow environment by means of rotating wheel equipped with cylindrical spokes and an annular diffuser with an apex angle of  $20^\circ$ , purposely chosen to create a strongly separated flow based on Sovran and Klomp performance maps. The goal of their studies was to understand the impact of secondary flows on the separated diffuser performance. They considered the same configuration tested in an experimental test rig at the Leibniz University, Hannover. They evaluated three turbulence models, i.e. the standard k-epsilon, the Shear Stress Transport (SST), and the Scale Adaptive Simulation with SST (SAS-SST). The measurements showed that for low rotational speeds of the spoke-wheel, the flow in the diffuser separates as free jet as predicted by theory; however, for rotational speeds greater than 500 rpm, the flow remains attached to the outer diffuser wall. They concluded that only the elaborate SAS-SST turbulence model was capable of predicting the stabilizing effect of the larger rotational speeds of the spoke wheel to the diffuser flow. They also concluded that the mixing effects of wakes and secondary flow pattern are responsible for the reattachment and that higher numerical costs of unsteady calculations must be accepted to increase the understanding of the physical flow phenomena in turbine exit flow and its interaction with the downstream diffuser. Observing all previous experimental investigations found in the open literature, they concluded that for more accurate and compact design, the entire system of last turbine stage, diffuser, and duct have to be taken into account during the design process. Furthermore, they found that the orientation of the absolute swirl with respect to the rotation of the turbine has a dominant effect

on diffuser performance and that the optimum static pressure recovery, for constant area ratio diffusers, could be moved toward shorter normalized diffuser sizes than given by Sovran and Klomp performance charts. In their 2004 work, using a steady-state analysis with the frozen-rotor approach, David and his coworkers showed that circumferentially non-uniform flow at the diffuser entrance had a strong effect on the diffuser performance. They claimed that this could not be obtained using the classical mixing plane approach.

In the current study we shall account for the influence of unsteady wakes on turbulence by investigating the impact of turbulence level on the predicted results and determine appropriate turbulent quantities for the inlet to ensure good predictions of the measurements. Also, since temperature variation at the turbine exit will create a distortion of the mass-flux distribution (density times velocity) and influence the flow and the loss, we shall look at the impact of the temperature itself on these.

Working for Alstom Power Company, the authors in [35] with extensive practical and computational experiences considered the fact that the flow in the exhaust diffuser strongly depends on the inflow conditions to analyze the impact of some parameters such as Mach number level, total pressure distribution, flow angle, and turbulence using CFD, experimental data from a test rig, and field measurements. They also discussed the minimization of exhaust losses in heavy-duty gas turbines. They showed that a nonuniform pressure distribution can lead to a better diffuser performance as well as a moderate residual swirl; this is contradictory to a widespread opinion that the optimal condition for a diffuser is an axial uniform inflow. Also contrary to the results of investigations on conical and annular diffusers showing that residual swirl reduces

the pressure recovery, especially for high values of swirl angles above  $20^\circ$ , the impact of swirl in practical applications of exhaust diffusers of heavy-duty turbines is quite different from simplified mode conditions. The higher pressure recovery in a diffuser without strut can be reached than in a diffuser with struts since struts will always generate additional losses even in the case of optimal inflow conditions. However, they showed that any negative impact of residual swirl on the exhaust diffuser performance can at least be neutralized by a proper matching of the strut geometry. They claimed that residual swirl is typically favorable for turbine last stage performance since allowing extraction of more work and increased efficiency. The total pressure profile near the casing walls should have a twin-peak shape, i.e., higher than in the middle of the channel. It is important to note that diffuser inflow conditions depend upon specific technical or industrial applications and the location of the diffuser. Since the diffuser flow behavior and performance depend upon adjacent components and that the former should not be optimized as a stand-alone component but as a part of a system, the authors focussed their attention on the interaction of the exhaust diffuser and the turbine. From their analysis of possible consequences of unsteady conditions on strutted diffusers, the authors found that the average loss values were very similar in both steady and unsteady simulations notwithstanding the fact that the turbine upstream the exhaust diffuser generates unsteady wakes which have an influence on turbulence. They concluded that, in practical applications, the steady-state approach can still be used with a relatively high degree of confidence. Since the investigations of unsteady effects are very recent, they assert that further investigations are advisable and may provide new opportunities for diffuser improvement.

Considering that a wide variety of inlet conditions are present in many applications of diffusers, Stevens [31] carried out tests to investigate the influence of inlet conditions on the performance of two symmetrical annular diffusers with 4:1 area ratio and, 2.5 and 5 degrees wall angles. With the latter, a detailed measurements of the boundary layer growth on inner and outer walls were made and turbulence measurements were taken at inlet. The inlet conditions were varied by using both inlet sections of varying lengths and annular gauzes. The gauzes were inserted about 15 diameters upstream of the inlet to produce a boundary layer momentum thickness thicker than the one in fully developed pipe flow. He found that the diffuser efficiency deteriorated with increase in outer wall momentum thickness when testing the 2.5° diffuser. The results were compared to a theoretical analysis based on the assumption of power law velocity profiles in the conical and annular diffusers. The comparison shows good agreement for the separation point and the axial static pressure distributions. The author invoked the work of Ainley, "Investigation of air flow through some annular diffusers", in which it was found that the performance of symmetrical annular diffuser deteriorates more rapidly with increasing outer wall angle with the diffusion continuing for some distance in the settling chamber due to radial momentum transfer that reduces the velocity profile momentum coefficient, and that the flow at outlet was unstable in diffusers with wall angles greater than 5°. The author also showed that the momentum thickness on the outer wall was a major parameter controlling annular diffuser performance.

Pradeep et al. [26] investigated diffuser flow characteristics under two inflow swirl conditions to simulate typical turbine exhaust flows under full load and part load

operations, i.e., low swirl and high swirl respectively. In their attempt to improve the GT exhaust diffuser performance by shape modifications, they attenuated the flow separation due to diffuser high initial angle by using, for the diffuser casing, a 4th order polynomial curve with a point of inflexion right at the struts leading edge and with both end angles equal to zero; this change improved the diffuser performance. Comparing two cases, one with low swirl and the other with high swirl, they came to the same conclusion as Vassiliev et al. that performance improvement obtained with the lower swirl case was better than that with higher swirl.

Fleige et al. [7] indicated that the increase of diffuser performance, mainly in short diffusers, due to the introduction of moderate swirl was previously observed by other researchers, who indicated that larger tip gaps can increase diffuser performance. It was also found that higher degrees of swirl would decrease the pressure recovery as the flow separates at the hub of annular diffusers or the presence of backflow in the core of conical diffusers. An approximately 1/10 scale model of a typical GT exhaust diffuser, i.e., annular part followed by conical one, was investigated experimentally and numerically by Fleige et al.[7], simulating the turbine exhaust flow by swirl of four different angles respectively coupled with tip leakage flow prevalent in the outer wall region. Using cold air flow measurements, they concluded that even without struts, inlet swirl angle higher than  $8^\circ$  was found to adversely influence the pressure recovery. Also profiled struts, preferably with "streamlined" profiles, were not able to redirect the flow, and for swirl angles higher than approximately  $10^\circ$ , cylindrical struts yielded better diffuser performance than profiled struts.

The studies mentioned that McDonald and Fox [1966] indicated that the influence of the inlet Reynolds number on pressure recovery is weak as long as the inlet flow shows fully developed turbulent boundary layers [7]. The investigations found that Chen's and the standard  $k$ -epsilon models overpredict the pressure recovery of the annular part of the GT exhaust diffuser at all inlet conditions; however, the results of the numerical analysis are less extensive.

Sonoda et al. [28] carried out experimental and numerical investigations to gain a better understanding of the flow characteristics within an annular S-shaped duct connecting the low- and high-pressure compressors of aircraft gas turbine engines. The annular S-shaped duct consisted of six struts with NACA 0021 profile geometry canted by  $15^\circ$  to match the S-shaped duct passage. They also studied the duct exit shape influence on the upstream flow using two types of downstream passage, a straight annular passage and a curved one. They showed that the total pressure loss near the hub was larger than near the casing due to the instability of the flow which greatly increased in case of curved annular passage. A horseshoe vortex was observed experimentally near the casing, in the high loss region; the spatial position of which depends on the passage core pressure gradient. For their numerical analyses, they used an in-house-developed three-dimensional compressible Navier-Stokes code with a low-Reynolds-number  $k - \epsilon$  turbulence model applied to the flow. The numerical results were in good agreement with experimental ones, predicting a region of very high pressure loss near the hub at the duct exit due to the formation of horseshoe vortex related to the increase of inlet boundary layer thickness; however, quantitative discrepancies were observed in the wake region. They concluded that these regions of

high pressure loss may act on the downstream compressor as a large distortion and strongly affect its performance. Downstream back pressure was adjusted to coincide with the corrected mass flow.

Sultanian et al. [32] experimentally and numerically investigated the complex internal flow field in an industrial gas turbine exhaust system, GE-MS9001E type, featuring an annular diffuser passage with struts, followed by turning vanes and a rectangular plenum with side exhaust. A scale model was used for better understanding of the flow field and validation of CFD prediction capabilities for improved design applications. Numerical analyses were performed using a 3-D N-S code using the standard k-epsilon turbulence model for three load conditions, i.e., full speed no load characterized by a very high negative swirl angle ( $- 50.8^\circ$ ), full speed mid (57%) load ( $- 4.9^\circ$ ), and full speed full load with positive low swirl angle ( $+ 13.6^\circ$ ), considered positive in clockwise direction. It is important to note that an important characteristic of an industrial GT exhaust diffuser system is that the inlet mass flow rate and the flow angle widely vary with turbine load. They found that the total pressure loss and static pressure drop or recovery vary with the change in load condition. Significant decrease of these properties was observed near the mid load operating condition, with better agreement between calculation and experiment in the front part for all load conditions. They also observed that calculation always underpredict total pressure losses and static pressure drops compared to experiments in the model exit, i.e. pressure levels are calculated somewhat higher indicating that secondary flow losses in regions of turning vanes and the plenum are not fully captured by the turbulence model, which is an important tendency to design application.

They ultimately concluded that the applied CFD method was capable of predicting complicated gas turbine exhaust system flows and offered a useful design engineering tool for design applications using the standard high-Reynolds-number  $k - \epsilon$  model. The used wall function ensured that first nodes from the wall region fall within the logarithmic region for proper applicability of the wall function boundary conditions with the computed  $y^+$  were in the range of 30 - 160 for most surfaces.

Olaf Sieker and his co-worker Joerg Seume [27] used a scale model of a typical gas turbine exhaust diffuser for experimental investigations looking at the influence of rotating wakes. Measurements with variable-speed rotating cylindrical spoke wheel using 2 mm- or 10 mm-spokes to simulate turbine rotor wakes were obtained, as well as measurements without spoke wheel. They investigated the separating behavior, i.e. the annular diffuser flow pattern and its pressure recovery, under the influence of swirl and high energized wakes. With higher rotational speed of the wheel, higher induced swirl in the diffuser, as well as higher turbulent energy of the rotating wakes are expected. They discovered that without a spoke-wheel, the annular diffuser separates at the shroud for all swirl configurations. The 2 mm spoke-wheel showed an unstable separating diffuser. For a non-rotating 10 mm spoke wheel, and for the case of rotational speeds less than 1,000 rpm, the annular diffuser separated at the shroud. By increasing the rotational speed there was no separation, and a much higher pressure recovery was achieved than without a spoke wheel. A mass flow rate of about 6 kg/s was kept constant, for all measurements, by increasing the frequency of the axial fan due to the fact that increasing rotational speed of the spoke wheel leads to increased pressure loss. Swirl angles of 0, 15, 25, and 30° were respectively used.

For the investigations without a spoke wheel, non-axisymmetric peripheral static pressure distributions were measured. The experiments without a spoke-wheel are used to validate our numerical procedure and conduct further numerical investigations that form the gist of our research. They also showed that bladed wheel has a weak impact on the diffuser performance than a wheel with cylindrical spokes and produces unrealistic high unsteady distortions that significantly influence the diffuser pressure recovery.

Kline et al.[13] carried out the first systematic study of flow patterns in straight-walled diffusers and defined the four common and important optimum problems in diffuser design in relation to flow regimes in terms of geometrical parameters. They discussed two basic problems encountered in the design of straight-walled diffusers, i.e. the prediction of the overall flow regime, and the design of the optimum straight-walled diffusers. At that time, only existing data, i.e. maps of expected flow regime for two-dimensional flat diffusers and performance data on recovery and effectiveness, for both conical and two-dimensional flat diffusers, they thus related the flow regime to performance curves from various geometries and associated the parameters on the flat units with those of conical units, i.e association of geometrical parameters, in order to make a best use of them and to generalize results. The association or correspondance of variables was based on the idea that the area ratio be made the same at least up to the first order in terms of these variables in the different area ratio expressions while preserving the expansion ratio. The flow-regime charts in association with the developed methods for correlating the flow regimes of various geometries are believed to be able to well predict the location of optimum conditions

and the general type of flow to be expected or both with the assumptions of reasonable inlet conditions, straight walls, and low Mach numbers. Each flow regime was conveniently characterized by a specific flow pattern representing an essentially continuous spectrum with low pressure gradients and shorter diffusers giving less stall and smoother flow. They found that if the diffuser-divergence angle was continuously increased from zero degree while the inlet flow conditions, the wall length, and the throat width were kept constant, four regimes exist. They demonstrated that as the diffuser angle is increased, the rate of increase of the pressure recovery coefficient is reduced by the additional losses and the production of a less uniform exit-velocity profile. They emphasized the fact that correlation of flow regime does not imply correlation of recovery value since more variables enter into account when determining recovery than into determining flow regime; and that Reynolds number, aspect ratio, and inlet boundary layer within limits do not appreciably affect flow regime, but do affect recovery and losses. They believed, without verifications that at very high angles, the important parameters affecting recovery are  $L/W_1$ , with  $L$ , the inclined wall length of a two-dimensional straight-walled difuser and  $W_1$  its inlet height, the inlet conditions, including boundary-layer thickness and turbulence, and downstream geometry. They concluded that for good recovery, high  $L/W_1$ , high inlet turbulence, and thin inlet boundary layers are desirable, and that a partially blocked exit or tailpipe is also preferable, or a plenum discharge. They concluded that the presented correlations could fairly and reliably produce the location of optimum performance and/or of flow regime to be anticipated even though the value of losses and recovery at these conditions could not yet be predicted in general; however they appeared to

give correct predictions for straight-walled passages than any known method based on boundary-layer theory alone.

The review of the numerous research existing on the turbulent flow within an exhaust diffuser revealed that the data on the effects of varying the turbine exit flow turbulence intensity, the temperature, as well as the flow angularity at the inlet of the exhaust diffuser were scant. Extensive experimental studies using axial cold air turbine show favorable effect of swirl on diffuser performance; however. Very few investigators such as Zierer [1995] who experimentally investigated the flow in diffuser located behind an axial flow compressor and found that a higher inflow turbulence level and periodic unsteadiness tend to increase the diffuser performance and stabilize diffuser outlet flows. Early experimental work performed by Stevens and Williams also looked at the influence of inlet conditions, especially the impact of turbulence, on the performance of annular diffusers.

The purpose of the current work is to further gain a better understanding of the influence of these two parameters on a typical GT annular-conical combination exhaust diffusers. The defined research project goals were then to conduct systematic CFD analyses of the exhaust diffuser turbulent flow considering these actual physics at the inlet of the diffuser using an open-source CFD code to minimize the cost and establish best practices guidelines for the efficient use of this simulation software in simulating typical flows. The results of the investigations should allow the design of optimized diffusers that maximize pressure recovery.

## CHAPTER 3: THEORETICAL FRAMEWORK

### 3.1 Governing Equations of Fluid Flow

#### 3.1.1 Introduction

In this section we will derive and examine the nature of the transport equations governing a general, i.e. compressible and viscous, fluid-flow problem, the Navier-Stokes equations. These equations are based on Newton's second law formulated as:

$$\vec{F} = m\vec{a}, \quad (1)$$

expressing the equilibrium of forces for a moving fluid element of mass  $m$ . Since, for a fluid particle system, it is rather convenient to work with density than mass, let us divide the above equation by the system volume. The applied force per unit volume is composed of two types, i.e. surface forces and body forces. Rewriting equation (1) in a more traditional form we get:

$$\rho \frac{D\vec{V}}{Dt} = \vec{f} = \vec{f}_{body} + \vec{f}_{surface}. \quad (2)$$

Neglecting the effects of other body forces, the gravitational force per unit volume is given by:

$$\vec{f}_{body} = \rho\vec{g}, \quad (3)$$

where  $\vec{g}$  is the acceleration of gravity vector. The total surface force, pressure and

viscous forces, depends on the stress tensor,  $\tau_{ij}$ , and is given by:

$$\vec{f}_{surface} = \vec{\nabla} \cdot \tau_{ij} = \frac{\partial \tau_{ij}}{\partial x_j}. \quad (4)$$

The Newton's second law thus becomes:

$$\rho \frac{D\vec{V}}{Dt} = \rho \vec{g} + \vec{\nabla} \cdot \tau_{ij}. \quad (5)$$

Let us next express the stress tensor,  $\tau_{ij}$ , in terms of the velocity vector  $\vec{V}$ , relating it to the strain rates,  $S_{ij} = \frac{1}{2}(\frac{\partial u_i}{\partial x_j} + \frac{\partial u_j}{\partial x_i})$ , assuming the Newtonian viscous fluid deformation-rate law obtained by analogy with Hookean elasticity. The simplest assumption for the variation of viscous stress with strain rate is a linear law, and was first made by Stokes in 1845 under the following three postulates [41]:

- The fluid is continuous, and its stress tensor,  $\tau_{ij}$ , is at most a linear function of the strain rates  $S_{ij}$ ,
- The fluid is isotropic, i.e., its properties are independent of direction. Thus, the deformation law is independent of the coordinate axes in which it is expressed,
- When the strain rates are zero, the deformation law must reduce to the hydrostatic pressure condition,  $\tau_{ij} = -p\delta_{ij}$ , where  $\delta_{ij}$  is the Kronecker delta function equal to 1 if  $i = j$  and 0 if  $i \neq j$ .

The resulting deformation law is satisfied by all gases and most common fluids. Stokes last postulate allows to include pressure forces into the surface forces giving a constitutive relationship for a newtonian, i.e. linear, viscous fluid as follows:

$$\tau_{ij} = -p\delta_{ij} + \mu \left( \frac{\partial u_i}{\partial x_j} + \frac{\partial u_j}{\partial x_i} \right) + \delta_{ij} \lambda \text{div} \vec{V}, \quad (6)$$

where  $\lambda$ , in linear elasticity, is called Lamé's constant considered as the second coefficient of viscosity [41]. Since this coefficient is associated only with volume expansion, it also called the coefficient of bulk viscosity.

Introducing the viscous stress model into Newton's second law gives the most useful form of the momentum conservation equation for a general linear viscous fluid flow:

$$\rho \frac{D\vec{V}}{Dt} = \rho \vec{g} - \vec{\nabla} p + \frac{\partial}{\partial x_j} \left[ \mu \left( \frac{\partial v_i}{\partial x_j} + \frac{\partial v_j}{\partial x_i} \right) + \delta_{ij} \lambda \text{div} \vec{V} \right], \quad (7)$$

The continuity equation is given by:

$$\frac{D\rho}{Dt} + \rho(\vec{\nabla} \cdot \vec{V}) = 0 \quad (8)$$

describing the changes of density experienced by a fluid particle along its path for a known velocity field. The continuity equation, the momentum equations with Newton's viscosity law, and an energy equation with Fourier's conduction law are commonly referred to as the Navier-Stokes equations. Constitutive relations approximate the observed physical behavior of a material under specific conditions of interest. These additional equations, named equations of state, function of the material of the system allow the determination of extra unknown fields in the balance laws.

### 3.1.2 Incompressible Flow

If we assume that the fluid has a constant density,  $\rho$ , which leads to the disappearance of The term  $\text{div} \vec{V}$  due to the continuity equation along with the coefficient  $\lambda$ , a constant dynamic viscosity,  $\mu$ , a constant Specific heat capacity,  $C_p$ , and a constant

thermal conductivity,  $k$ , we obtain the following simplified Navier-Stokes equation:

$$\rho \frac{D\vec{V}}{Dt} = \rho \vec{g} - \vec{\nabla} p + \mu \vec{\nabla}^2 \vec{V} \quad (9)$$

The most useful form of the Navier-Stokes equations for the development of the finite volume method is, in x-, y-, z-directions with  $\vec{g} = (0, 0, -g)$ :

$$\frac{\partial u}{\partial x} + \frac{\partial v}{\partial y} + \frac{\partial w}{\partial z} = 0 \quad (10)$$

$$\rho \frac{Du}{Dt} = -\frac{\partial p}{\partial x} + \mu \frac{\partial^2 u}{\partial x^2} + \mu \frac{\partial^2 u}{\partial y^2} + \mu \frac{\partial^2 u}{\partial z^2} \quad (11)$$

$$\rho \frac{Dv}{Dt} = -\frac{\partial p}{\partial y} + \mu \frac{\partial^2 v}{\partial x^2} + \mu \frac{\partial^2 v}{\partial y^2} + \mu \frac{\partial^2 v}{\partial z^2} \quad (12)$$

$$\rho \frac{Dw}{Dt} = -\frac{\partial p}{\partial z} + \mu \frac{\partial^2 w}{\partial x^2} + \mu \frac{\partial^2 w}{\partial y^2} + \mu \frac{\partial^2 w}{\partial z^2} - \rho g \quad (13)$$

By doing some derivations and mathematical manipulations we can obtain the conservative form of the N.-S. equations in terms of vectors, with the left hand side written in terms of the mass and momentum fluxes instead of the velocity components:

$$\vec{\nabla} \cdot (\rho \vec{V}) = 0, \quad (14)$$

$$\frac{\partial(\rho u)}{\partial t} + \vec{\nabla} \cdot (\rho u \vec{V}) = -\frac{\partial p}{\partial x} + \mu \nabla^2 u, \quad (15)$$

$$\frac{\partial(\rho v)}{\partial t} + \vec{\nabla} \cdot (\rho v \vec{V}) = -\frac{\partial p}{\partial y} + \mu \nabla^2 v, \quad (16)$$

$$\frac{\partial(\rho w)}{\partial t} + \vec{\nabla} \cdot (\rho w \vec{V}) = -\frac{\partial p}{\partial z} + \mu \nabla^2 w - \rho g, \quad (17)$$

with  $\nabla^2 = \frac{\partial^2}{\partial x^2} + \frac{\partial^2}{\partial y^2} + \frac{\partial^2}{\partial z^2}$ .

### 3.1.3 Viscous Fluid Flow Boundary Conditions

In modeling, the role of boundaries is not simply that of a geometric entity, but an integral part of the solution and numerics through boundary conditions or inter-boundary connections. The topic of boundaries is relevant to the discussions on meshes, fields, discretization, computational processing, etc.[18]. The difference between one fluid flow situation and another is function of the boundary conditions since the equations of motion require mathematically tenable and physically realistic boundary conditions [25].

Three types of boundary conditions are encountered when solving for some variable  $\phi$  on a region:

- The exact or Dirichlet conditions where we can specify  $\phi = f$  on the region boundary, and  $\phi$  can be a constant or a function
- The derivative or Neumann conditions where the derivative of the variable is specified on the region boundary as  $\frac{\partial\phi}{\partial n} = f$ ,
- Mixed conditions or Robin problem where you can specify both the value and their derivative on the region boundary as  $\frac{\partial\phi}{\partial n} + k\phi = f$ , or  $\phi$  can be prescribed on a portion of the region boundary and its derivative on the remaining portion.

## 3.2 Gas Turbines

### 3.2.1 Gas Turbine Composition

A gas turbine is an integrated system consisting of three main components coupled in series:

- A compressor;

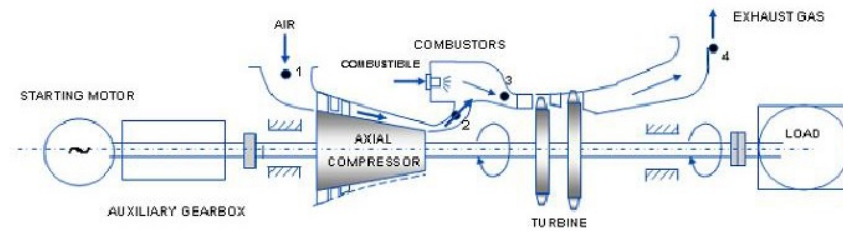


Figure 4: Gas turbine components (Courtesy of GE)

- A combustor; and
- A turbine.

A schematic of a single shaft General Electric (GE) gas turbine is shown in figure 4:

The overall objective of these creatively combined devices is to develop mechanical power at a shaft that is free to rotate, and drive devices such as alternators for power generation applications. The optimized design of such complex systems is generally subject to some constraints such as minimum total cost, plant floor occupation, and reduced maintenance cost and time.

### 3.2.2 Diffusers

#### 3.2.2.1 General Considerations

A diffuser is an expanding duct with the purpose of recovering static pressure from a flowing fluid, by converting a portion of the kinetic energy of the flow into the potential energy of pressure while reducing the fluid stream velocity head. An efficient diffuser will convert the highest possible percentage of kinetic energy into static pressure within a given restriction on diffuser length or expansion ratio. Any losses occurring during this conversion process are manifested as a fall in total pressure

throughout the diffuser [2].

In heavy-duty gas turbines, diffusers are used in several locations, i.e., at the GT compressor outlet, upstream of the combustion chamber, and at the turbine exit. The diffuser use upstream of the combustor is intended to reduce air velocity and thus stabilize the combustion and maximize compressor pressure rise for a given work input. Its use after the turbine recovers pressure, and simultaneously increases the turbine pressure ratio, power output, and efficiency. The diffuser flow behavior and performance are strongly linked to the adjacent components [35]. Variations in static pressure in a cross section are generally large just downstream of the turbine or compressor outlet guide vanes [17].

### 3.2.2.2 Diffuser Characterization

Three geometric parameters may completely describe a diffuser geometry [17] as can be seen in figure 5:

- The area ratio,  $AR$ , directly related to the primary function of the diffuser in achieving a prescribed reduction in velocity;
- A characteristic nondimensional length defining, in combination with the area ratio, the overall pressure gradient, principal factor in boundary-layer development. It is defined by dividing either the wall length,  $L$ , or the axial length,  $N$ , by a representative inlet dimension;
- The divergence angle,  $2\theta$ , related to the other parameters.

For the general case of annular diffuser, the area ratio,  $AR$ , is expressed by [13] as:

$$AR = \frac{1 + 2\frac{L}{R_o} \sin \theta + \left(\frac{L}{R_o}\right)^2 \sin^2 \theta - \left(\frac{R_{i2}}{R_o}\right)^2}{1 - \left(\frac{R_{i1}}{R_o}\right)^2} \quad (18)$$

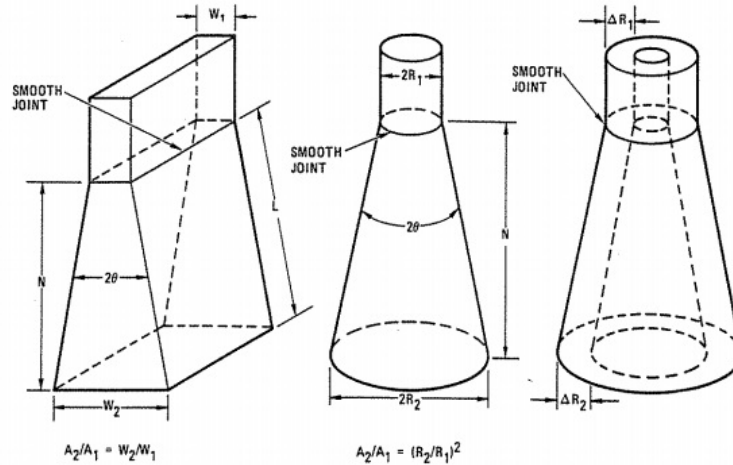


Figure 5: Two-dimensional, conical, and annular straight-walled diffuser characterizations [2]

where the subscripts  $o$  and  $i$  respectively denote *outer* and *inner*, and 1 and 2 the *inlet* and *outlet*.  $L$  in the annular diffuser is the average wall length. The area ratio general expression can be reduced to that of conical diffuser by considering the inlet radii  $R_i = 0$ , and to that of two-dimensional flat-walled diffuser by further neglecting the second-order term. Defining the diffuser geometry in this fashion allows the performance characteristics of these three diffuser types to be plotted on a single set of coordinate axes or map.

Two-dimensional diffusers have been widely used in combustor development. However, Klein [12] found that measured values of losses and pressure recoveries from these two-dimensional models were inaccurate for the following reasons:

- The boundary layers growing along the side walls and the secondary flows they create have considerable influence on the main flow for which the effects cannot be ignored in two-dimensional models.
- In two-dimensional models, the radial velocity profile diffuses only in the di-

rection of the flow, whereas in a fully annular model it is also diffusing in the circumferential direction creating additional mixing and therefore higher pressure losses.

Though no method exists for accurately predicting the quantitative performance of an arbitrary shape and flow diffuser, Cocanower et al.[4] have described an important class of diffusers, called "Class A", for which the performance can be predicted with reasonable accuracy, presenting the following characteristics [17]:

- The flow is subsonic, but not necessarily incompressible;
- The inlet Reynolds number is greater than  $2.5 \times 10^4$  to avoid transition problems;
- The inlet velocity profile is symmetrical;
- Flow within the diffuser is essentially unstalled;
- The diffuser is symmetrical and nonturning; and
- The diffuser is either of two-dimensional, conical or annular geometry.

### 3.2.2.3 Diffuser Performance Criteria

Diffusers performance assessment generally focuses on two objectives [31]:

- The achievement of a given reduction in velocity or increase in pressure, consistent with acceptable internal loss;
- The achievement of stable flow conditions at outlet.

Theoretical aspects of diffuser performance are now being discussed, and four useful parameters for its expression will be derived using the continuity and Bernoulli equations for incompressible axial flow through a 1-D diffuser represented in figure 6 [17], with most of the derivations coming from reference [17]. The flow properties

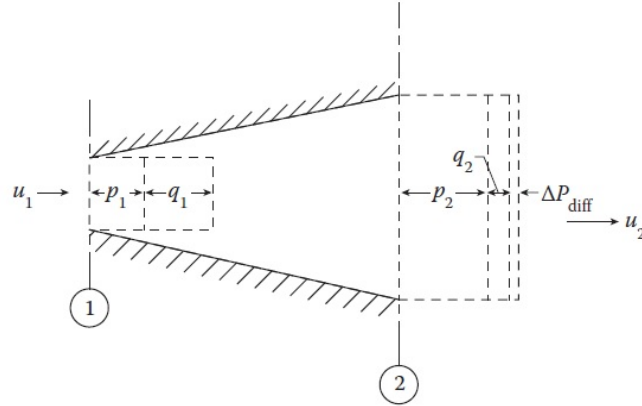


Figure 6: Diffuser energy conversion

change as a function of  $x$  as the fluid flows through the diffuser. Assuming steady-state conditions, uniform entrance and exit flows, and the absence of body forces, the continuity equation is given by:

$$\dot{m} = \rho_1 A_1 U_1 = \rho_2 A_2 U_2 \quad (19)$$

If the fluid density is constant, we get:

$$\dot{m} = A_1 U_1 = A_2 U_2, \quad (20)$$

giving:

$$\frac{A_2}{A_1} = \frac{U_1}{U_2} = AR. \quad (21)$$

where the average axial velocity over a diffuser specific cross section, say  $A$ , is calculated by the following equation:

$$U = \frac{1}{A} \int_A u \, dA, \quad (22)$$

As for the Bernoulli equation, which is written along a streamline, we have from figure 6:

$$p_1 + q_1 = p_2 + q_2 + \Delta P_{diff}, \quad (23)$$

with  $q_i = \frac{1}{2}\rho U_i^2$  and  $p_i$  respectively, the dynamic pressure and the static pressure at cross sections 1 or 2, and  $\Delta P_{diff} = P_1 - P_2$ , the total pressure loss, which includes both the internal energy loss and the effects of redistribution of velocity between inlet and outlet, with the total pressure at a specific cross section expressed as  $P = p + q$ . The mean velocity,  $U_i$ , at that cross section is obtained directly from the continuity equation (19) as:

$$U = \frac{\dot{m}}{\rho A} \quad (24)$$

From equations (21) and (23) the rise in static pressure is obtained as:

$$p_2 - p_1 = q_1 \left[ 1 - \frac{1}{AR^2} \right] - \Delta P_{diff}, \quad (25)$$

From this equation we shall derive now the four parameters expressing diffuser performance.

The Actual Diffuser Pressure-Recovery Coefficient: For flow through a diffusing duct, the actual recovery of static pressure is specified with respect to the kinetic energy of the mean flow at the diffuser inlet, through an experimentally determined static pressure recovery coefficient given by [17]:

$$C_p = \frac{p_2 - p_1}{q_1} = \left[ 1 - \frac{1}{AR^2} \right] - \frac{\Delta P_{diff}}{q_1}, \quad (26)$$

It describes how much of the available kinetic energy or dynamic pressure,  $q_1$ , is

actually converted into static pressure. The static pressure recovery coefficient,  $C_p$ , is generally function of:

- The diffuser geometry,
- The conditions at the diffuser inlet, such as the inlet boundary layer profile, the inlet Reynolds number, the inlet flow profile, and
- The conditions at the diffuser exit, i.e. the exit flow profile.

In addition to the viscous dissipation and velocity peaking in the outlet stream that reduce the actual static pressure recovery, there exists another loss of kinetic energy, that of the exiting stream when a diffuser is discharging into a large reservoir of still fluid [2]. The diffuser performance generally decreases with increasing inlet boundary layer thickness and this can be varied by changing the length of the inlet ducting into the diffuser [2].

**The Ideal Diffuser Pressure-Recovery Coefficient:** If from equation (25) we consider  $\Delta P_{diff} = 0$ , i.e. no friction losses in an ideal diffuser, and for uniform entrance and exit flows, the ideal or theoretical coefficient static pressure rise can be defined as:

$$C_{p_{ideal}} = \frac{(p_2 - p_1)_{ideal}}{q_1} = \left[1 - \frac{1}{AR^2}\right], \quad (27)$$

This coefficient depends only on the area ratio.

**The Diffuser Overall Effectiveness:** The diffuser overall effectiveness is defined as the ratio,  $\eta$ , of the actual diffuser performance, i.e. the measured static pressure recovery coefficient  $C_p$ , and the theoretical ideal static pressure recovery coefficient  $C_{p_{ideal}}$ :

$$\eta = \frac{C_{p_{measured}}}{C_{p_{ideal}}}, \quad (28)$$

Typical values are between 0.5 and 0.9 depending on the geometry and the flow conditions [17].

The Diffuser Total Pressure Loss Coefficient: The last performance parameter is the diffuser total loss coefficient,  $\lambda$ , which is largely diffuser-type dependent, and defined by the change in total pressure through the diffuser [2]:

$$\Delta P_{diff} = P_1 - P_2 = p_1 + \frac{1}{2}\rho U_1^2 - (p_2 + \frac{1}{2}\rho U_2^2) = \frac{1}{2}\rho U_1^2 \lambda. \quad (29)$$

The equation (29) can be re-written as:

$$(p_1 - p_2) + \frac{1}{2}\rho U_1^2 (1 - (\frac{U_2}{U_1})^2) = \frac{1}{2}\rho U_1^2 \lambda \quad (30)$$

From the continuity equation (19), substituting  $(\frac{U_2}{U_1})^2$  by  $(\frac{A_1}{A_2})^2$ , and dividing the whole equation by  $\frac{1}{2}\rho U_1^2$  we get, after replacing  $\frac{p_1 - p_2}{\frac{1}{2}\rho U_1^2}$  by  $-C_p$ :

$$\lambda = 1 - (\frac{A_1}{A_2})^2 - C_p, \quad (31)$$

relating the total loss coefficient  $\lambda$  to the pressure recovery coefficient  $C_p$ . Typical values are around 0.15 for aerodynamically clean faired diffusers to around 0.45 for dump diffusers. For vortex-controlled diffusers (VCD), values range from 0.05 to 0.15.

For a diffuser with a free discharge into a large reservoir, which is the most common diffuser application,  $A_2 = \infty$  we get:

$$\lambda = 1 - C_p. \quad (32)$$

And for a perfect diffuser,  $C_p = 1$  and  $\lambda = 0$  [2].

The pressure loss is composed of the following components as shown in figure 7:

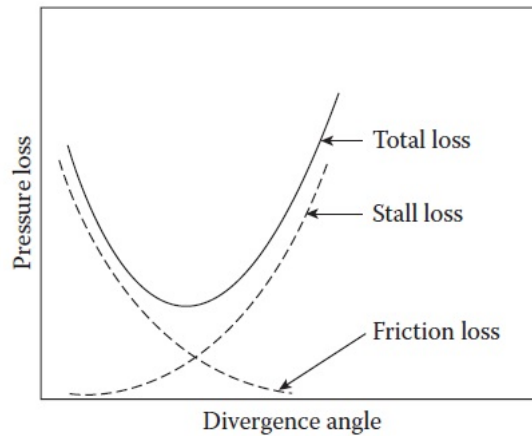


Figure 7: Diffuser pressure loss function of divergence angle [17]

- The dissipation due to wall shear or skin friction along the walls;
- The stall or mixing loss from boundary-layer separation; and
- The leaving momentum loss or the excess of kinetic energy leaving the diffuser above the kinetic energy obtained with a one-dimensional exit-velocity

Above a certain diffuser divergence angle, mixing losses are known to be an order of magnitude higher than those due to skin friction alone. However the leaving loss, coming from the nonuniformity of the velocity profile at the exit, increases smoothly and slowly as a function of the divergence angle corresponding to an exit-velocity profile of an unstalled flow pattern. Furthermore, any stall occupying an appreciable area of the exit plane, on average over both time and space, will increase the leaving loss inversely as the square of the effective area [13]. The wall shear dissipation in the flow and the leaving loss, which in general can be recovered downstream, constitute what is called the head loss.

The Kinetic-Energy Coefficient or Flux Profile Factor: If for a diffusing duct control volume bounded by the diffuser interior walls we consider the following assumptions [2]:

- The changes in internal energy,  $e$ , are neglected, i.e., viscous dissipation is neglected;
- The static pressure is uniform over each diffuser cross-sectional area,  $A$ , corresponding to experimental observation; and
- The attention is restricted to components of flow parallel to the centerline of the diffuser,

the axial flow velocity varies from zero at the diffuser walls to a peak value along the centerline. This velocity distribution is characterized by a kinetic-energy coefficient, also known as kinetic-energy flux profile factor, defined as :

$$\alpha = \frac{1}{A} \int_A \left(\frac{u}{U}\right)^3 dA, \quad (33)$$

which generally vary along the diffuser axis, and where  $u$  is the local velocity at a specific radius and  $U$  the maximum at the considered cross section. This coefficient represents the the ratio of the transport of fluid kinetic energy, passing through the diffuser cross section of area  $A$ , to the minimum possible transport of fluid kinetic energy at the same mass flow [2].

For non-uniform flows where the kinetic energy flux is greater than for uniform flow conditions, for the same flow rate, the velocity profile energy coefficient is defined as:

$$\alpha = \frac{\int_A \frac{1}{2} u^2 \rho u dA}{\frac{1}{2} U^2 \dot{m}} \quad (34)$$

The minimum value is  $\alpha = 1$ , corresponding to completely uniform flow and increases as the flow becomes peaked up to around 2.0 for flow on the verge of separation. For fully developed turbulent flow  $\alpha$  is about 1.05 [17]. By minimizing the peak of the diffuser exit flow, i.e. minimum  $\alpha$ , the kinetic energy exiting the diffuser will be minimized and, by conservation of energy, the pressure recovery will be maximized.

This coefficient may be incorporated into equation (23) giving:

$$p_1 + \alpha q_1 = p_2 + \alpha q_2 + \Delta P_{diff}, \quad (35)$$

As earlier, from this equations we can derive the relevant performance parameters when nonuniformity exists at the diffuser cross section exit. Thus:

$$C_{P_{ideal\ non-uniform\ flow}} = \alpha_1 - \alpha_2 \left(\frac{A_1}{A_2}\right)^2 = \alpha_1 - \alpha_2 \left(\frac{1}{AR}\right)^2, \quad (36)$$

This relation shows that the diffuser pressure recovery is strongly influenced by the flow profiles at the entrance and exit of the diffuser through the profile parameter  $\alpha$ . For uniform flow profiles,  $u = U$  and  $\alpha_1 = \alpha_2 = 1$ . Equation (36) implies that the pressure recovery is maximized by increasing  $\alpha_1$ , therefore increasing the peakedness of the inlet profile, and by minimizing  $\alpha_2$ , hence making the outlet flow as uniform as possible. However, the typical situation is just the opposite since viscous friction at the diffuser walls peaks the exit profile and increases  $\alpha_1$  over  $\alpha_2$ . The extreme situation of a peaked exit flow profile corresponds to jet flow where the flow separates from the walls near the diffuser throat and maintains a uniform narrow jet through the diffuser[2]. By considering (33), it can easily be shown that for an uniform jet of velocity  $U_1$  over area  $A_1$ ,  $\alpha_1 = 1$  and  $\alpha_2 = (A_2/A_1)^2$ . In this case, the corresponding

pressure recovery is zero with  $p_1 = p_2$ . The diffuser efficiency is thus reduced to zero, demonstrating that the effectiveness is largely governed by the degree to which the flow conforms to the diffuser walls [2]. As for the other performance parameters, they are derived here respectively as the non-uniform profile pressure recovery, overall effectiveness, and loss coefficient:

$$C_{p_{non-uniform\ flow}} = \frac{p_2 - p_1}{\alpha_1 q_1}; \quad (37)$$

$$\eta_{non-uniform\ flow} = \frac{p_2 - p_1}{q_1(\alpha_1 - \frac{\alpha_2}{AR^2})}; \quad (38)$$

$$\lambda_{non-uniform\ flow} = C_{p_{ideal\ non-uniform\ flow}} - C_{p_{non-uniform\ flow}}. \quad (39)$$

### 3.3 Boundary Layer Characteristics

#### 3.3.1 Boundary Layer Separation or Stall

Prandtl showed that separation is caused by excessive momentum loss near the wall, in a boundary layer trying to move downstream against increasing pressure, and positive  $dp/dx$ , called adverse pressure gradient, that opposes the flow [42]. This harmful pressure gradient, whose size depends on how large the diffuser angle is, decelerates and rapidly thickens the boundary layer causing its separation from the diffuser wall. The boundary layer separation will then form appreciable regions of unsteady separated eddying flow that blocks the main diffuser flow and often resulting in severe asymmetry and unsteadiness of the exit flow. The described flow condition is called diffuser stall, and can be delineated into regimes as we shall see in the next section, for the case of two-dimensional straight-wall diffusers. The rear of blunt-body flow and airfoil aerodynamics are also typical examples of this phenomenon characterized

by backflow, increased losses, degraded diffuser pressure recovery, disruption of the air flow with attendant loss of properties, and affected diffuser exiting flow profile.

The diffuser stall is function the following main parameters [2]:

- The diffuser geometry, since the regimes of diffuser flow are given as function of this parameter,
- The diffuser inlet conditions,
- The diffuser exit conditions,
- The Reynolds number, and
- The Mach number.

Predictions using boundary-layer theory and related methods are valid only up to the separation point, after which the theory is invalid [42]. Thus experimentation or numerical simulations using turbulence modeling can be used to predict flows in stalled regions, and to analyze the strong interaction effects caused by separated flows.

According to Stevens [31], diffuser flows theoretical analysis is a problem concerned with the calculation of the rate of growth of a turbulent boundary layer, for which the development of the boundary layer itself allows the determination of pressure, contrary to the case of a body surrounded by a free stream where the pressure is determined by the frictionless external flow. Thus, in calculating diffuser flows the pressure distribution is unknown and only obtained when calculating the boundary layer, which constitutes one of the main difficulties. Many existing methods make the assumption of a potential core throughout the diffuser length, which is not the case in many applications where the boundary layers may merge, as for the case of unstalled flows in conical diffusers where the boundary layers meet in the middle.

The static pressure gradient, in this case, is expressed by Bernoulli's equation along the streamline of maximum velocity by the following equation [31]:

$$\frac{dp_t}{dx} = \frac{dp}{dx} + \rho U \frac{dU}{dx} \quad (40)$$

### 3.3.2 Diffuser Flow Regimes

Stall flow patterns, in flat two-dimensional diffusers with straight walls, have been conveniently divided into four regimes of flow in a systematic study done by S. J. Kline and his co-worker Carl A. Moore [23]. By holding the inlet-flow conditions, the wall length, and the throat width and continuously increasing the diffuser-divergence angle, the following flow regimes were found [13]:

- A region of *no appreciable stall* or apparently unstalled flow: The main flow here is well behaved and apparently unseparated
- A region of *large transitory stall* in which the separation varies in position, size, and intensity with time. Eddies are formed along the diffuser with some in close proximity to the wall, assisting the diffusion process by transporting lethargic air away from the boundary layer and replacing them with more energetic air from the main core flow [17]. This regime is characterized by highly pulsating flows with eddies associated with formed stall, subsequently washed out in quasi-periodic fashion. The average stall-washout time cycle varies about a typical mean period called *mean stall period* which is a valid estimate of the average period of 100 or more stall-washout events [2].
- A region of *fully developed stall*: In this regime, a major portion of the diffuser is filled with a large triangular-shaped turbulent recirculation region extending

from the diffuser exit to a position close to the diffuser throat with the main flow following along one wall continuously, and relatively smoothly

- A *jet-flow* region in which the main flow is separated from both walls with the separation beginning slightly downstream from the throat. this occurs only at quite high angles of divergence, and the flow does not reattach until well downstream from the diffuser

### 3.4 The Effects of Diffuser Inlet Flow Conditions

It has been understood very early that the diffuser inlet conditions have some influence on the flow development within the diffuser, the flow stability, and thus the diffuser performance. It is very crucial to simulate compressor or turbine efflux conditions as closely as possible, in terms of velocity profile and angle of swirl, during experimental, as well as CFD modelings [17]. Some of these diffuser inlet conditions are the inlet swirl, the Reynolds number, turbulence, the Mach number, the wakes produced by compressor outlet blade vanes or the turbine last stage, and the radial distribution of velocity at the compressor and turbine exits.

#### 3.4.1 The Influence of Swirl

In combustor diffusers, swirl is generally regarded as undesirable due to its detrimental effect on temperature pattern factor at the turbine inlet. However, it has been found that, for wide-angled diffusers, swirl can suppress flow separation, although not much evidence is available on its effects on diffuser performance [17]. Lohmann et al. [19], showed that inlet swirl angles can increase as the flow is diffused due to the decrease in axial velocity. Furthermore, Carrotte et al. [3], showed, in their detailed

measurements on a modern dump diffuser, that small amount of inlet swirl of about  $3^\circ$ , value typical of gas turbine engines, resulted in the generation of large swirl angles of about  $15^\circ$  further downstream.

### 3.4.2 The Reynolds Number Influence

Reynolds number influence is most pronounced when the inlet boundary layer is not fully developed, and its increase will improve performance by reducing the boundary layer thickness and increasing the turbulence level until the performance becomes insensitive to Reynolds number variations [17]. Klein [12] found that for conical diffusers, Reynolds number should be larger than  $3 \times 10^5$  at the diffuser inlet. As for annular diffusers, it is believed that Reynolds number has little or no effect on performance for  $Re$  greater than  $5 \times 10^4$ , based on the hydraulic mean diameter at inlet. For dump diffusers  $Re$  should be between  $9.2 \times 10^4$  and  $1.6 \times 10^5$  according to Hestermann et al.[8]. However, in real gas turbines Reynolds number values are in the order of several millions and turbulence levels high, making the diffuser to be insensitive to Reynolds number.

### 3.4.3 The Turbulence Influence

Moore and Kline [23], who were among the first to study turbulence influence on the performance of two-dimensional diffusers, showed that even though turbulence has little effect on the line of first stall, the divergence angle at which fully developed stall occurs is significantly increased. Hoffmann et al. [9] later showed that increasing the turbulence intensity up to 3.5% can improve considerably the diffuser performance. The pressure recovery coefficient has been improved from 0.53 to 0.71 by an increase

in turbulence level on a diffuser of  $N/W_1$  ratio of 15, with a divergence angle of 20. Furthermore, Stevens and Williams in [30], found that the flow stability at the diffuser exit was improved by increasing the turbulence intensity of an annular diffuser with constant inner diameter. Lakshminarayana and Reynolds showed in [16], that the generated turbulence is beneficial to diffuser performance with larger improvements using grid- or spoiler-generated turbulence of the same intensity, due to the fact that a compressor-generated turbulence has a large component in the radial direction.

#### 3.4.4 The Mach Number Influence

For incompressible flows, i.e. Mach number below 0.3, the flow characteristics and performance of diffusers are insensitive to Mach number [17]. However, compressibility effects gain practical significance for Mach number greater than 0.6, where the pressure gradient near the inlet of a straight-walled diffuser increases to the point of deteriorating the performance, and large scale separation occur around 0.7, greatly reducing performance. But between 0.4 and 0.6 performance can slightly improve, with much of the pressure recovery occurring very close to the diffuser inlet allowing a settling of the flow downstream [17].

### 3.5 The Engineering Design Process

#### 3.5.1 Design General Considerations

Kline et al. in [13] discuss the two basic problems encountered in the design of straight-walled diffusers, i.e.:

- The prediction of the overall flow regime;
- The design of optimum straight-walled diffusers.

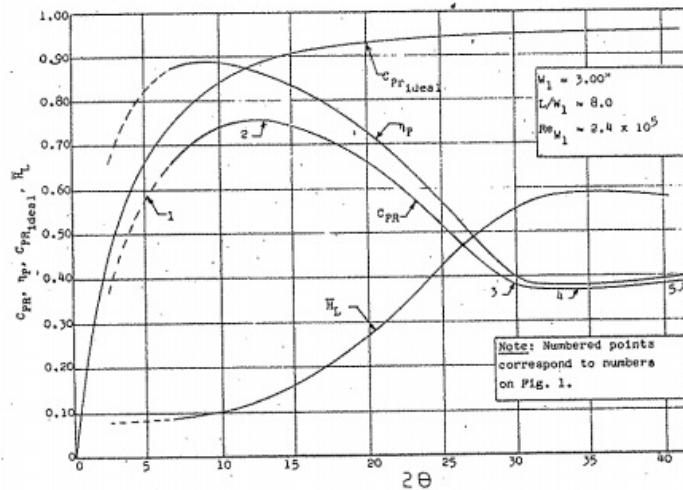


Figure 8: Typical diffuser performance curves: Rectangular diffuser, Cochran [13]

To resolve these problems, engineering analyses or studies predicting relevant characteristics using experimental information, the underlying theory, and adequate methods, either experimental, exact or approximate, are required. There exists a correlation of flow regime with the location on performance curves that can show where optimum recovery occurs for a specific flow regime. Typical diffuser performance curves of a rectangular diffuser obtained by Cochran are represented in figure 8, showing that at constant length, optimum recovery occurs at or slightly above the border between no appreciable stall and large transitory stall [13]. Considering the same figure from a design point of view:

- The regions between points 2 ( $12.5^\circ$ ) and 3 ( $30^\circ$ ) are characterized by large pulsations and very unsteady flow;
- The flows above point 4 (about  $35^\circ$ ) are much steadier, but with some fluctuations;
- Properly designed flat short-vane systems can be used to advantage and provide,

in the regime of fully developed stall where the recovery curve passes through a minimum, good recovery, smooth flow, and uniform exit-velocity profiles for divergence angles of at least  $45^\circ$  (point 5), where larger divergence angles may be better than intermediate values.

The figure also shows that the curve of pressure effectiveness,  $\eta_p$ , has its maximum at an appreciably smaller divergence angle than that of maximum recovery curve as demonstrated in [13]. For optimal design of simple passages, there are many optimum problems that can be formed. However, the authors in [13] defined the four most important optimum problems commonly encountered, each having a different optimum location, and the methods of their prediction as follows:

- Minimum loss of total pressure is desired for a given pressure rise;
- Maximum recovery for a given area ratio is desired regardless of length in the flow direction.
- It is desired to design for optimum recovery within a given length in the direction of flow.
- Optimum recovery for any possible geometry is desired for the given inlet conditions and this can be called the best optimum.

In diffuser design, usually the overall length or the area ratio are the two constraints that the designer encounter. The solutions to two common design problems are represented in figure 9 by the two dashed lines that lie at or near the range of onset of stall [2], with:

- $Cp^*$ , representing the locus of points defining the diffuser area ratios producing

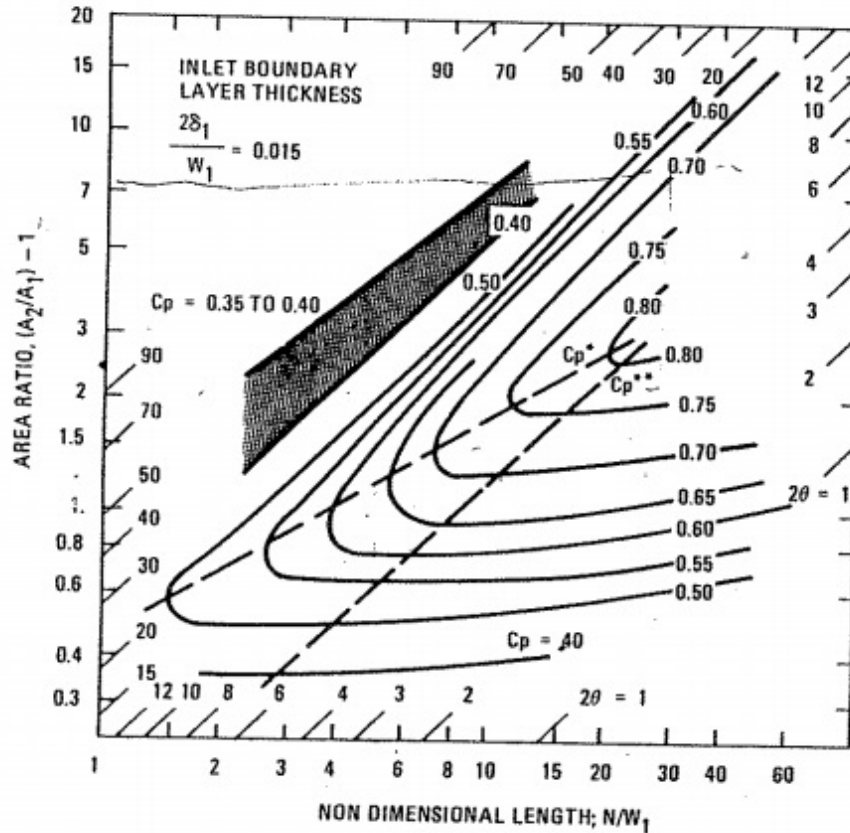


Figure 9: Solutions to two common design problems: Static pressure recovery coefficient  $C_p$  [2]

the maximum static pressure recovery given the nondimensional length, i.e. the ratio of overall length to inlet width, and

- $C_p^{**}$ , the locus of points defining the diffuser nondimensional lengths that produce the maximum recovery given a prescribed area ratio, i.e. the ratio of outlet to inlet area, with  $C_p^{**}$  generally below  $C_p^*$  for all diffuser types.

The best optimum for any geometry for given inlet conditions, which is the best of all optima, can be approximately predicted by taking a total divergence angle around  $7^\circ$  and  $L/W_1$  of 25 to 30. This represents the intersection of the line of minimum loss

per unit of actual pressure rise located at  $7^\circ$ , which is a balance between wall friction loss and mixing loss, with the line of maximum length possible without large stalls, representing the largest area ratio achievable. For short, wide-angle diffusers, like ours, the performance can often be considerably improved by installing vanes that subdivide the diffuser into a series of stall-free diffusing passages. The vanes produce much smaller divergence angles and area ratios so that the resulting passages operate at near-optimum pressure recovery, even though the vaneless diffuser operates in the regime of stall or jet flow.

Experiments show that using vanes in badly stalled diffusers, or operating in jet flow regime, has [2]:

- Increased pressure recovery by as much as a factor of 2,
- Produced much steadier exit flow, and
- Yielded uniform exit flow with as much as a factor of 2 reduction in the peak to average flow velocity.

### 3.5.2 Diffuser Types

#### 3.5.2.1 Aerodynamic or Faired Diffusers

The primary objective of a "faired" type of diffuser is to achieve a gradual reduction in flow velocity without inducing flow separation, i.e. stall, with minimum loss in pressure [17]. Ordinarily, the designer is constrained by the overall length or area ratio [2]. Diffusers can include a settling section allowing to dissipate the large radial and circumferential flow distortions existing at the compressor or turbine efflux, where the flow velocity can be maintained constant, resulting in weaker flow distortions.

However, according to Klein and other workers the resulting weaker flow distortions will decay at a slower rate than when their level is high, arguing that a settling length offers no advantage. Arthur Lefebvre [17], affirms that the great attribute of faired diffuser, i.e. low pressure loss of about one-third less than in dump diffuser, is more than offset by the following drawbacks, preventing its application to modern aircraft engines:

- Excessive length and weight;
- Performance and flow stability are very sensitive to changes in inlet velocity profile;
- Performance is very susceptible to thermal distortions and manufacturing tolerances.

### 3.5.2.2 Dump Diffusers

The dump diffuser, however, may consist of a short conventional diffuser, responsible for nearly all the static pressure rise, reducing the air velocity by about 40% before dumping the flow in complete disregard for conventional diffuser principles. Most of the loss in total pressure occurs in the dump and settling regions. Sudden expansion at the prediffuser outlet is likely to cause higher pressure loss and standing vortices. Contrary to faired diffuser, the dump diffuser produces a stable flow pattern fairly insensitive to manufacturing tolerances, differential thermal expansions between the liner and combustor casing, and variations in inlet velocity profile [17]. Studies showed that liner presence and gap dump reduction to some optimum value tend to suppress flow separation in the prediffuser allowing larger divergence angles and area ratios.

Experimental studies showed that splitter vanes used to obtain near-optimum pressure recoveries and unstalled flow, by creating multiple passages within a diffuser, can be applied in diffusers with a total divergence angle up to  $50^\circ$ , reducing the diffuser length as compared to annular diffuser of the same area ratio. Splitter vanes also improved the outlet velocity profile by making it more uniform [5].

### 3.5.2.3 Vortex-Controlled Diffusers (VCD)

This type of diffuser allows to achieve rapid and efficient diffusion by bleeding the boundary layer, about 4% of the mainstream flow, at the throat of a sudden expansion. Although the basic mechanism of vortex control is not yet fully understood [17], Adkins et al. [1] have proposed the following model 10, where the application of external suction causes the static pressure in the vortex chamber to fall below that of the main stream, drawing and accelerating "stream a" into the vortex; "stream b" however is decelerated since flowing into a region of greater static pressure. The difference of velocity between the two streams creates a shearing action producing an extremely turbulent layer that inhibits flow separation, and thus achieves diffusion in a very short length, with the effectiveness almost equal to the theoretical optimal value. Vortex-controlled diffusers have great potential for application to gas turbines, and especially to high-temperature engines where bleed air from the combustor allows to cool hot sections downstream [17]. The main advantages are:

- Significant savings in engine length and weight;
- Increased available liner pressure drop improving almost all aspects of combustion performance.

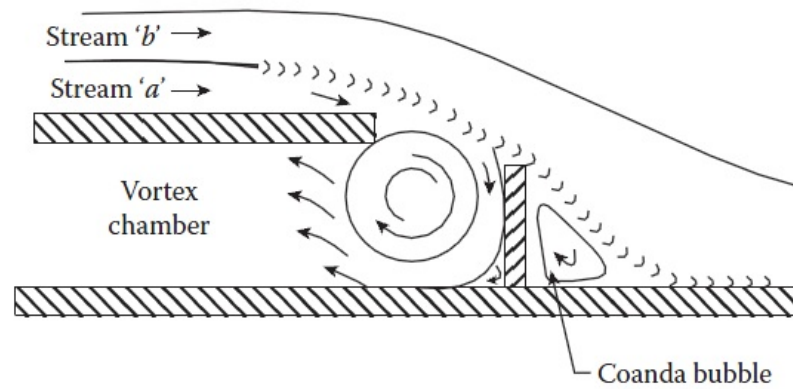


Figure 10: Flow mechanisms of vortex control, Adkins et al. [1]

#### 3.5.2.4 Hybrid Diffusers

Developed by Adkins and co-workers, these diffusers combine a vortex-controlled diffuser, accounting for only a small increase in cross-sectional area with a minimal bleed-off, with a conventional wide-angled postdiffuser at the exit. The turbulent layer generated by the VCD is used to suppress flow separation in the wide-angled diffuser. The hybrid diffuser is capable of giving high pressure recovery even without the bleed of air. However, it cannot be used on most engines since the bleed pressure is too low for turbine blade cooling, and this can be resolved by fitting a short pre-diffuser, with an area ratio between 1.3 -1.4, in front of the vortex-controlled diffuser to raise the bleed air pressure sufficient for turbine cooling. However, this solution has the drawback of adding the length of the diffuser.

#### 3.5.3 The Analysis Phase

The analysis phase, either experimental, theoretical, or numerical can be performed once a specific type of diffuser has been adopted, leading to important predicted characteristics used to make judgement. It is important that the initial diffuser be

tested while the engine is still at an early stage of development [17]. Water flow-visualisation rigs, that can reveal any irregularities in the flow, are ideally suited for this purpose. CFD simulations can provide valuable guidance in the diffuser design and development stages [17].

### 3.6 Turbulence Modeling

#### 3.6.1 Turbulence Definition

Turbulence is defined as a chaotic and random state of motion developing at high Reynolds number flows, in which the velocity and pressure change continuously with time within substantial regions of flow [40]. The flow Reynolds number, a dimensionless viscous flow controlling parameter measuring the relative importance of inertia forces and viscous forces, is given by:

$$Re = \frac{UL}{\nu}, \quad (41)$$

where  $U$  and  $L$  are characteristic velocity and geometric length scales of the mean flow, and  $\nu$  is the fluid kinematic viscosity. The main characteristics of turbulent flows are their random nature, which prevents any economical description of the motion of all the fluid particles, the three-dimensional nature of the turbulent fluctuations, and the rotational flow structures called eddies. Eddies have a wide range of time and length scales that favor an effective mixing and allow high values of diffusion coefficients of mass, momentum, and heat. Furthermore largest turbulent eddies interact with the mean flow and extract energy from it by a process called vortex stretching. Their structure is highly anisotropic, whereas the smallest eddies are

isotropic at high mean flow Reynolds numbers.

### 3.6.2 Time-Averaged N.-S. Equations

Viscous-flow theory has limitations, especially in high Reynolds number turbulent flow regime, where the flow undergoes random fluctuations and is only modeled on a semi-empirical time-mean or statistical basis [42]. For most engineering purposes, it is unnecessary to resolve the details of turbulence fluctuations. Information about the time-averaged properties of the flow, namely, mean velocity, mean pressure, and mean stresses, etc., is satisfactory for CFD users.

Prior to the application of numerical methods, the Navier-Stokes equations are time averaged. Reynolds basic idea is to split the unsteady turbulent flow into a steady mean motion and an unsteady (fluctuating) motion. The mean value is evaluated over a long enough time interval so that it becomes time invariant, consequently the time averaging of fluctuating terms equal to zero. Time averaging produces the steady forms of the N.-S. equations, referred to as RANS equations, which focus on the mean flow and The effects of turbulence on mean flow properties. During this averaging process, extra terms or new variables, specifically shear stresses, appear in the time-averaged flow equations due to the interactions between various turbulent fluctuations or eddies. The complete set of the shear stresses expresses:

- The so-called Reynolds stresses in the three orthogonal directions and
- The "apparent" increase of viscosity due to fluctuating motion in turbulent flow.

The N.-S. equations now contain more unknowns than the number of equations. Ways and means to link these new unknowns with the mean flow have to be found before a solution of the RANS equations is possible. This requires the formulation

of additional equations to close the RANS equations. The closure of the RANS equations with a set of additional equations bears the name turbulence modeling. It is worth mentioning that with this approach, only the effects of turbulent motions on the mean flow are modeled; the fluctuating components of velocity and pressure are not computed! In the RANS approach, multitude of length scales involved in the turbulence are excluded, with an immediate consequence of reducing the computing resources demand.

### 3.6.3 The Modeling of Turbulence

Mathematical modeling is the act of translating a physical problem, or other problems usually of a physical nature, into a mathematical model, i.e. an algebraic equation, a differential equation, or some other mathematical expression [15]. Due to the fact that physical concepts such as velocity and acceleration are derivatives, a mathematical model is very often a differential equation containing total or partial derivatives of an unknown function satisfying the differential equation, and known as its solution.

Turbulence models can be broadly classified into two groups:

- Those based on eddy viscosity concept, where the turbulent eddy viscosity, which is analogous to the physical viscosity, is assumed to be isotropic. This assumption allows the turbulence to be represented as a scalar parameter using a gradient transport approximation. This parameter depends on the local structure of the turbulence, and hence its velocity and length scales.
- Those that attempt to solve for the individual turbulent stresses and fluxes. These

models treat the turbulence as anisotropic, and turbulence is studied as a tensor. The approach is of fundamental importance for the correct description of physical phenomena governing the turbulence transport. .

Most turbulence models based on RANS equations belong to the group of statistical turbulence models based on the eddy-viscosity hypothesis [14].

### 3.6.3.1 Reynolds Stresses

Consider a control volume in a two-dimensional turbulent shear flow in the  $x$ -direction as explained in [40] where most of the treated material comes from. This flow has a mean velocity gradient in the  $y$ -direction. The presence of vortical eddy motions creates strong mixing and random currents, associated with the passage of eddies near the boundaries of the control volume, will transport fluid across its boundaries. Fluid portions transported by the eddies will carry momentum and energy into and out of the control volume. Due to the existence of velocity gradient, fluctuations with a negative  $y$ -velocity will bring fluid portions with higher momentum in the  $x$  direction into the control volume through the top boundary. Across the bottom boundary however, it will transport control volume fluid to a region of slower moving fluid. In the same manner, positive  $y$ -velocity fluctuations will transport slower moving fluid into regions of higher velocity. Ultimately we have a net momentum exchange due to convective transport by the eddies, which causes the faster moving fluid layers to be decelerated and the slower moving layers to be accelerated, causing fluid layers to experience additional turbulent shear stresses called Reynolds stresses. The specific Reynolds-stress tensor, assuming that the Boussinesq approximation is valid, is given

by:

$$\tau_{ij} = 2\nu_t S_{ij} + \frac{2}{3}k\delta_{ij}, \quad (42)$$

where  $\nu_t$  and  $k$  are respectively the turbulent viscosity and the turbulent kinetic energy. In the presence of temperature or concentration gradients, the eddy motions will also generate turbulent heat or species concentration fluxes across the control volume boundaries which will affect the equations for momentum and energy.

### 3.6.3.2 Boussinesq Hypothesis: Eddy viscosity and eddy diffusivity

The eddy-viscosity  $\nu_t$  is incorporated in the RANS equation as follows:

$$-\overline{u_i' u_j'} = \nu_t(x, y, z) \left( \frac{\partial U_i}{\partial x_j} + \frac{\partial U_j}{\partial x_i} \right). \quad (43)$$

The method was first postulated by Boussinesq using an isotropic eddy viscosity assumption. His proposition of Reynolds stresses (1877) states that they might be proportional to mean rates of deformation:

$$\tau_{ij} = -\overline{u_i' u_j'} = \mu_t(x, y, z) \left( \frac{\partial U_i}{\partial x_j} + \frac{\partial U_j}{\partial x_i} \right) - \frac{2}{3}\rho k \delta_{ij}, \quad (44)$$

which is the boussinesq hypothesis where  $\mu_t(x, y, z,)$  is the turbulent or eddy viscosity, and  $\delta_{ij}$  is the kronecker Delta whose value is 1 if  $i = j$  and 0 if  $i \neq j$ .

### 3.6.3.3 The k - $\epsilon$ Turbulence Model

The standard  $k - \epsilon$  model uses the following transport equations for  $k$  and  $\epsilon$ :

$$\frac{\partial(\rho k)}{\partial t} + \text{div}(\rho k \vec{U}) = \text{div} \left[ \frac{\mu_t}{\sigma_k} \text{grad } k \right] + 2\mu_t S_{ij} \cdot S_{ij} - \rho \epsilon \quad (45)$$

$$\frac{\partial(\rho \epsilon)}{\partial t} + \text{div}(\rho \epsilon \vec{U}) = \text{div} \left[ \frac{\mu_t}{\sigma_\epsilon} \text{grad } \epsilon \right] + C_{1\epsilon} \frac{\epsilon}{k} 2\mu_t S_{ij} \cdot S_{ij} - C_{2\epsilon} \rho \frac{\epsilon^2}{k} \quad (46)$$

The right-hand-side represents the modeled form of the principal turbulence physical transport processes. The sum of the two terms on the left-hand side, i.e., the unsteady and the convective terms, is the substantial derivative of  $k$  or  $\epsilon$ , that gives the rate of change of  $k$  or  $\epsilon$  as we follow a fluid particle. These two equations contain five adjustable constants:  $C_\mu$  in  $\mu_t = \rho C_\mu \cdot k^2/\epsilon$ ,  $\sigma_k$ ,  $\sigma_\epsilon$ ,  $C_{1\epsilon}$ , and  $C_{2\epsilon}$ , whose values are gotten from a comprehensive data fitting for a wide range of turbulent flows. So we have  $C_\mu = 0.09$ ;  $\sigma_k = 1.00$ ;  $\sigma_\epsilon = 1.30$ ;  $C_{1\epsilon} = 1.44$ , and  $C_{2\epsilon} = 1.92$ . Prandtl numbers  $\sigma_k$  and  $\sigma_\epsilon$  link the diffusivities of  $k$  and  $\epsilon$  to the eddy viscosity  $\mu_t$ . The pressure term,  $div(-\overline{p'u'})$  in the exact  $k$ -equation cannot be measured directly, but its effect is accounted for within,  $div[\frac{\mu_t}{\sigma_k} grad k]$  of the  $k$  equation. The dissipation rate  $\epsilon$  is large where the production of  $k$  is large. The second equation of the standard  $k - \epsilon$  model assumes that the production and destruction terms are proportional to those of the first equation. These forms ensure that  $\epsilon$  increases rapidly if  $k$  increases rapidly, and that it decreases sufficiently fast to avoid non-physical, negative values of turbulent kinetic energy if  $k$  decreases.

Industrial CFD users rarely have measurements of  $k$  and  $\epsilon$  at their disposal [40]. If no information is available at all, rough approximation for the inlet distributions of  $k$  and  $\epsilon$  in internal flows can be obtain from the turbulence intensity,  $I$ , and characteristic length,  $L$ , of the equipment (equivalent to pipe diameter) by means of the following simple assumed form:

$$k = \frac{2}{3}(U_{ref}I^2), \quad (47)$$

$$\epsilon = C_\mu^{3/4} \frac{k^{3/2}}{l}, \quad (48)$$

with  $l = 0.07L$ .

These are closely related to the mixing length formulas, and the universal distribution near a solid wall are given at high Reynolds numbers by:

$$u^+ = \frac{U}{u_\tau} = \frac{1}{\kappa} \ln(Ey_P^+), \quad (49)$$

$$k = \frac{u_\tau^2}{\sqrt{C_\mu}}, \epsilon = \frac{u_\tau^2}{\kappa y} \quad (50)$$

where  $u_\tau$  is the frictional velocity given by:

$$u_\tau = \sqrt{\frac{\tau_w}{\rho}} \quad (51)$$

and equations (49) and (50) are wall functions relating the local wall shear stress, through  $u_\tau$ , to the mean velocity, turbulence kinetic energy, and the rate of dissipation. Von Karman's constant  $\kappa = 0.41$ , and  $E$  is the wall roughness parameter corresponding to 9.8 for smooth wall. At low Reynolds numbers the log law is not valid, so the above-mentioned boundary conditions cannot be used; there is a need to modify the  $k - \epsilon$  model. It is essential to apply wall damping in order to ensure that viscous stresses take over from turbulent Reynolds stresses at low Reynolds numbers, and in the viscous sub-layer adjacent to solid walls.

Assessment of performance. Advantages:

- The  $k - \epsilon$  model is the simplest turbulence model for which only initial and/or boundary conditions need to be supplied.
- The  $k - \epsilon$  model is the most widely used, validated, and well established turbulence model in both engineering and academia.
- Great results have been achieved in calculating a wide variety of thin shear

layer and recirculating flows without the need for case-by-case adjustment of the model constants.

- It performs particularly well in confined flows where the Reynolds shear stresses are most important, viz., in many industrial engineering flow applications, hence its popularity.
- It can be used to study environmental flows such as pollutant dispersion in the atmosphere and in lakes, and the modeling of fires.

Disadvantages:

- More expensive to implement than the mixing length model, with two extra PDEs
- It shows only moderate agreement in unconfined flows.
- Does not perform well in weak shear layers, specifically far wakes and mixing layers, flows with large extra strains such as curved boundary layers, swirling flows, and diverging passages. In rotating flows, the model is oblivious to body forces due to rotation of the frame of reference, and secondary flows in long non-circular ducts, which are driven by anisotropic normal Reynolds stresses due to the same deficiencies of the treatment of normal stresses within the  $k - \epsilon$  model

#### 3.6.3.4 The RNG $k - \epsilon$ Turbulence Model

A more recent version of the  $k - \epsilon$  model has been developed by Yakhot and Orszag (1986 and 1992) from the instantaneous Navier-Stokes equations, using a mathematical technique called renormalization group (RNG) theory or methods. Here

the model uses a modified coefficient,  $C_{\epsilon 2}$ , appearing in the dissipation rate equation that can also be written as follows:

$$\frac{\partial \epsilon}{\partial t} + U_j \frac{\partial \epsilon}{\partial x_j} = C_{\epsilon 1} \frac{\epsilon}{k} \tau_{ij} \frac{\partial U_i}{\partial x_j} - C_{\epsilon 2} \frac{\epsilon^2}{k} + \frac{\partial}{\partial x_j} \left[ \left( \nu + \frac{\nu_t}{\sigma_\epsilon} \right) \frac{\partial \epsilon}{\partial x_j} \right], \quad (52)$$

and,

$$C_{\epsilon 2} \equiv \tilde{C}_{\epsilon 2} + \frac{C_\mu \lambda^3 (1 - \frac{\lambda}{\lambda_0})}{1 + \beta \lambda^3}, \quad (53)$$

with  $\lambda \equiv \frac{k}{\epsilon} \sqrt{2 S_{ij} S_{ij}}$ . The turbulent kinetic energy is rewritten as:

$$\frac{\partial k}{\partial t} + U_j \frac{\partial k}{\partial x_j} = \tau_{ij} \frac{\partial U_i}{\partial x_j} - \epsilon + \frac{\partial}{\partial x_j} \left[ \left( \nu + \frac{\nu_t}{\sigma_k} \right) \frac{\partial k}{\partial x_j} \right], \quad (54)$$

with  $\nu_t = \frac{C_\mu k^2}{\epsilon}$  and the closure coefficients for the RNG  $k - \epsilon$  model are:

$$C_{\epsilon 1} = 1.42, \tilde{C}_{\epsilon 2} = 1.68, C_\mu = 0.085, \sigma_k = 0.72 = \sigma_\epsilon, \beta = 0.012, \text{ and } \lambda_0 = 4.38.$$

### 3.6.3.5 The $k - \omega$ Turbulence Model

The  $k - \omega$  turbulence model, proposed by Wilcox in 1988, uses the turbulence frequency  $\omega = \epsilon/k$  [ $s^{-1}$ ] as the second variable. The length scale is:  $l = k^{1/2}/\omega$ , and the eddy viscosity is given by  $\mu_t = \rho k/\omega$ . The Reynolds stresses are computed as usual in two-equation models with the Boussinesq expression. The transport equations for  $k$  and  $\omega$  for turbulent flows at high Reynolds are as follows:

$$\frac{\partial(\rho k)}{\partial t} + \text{div}(\rho k \vec{U}) = \text{div} \left[ \left( \mu + \frac{\mu_t}{\sigma_k} \right) \text{grad } k \right] + (2\mu_t S_{ij} \cdot S_{ij} - \frac{2}{3} \rho k \frac{\partial U_i}{\partial x_j} \delta_{ij}) - \beta^* \rho k \omega, \quad (55)$$

where  $P_k = 2\mu_t S_{ij} \cdot S_{ij} - \frac{2}{3} \rho k \frac{\partial U_i}{\partial x_j} \delta_{ij}$  is the rate of production of turbulent kinetic

energy, and

$$\frac{\partial(\rho\omega)}{\partial t} + \text{div}(\rho\omega\vec{U}) = \text{div}\left[\left(\mu + \frac{\mu_t}{\sigma_\omega}\right)\text{grad}\omega\right] + \gamma_1(2\rho_t S_{ij} \cdot S_{ij} - \frac{2}{3}\rho\omega\frac{\partial U_i}{\partial x_j}\delta_{ij}) - \beta_1\rho\omega^2, \quad (56)$$

The constants are given by :  $\sigma_k = 2.0$ ;  $\sigma_\omega = 2.0$ ;  $\gamma_1 = 0.553$ ;  $\beta_1 = 0.075$ ; and  $\beta^* = 0.09$ .

The reason for which the  $k - \omega$  model was initially attracting attention is that the integration to the wall does not require wall-damping functions in flows with low Reynolds numbers. In this model the boundary conditions are specified as:

- $k = 0$  at the wall
- $\omega \rightarrow \infty$  at the wall. However, we can specify a very large value at the wall or, apply a hyperbolic variation  $\omega_p = 6\nu/(\beta_1 y_p^2)$ , according to Wilcox, at the near-wall grid point, P.
- At inlet boundaries:  $k$  and  $\omega$  must be specified,
- At outlet boundaries: the usual zero gradient conditions are used.

The boundary condition of  $\omega$  in a free stream, where  $k \rightarrow 0$  and  $\omega \rightarrow 0$  is the most problematic.  $\mu_t = \rho k/\omega$ ,  $\omega \rightarrow 0$  implies that  $\mu_t$  is indeterminate or infinite. Therefore non-zero value of  $\omega$  must be specified.

Disadvantage: The results of the model depend on the assumed free stream value of  $\omega$ , which is a serious problem in external aerodynamics and aerospace applications where free-stream boundary conditions are used routinely.

### 3.6.3.6 The Menter Shear-Stress Transport (SST) $k - \omega$ Turbulence Model

The Menter SST  $k - \omega$  model is a hybrid turbulence model using:

- a) A transformation of the  $k - \epsilon$  model into a  $k - \omega$  model in the near-wall region,

and

b) The standard  $k - \epsilon$  model in the fully turbulent region, far from the wall. Here, unlike the Wilcox's original model, the  $\epsilon$ -equation is transformed into an  $\omega$ -equation by substituting  $\epsilon$  by  $k\omega$ , while the Reynolds stress computation and the  $k$ -equation are alike. So we have:

$$\frac{\partial(\rho\omega)}{\partial t} + \text{div}(\rho\omega\vec{U}) = \text{div}\left[\left(\mu + \frac{\mu_t}{\sigma_{\omega,1}}\right)\text{grad}\omega\right] + \gamma_2(2\rho S_{ij} \cdot S_{ij}) - \frac{2}{3}\rho\omega \frac{\partial U_i}{\partial x_j} \delta_{ij} - \beta_2\rho\omega^2 + 2\frac{\rho}{\sigma_{\omega,2}\omega} \frac{\partial k}{\partial x_k} \frac{\partial \omega}{\partial x_k}. \quad (57)$$

In this equation we have an extra source term,  $2\frac{\rho}{\sigma_{\omega,2}\omega} \frac{\partial k}{\partial x_k} \frac{\partial \omega}{\partial x_k}$ , which is the cross-diffusion term, arising during the  $\epsilon = k\omega$  transformation of the diffusion term in the  $\epsilon$ -equation. The improvements from modifications to optimize the performance of the SST  $k - \omega$  model based on experience are:

- Revised model constants are:  $\sigma_k = 1.0$ ;  $\sigma_{\omega,1} = 2.0$ ;  $\sigma_{\omega,2} = 1.17$ ;  $\gamma_2 = 0.44$ ;  $\beta_2 = 0.083$ ; and  $\beta^* = 0.09$ .
- Blending functions: used to achieve a smooth transition between the standard  $k - \epsilon$  model in the far field, and the transformed  $k - \epsilon$  model near the wall. These functions modify the cross-diffusion term, and are also used for model constants that take the value  $C_1$  for the original  $k - \omega$  model and  $C_2$  in Menter's transformed  $k - \epsilon$  model.  $C = F_c C_1 + (1 - F_c) C_2$ ;  $F_c = F_c(l_t/y, Re_y)$  is a function of the ratio of turbulence  $l_t = k^{1/2}/\omega$ ,  $y$ , and  $Re_y = y^2\omega/\nu$ .  $F_c = 0$  at the wall;  $F_c = 1$  in the far field, and  $F_c$  produces a smooth transition around a distance half way between the wall and the edge of the boundary layer.
- Limiters: The eddy viscosity is limited to give improved performance in flows

with adverse pressure gradients and wake regions, and the turbulent kinetic energy production is limited to prevent the buildup of turbulence in stagnation regions. So the limiters are:

$\mu_t = a_1 \rho k / \max(a_1 \omega, S F_2)$ , where  $S = (2S_{ij}S_{ij})^{1/2}$ ,  $a_1 = \text{constant}$  and  $F_2$  is a blending function.

$$P_k = \min(10\beta^* \rho k \omega, 2\mu_t S_{ij} \cdot S_{ij} - \frac{2}{3} \rho k \frac{\partial U_i}{\partial x_j} \delta_{ij}). \quad (58)$$

Assessment of performance of turbulence models for aerospace applications

Advantages:

External aerodynamics:

- The Spalart-Allmaras,  $k - \omega$ , and the SST  $k - \omega$  models are all suitable for external aerodynamics.
- The SST  $k - \omega$  model is most general and gives superior performance for zero pressure gradient and adverse pressure gradient boundary layers, free shear layers, and, a NACA 4412 aerofoil.
- However, the original  $k - \omega$  model was best for the flow over a backward-facing step.

Disadvantages:

For general-purpose CFD, the Spalart-Allmaras model is unsuitable, but the  $k - \omega$  and the SST  $k - \omega$  models can both be applied, having both a similar range of strengths and weaknesses as the  $k - \epsilon$  model and fail to include accounts of more subtle interactions between turbulent stresses and mean flow when compared to RSM.

The SST turbulence model, tend to capture a realistic boundary layer without

using wall functions and to avoid the strong sensitivity of the turbulent frequency rate  $\omega$  to freestream condition.

### 3.6.3.7 The Spalart - Allmaras Turbulence Model

This is one of economical methods for aerospace applications, among the more recent advances in turbulence modeling seeking to address shortcomings of two-equation models such as the  $k - \epsilon$  model. The Spalart-Allmaras model is written in terms of a quantity that is a modified form of the turbulent or eddy kinematic viscosity. It involves:

- One transport equation to be solved for the kinematic eddy viscosity parameter  $\tilde{\nu}$ , and
- A specification of a length scale by means of an algebraic formula.

The transported variable in the Spalart-Allmaras model,  $\tilde{\nu}$ , is identical to the turbulent kinematic viscosity, except in the near-wall region affected by viscosity. This model provides economical computations of boundary layers in external aerodynamics. The model includes eight closure coefficients and three closure functions. Its defining equations are as follows:

The Kinematic Eddy Viscosity:

$$\nu_t = \tilde{\nu} f_{\nu 1}. \quad (59)$$

Here, the dynamic eddy viscosity is related to  $\tilde{\nu}$  by  $\mu_t = \rho \tilde{\nu} f_{\nu 1}$ , the modeling of the turbulent viscosity, where  $f_{\nu 1} = f_{\nu 1}(\frac{\tilde{\nu}}{\nu})$ , which is the wall-damping function given by:

$$f_{\nu 1} = \frac{\chi^3}{\chi^3 + C_{\nu 1}^3}, \quad (60)$$

a closure function with  $\chi \equiv \frac{\tilde{\nu}}{\nu}$ .

For high  $Re : f_{\nu 1} \rightarrow 1$ , equation (59) implies that  $\tilde{\nu} = \nu_t$ , and at the wall  $f_{\nu 1} \rightarrow 0$ .

The Reynolds stresses are given by:

$$\tau_{ij} = -\overline{\rho u_i' u_j'} = 2\mu_t S_{ij} = \rho \tilde{\nu} f_{\nu 1} \left( \frac{\partial U_i}{\partial x_j} + \frac{\partial U_j}{\partial x_i} \right). \quad (61)$$

The one transport equation for  $\tilde{\nu}$ , the viscosity parameter, is:

$$\frac{\partial(\rho \tilde{\nu})}{\partial t} + \text{div}(\rho \tilde{\nu} \vec{U}) = \frac{1}{\sigma_\nu} \text{div}[(\mu + \rho \tilde{\nu}) \text{grad}(\tilde{\nu}) + C_{b2} \rho \frac{\partial \tilde{\nu}}{\partial x_k} \frac{\partial \tilde{\nu}}{\partial x_k}] + C_{b1} \rho \tilde{\nu} \tilde{\Omega} - C_{\omega 1} \rho \left( \frac{\tilde{\nu}}{\kappa y} \right)^2 f_\omega. \quad (62)$$

The term  $C_{b1} \rho \tilde{\nu} \tilde{\Omega}$  is the modeling of the turbulent production or rate of production of  $\tilde{\nu}$  and is related to the local mean vorticity as follows:

$$\tilde{\Omega} = \Omega + \frac{\tilde{\nu}}{(\kappa y)^2} f_{\nu 2}. \quad (63)$$

The modeling of the turbulent destruction is  $C_{\omega 1} \rho f_\omega \left( \frac{\tilde{\nu}}{\kappa y} \right)^2$ .

The eddy viscosity parameter equation can also be written as:

$$\frac{\partial(\tilde{\nu})}{\partial t} + U_j \frac{\partial(\tilde{\nu})}{\partial x_j} = C_{b1} \tilde{\Omega} \tilde{\nu} - C_{\omega 1} f_\omega \left( \frac{\tilde{\nu}}{y} \right)^2 + \frac{1}{\sigma} \frac{\partial}{\partial x_k} [(\nu + \tilde{\nu}) \frac{\partial \tilde{\nu}}{\partial x_k}] + \frac{C_{b2}}{\sigma} \frac{\partial \tilde{\nu}}{\partial x_k} \frac{\partial \tilde{\nu}}{\partial x_k}. \quad (64)$$

where the mean vorticity, a scalar measure of the deformation tensor, is  $\Omega = \sqrt{2\Omega_{ij}\Omega_{ij}}$  based, by default, on the magnitude of the vorticity, and  $\Omega_{ij} = \frac{1}{2} \left( \frac{\partial U_i}{\partial x_j} - \frac{\partial U_j}{\partial x_i} \right)$  is the mean vorticity or the mean-rate-rotation tensor, with  $y$  representing the distance from the closest surface.

The functions  $f_{\nu 2} = f_{\nu 2} \left( \frac{\tilde{\nu}}{\nu} \right) = f_{\nu 2}(\chi) = 1 - \frac{\chi}{1 + \chi f_{\nu 1}}$ , and  $f_\omega = f_\omega \left( \frac{\tilde{\nu}}{\bar{\Omega} \kappa^2 y^2} \right) = f_\omega(r) = g \left[ \frac{1 + C_{\omega 3}^6}{g^6 + C_{\omega 3}^6} \right]^{1/6}$  are wall-damping functions with  $g = r + C_{\omega 2}(r^6 - r)$ . In the 2-equation model  $k - \epsilon$ , the length scale is found by combining the two transported quantities  $k$

and  $\epsilon$ :  $l = k^{3/2}/\epsilon$ . However, in the Spalart-allmaras model it cannot be computed, but must be specified to determine the rate of dissipation of the transported turbulence quantity. But,  $\kappa y$  can be used as the length scale and also enters in the vorticity parameter  $\tilde{\Omega}$  equal to the mixing length used to develop the log-law for wall boundary layers.

The model constants are  $\sigma_\nu = 2/3$ ;  $\kappa = 0.4187$ ;  $C_{b1} = 0.1355$ ;  $C_{b2} = 0.622$ ;  $C_{\nu1} = 7.1$ ;  $C_{\omega2} = 0.3$ ,  $C_{\omega3} = 2$ ;  $C_{\omega1} = \frac{C_{b1}}{\kappa^2} \frac{(1+C_{b2})}{\sigma}$ , all these are closure coefficients.

The justification for the default expression of  $\Omega$  is that, for the wall-bounded flows, that were of significant importance and interest when the model was formulated, turbulence is found only where vorticity is generated near walls. However, since one should also take into account the effect of mean strain on the turbulence production, a modification has been proposed combining measures of both rotation and strain tensors in the definition of  $\Omega \equiv |\Omega_{ij}| + C_{prod} \min(0, |S_{ij}| - |\Omega_{ij}|)$ , where  $C_{prod} = 2.0$ ,  $|\Omega_{ij}| \equiv \sqrt{2\Omega_{ij}\Omega_{ij}}$ , and  $|S_{ij}| \equiv \sqrt{2S_{ij}S_{ij}}$ .

When both the rotation and strain tensors are included, it reduces the production of eddy viscosity and consequently reduces the eddy viscosity itself in regions where the measure of vorticity exceeds that of strain rate.

#### Assessment of performance

##### Advantages:

- Gives good performance, compared to measurement, in attached boundary layers with adverse pressure gradients, important for predicting stalled flows. In this case it is as good as algebraic models.
- It is especially attractive for aerofoil and wing applications, for which it has been

calibrated. That is why it has also attracted an increasing following across the turbomachinery community.

- Spalart-Allmaras predictions are satisfactory for many engineering applications..

Disadvantages:

- It is difficult to define the length scale in complex geometries, which is why this model is unsuitable for more general internal flows.
- It lacks sensitivity to transport processes in rapidly changing flows.
- Its failure to accurately reproduce spreading rates for plane, round, and radial jets that are consistent with measurements is a cause for concern, and should serve as a warning that the model has some shortcomings.

Complex flows at high Reynolds numbers can be simulated using hybrid models that resolve various scales of detached eddies, while wall-bounded flow eddies are modeled by a RANS model. Examples of these are the detached eddy simulation (DES) approach developed by Spalart et al. in [29], where the wall-bounded RANS mode is switched to a LES mode in detached regions, or the SAS model of Menter et al. used in [22], [20], [21]. The DES approach however requires exact grid information, a detailed understanding and a high accuracy of grid generation which is difficult to achieve. Large eddy simulation (LES), a more sophisticated turbulence model that can resolve at least the large vortex structures, is computationally very expensive for high Reynolds number flows encountered in industrial applications and is not practicable.

### 3.7 Numerical Modeling

Numerical methods yield discrete numerical solutions of the governing equations describing these flow physics, and solving for such fields as  $U, V, W, p, T$ , etc. CFD provides the practical analysis of systems involving fluid flow, heat transfer, and associated phenomena such as chemical reactions by means of computer-based simulation. It can produce extremely large volumes of results at virtually no added cost, and parametric studies can be performed at lower cost in less time. It has the ability to study systems where controlled experiments are difficult or impossible to perform, or under hazardous conditions [40].

The results of numerical studies are generally compared with test data from experiment comprehensive measurements, using different types of measuring systems under different conditions. Our numerical method is validated using the test rig experimental data from the Hannover Leibniz University described in [27], using the test rig configuration without spoke-wheel and no swirl at the annular diffuser inlet.

The numerical solution process to solve the Partial Differential Equations (PDE's) governing a flow problem involves the following steps:

- The generation of a computational grid,
- The discretization of the governing equations on the computational grid to produce a set of discretized algebraic equations, and
- The solution of the algebraic equations.

### 3.7.1 Mesh Generation

In this first step, the solution domain is divided into a number of discrete cells known as control volumes. The control volumes geometric centers also known as cell centers, are considered as nodal points where all dependent variables and material properties are stored. The practice is called a co-located cell-centered variable arrangement where average values of quantities within a control volume are given at the cell center [10]. The control volume boundaries or faces are positioned mid-way between adjacent cell centers. It is common practice to set up control volumes near the edge of the domain such that the physical boundaries coincide with the control volume boundaries [40]. In diffuser CFD calculations, special importance is given to the generation of the computational grid which must be capable of predicting the flow behavior near the walls using an optimum number of grid nodes in the boundary regions. The grid must feature very fine meshes in regions where large gradients of the flow properties normal to the flow direction could exist [17]. For a better mesh design capable of capturing all the real flow features, it is necessary to have an idea of how the flow pattern will look like. This information can be provided by existing experimental data or the theory of the physics involved in the problem. For the current investigations, an experimental velocity profile at 50% annular diffuser provided some guidelines in designing the mesh. From analyzing the experimental data on figure 11, it was found four flow regions dominated by an adverse pressure gradient, i.e. two viscous boundary layers near the wall with high velocity gradients, a nearly inviscid core flow region where the velocity profile remained almost constant, and a

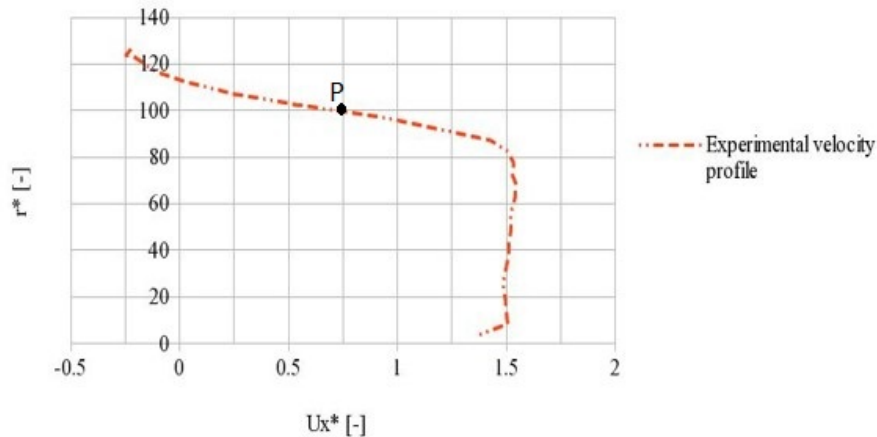


Figure 11: Physical insights: Main characteristics of diffuser high  $Re$  flows [27]

separated backflow region with high mixing. The shroud boundary layer was separated from the casing wall and the high gradient velocity profile changed concavity at a point of inflection, P, located within the boundary layer. High shear stress exit in the boundary layers and the backflow regions requiring high mesh resolution.

### 3.7.2 Discretization

OpenFOAM uses the standard Gaussian finite-volume (or control-volume CV) discretization practice. In this approach, the governing transport equations of fluid flow, for a property  $\phi$ , are numerically integrated over each of the computational cells or finite three-dimensional control volumes of the computation domain before the discretization of the governing equations. The Gauss's divergence theorem is then employed to replace volume integral involving divergences, i.e. the convective and the diffusive terms, with integrals over the entire bounding surface of the control volume to obtain the integral form of the general transport equations. The control volume integration is the key step of the finite volume method distinguishing it from

all other CFD techniques [40]. The finite volume method is more attractive due to its capability to conserve solution quantities for each finite size cell.

The generalized transport equation for a quantity  $\phi$ , representing most of the governing equations has the following form:

$$\frac{\partial(\rho\phi)}{\partial t} + \vec{\nabla} \cdot (\rho\vec{V}\phi) = \vec{\nabla} \cdot (\Gamma\vec{\nabla}\phi) + S_\phi, \quad (65)$$

The integration of this generic conservation equation over a control-volume cell leads to:

$$\int_{CV} \frac{\partial(\rho\phi)}{\partial t} dV + \int_{CV} \vec{\nabla} \cdot (\rho\vec{V}\phi) dV = \int_{CV} \vec{\nabla} \cdot (\Gamma\vec{\nabla}\phi) dV + \int_{CV} S_\phi dV, \quad (66)$$

The first term on the left-hand-side (LHS) of equation (66), which is a transient term, can be discretized as:

$$\int_{CV} \frac{\partial(\rho\phi)}{\partial t} dV = \frac{\rho\phi V_{CV} - \rho^0\phi^0 V_{CV}^0}{\Delta t}, \quad (67)$$

where the superscript 0 denotes the initial time, and the absence of superscript represents the current time. The discretization of the convection term, the LHS second term, is as follows:

$$\int_{CV} \vec{\nabla} \cdot (\rho\vec{V}\phi) dV = \int_A \rho\phi\vec{V} \cdot \vec{n} dA = \sum_i (\rho_i\phi_i(V_n)_i)A_i = \sum_i C_i\phi_i, \quad (68)$$

where the subscript  $i$  represents one of the cell faces, and  $A_i$  its area.  $V_n$  denotes the velocity component in the direction normal to the face, and  $C_i$  represents the mass flux across the face  $i$ . Due to the fact that the solution variable  $\phi$  is available only at cell centers, its cell-face values need to be interpolated. In the evaluation of

the  $\phi$  value at any face  $i$  of a control volume, there exist various interpolation schemes with varying levels of numerical accuracy and stability. Some popular ones are [10]:

- The first-order upwind scheme
- The central difference scheme
- The second-order upwind scheme
- The second-order upwind with limiter
- The smart scheme
- The third-order scheme.
- The upwind differencing scheme,
- The hybrid differencing scheme of Spalding (1972), based on a combination of the first two schemes,
- The power-law scheme of Patankar (1980),
- Higher-order differencing schemes for convection-diffusion problems such as the Quadratic upwind or upstream interpolation for convective kinetics (QUICK) scheme of Leonard (1979). These schemes involve more neighbor points and reduce the discretization errors by bringing in a wider influence,
- The total variation diminishing (TVD) schemes, formulated to achieve oscillation-free solutions, and a linear upwind differencing (LUD) scheme involving two upstream values.

The first term in the right-hand-side (RHS) is the diffusion term discretized as follows:

$$\int_{CV} \vec{\nabla} \cdot (\Gamma \vec{\nabla} \phi) dV = \int_A \Gamma \vec{\nabla} \phi \cdot \vec{n} dA = \sum_i \Gamma_i \left( \frac{\partial \phi}{\partial n} \right)_i A_i \quad (69)$$

To obtain useful forms of the discretized equations for a diffusion problem for example, the interface diffusion coefficient,  $\Gamma$ , and the gradient of the transported property in a certain direction  $x_i$ ,  $\frac{d\phi}{dx_i}$ , must be specified. It is common practice to define and evaluate the values of the property  $\phi$  and the diffusion coefficient at nodal points. Thus to calculate gradients and fluxes at the control volume faces, an approximate distribution of properties between nodal points is used. The linear approximations seem to be the obvious and simplest way of calculating interface values and the gradients. This approach is called central differencing scheme and linearly interpolated values for the diffusion coefficient on each face can be obtained in a uniform grid as[40]:

$$\Gamma_{face1} = \frac{\Gamma_{P-1} + \Gamma_P}{2} \quad (70)$$

$$\Gamma_{face2} = \frac{\Gamma_P + \Gamma_{P+1}}{2} \quad (71)$$

If the source term is a function of the dependent variable  $\phi$ , it can also be approximated by means of a linear form as:

$$S_\phi = S_u + S_p\phi_p, \quad (72)$$

where  $S_p$  is negative and both  $S_p$ ,  $S_u$  can, in general, be positive. They are evaluated using the latest available value of  $\phi$  generally from the previous iteration. The integrated linearized source term over the control volume is given by:

$$\int_{CV} S_\phi dV = S_U + S_P\phi_P, \quad (73)$$

with  $S_P = S_p\phi$  and  $S_U = S_u\phi$ . All the discretized terms are substituted into the

Table 1: The main keywords in fvSchemes.

<b>Keyword</b>	<b>Category of mathematical terms</b>
interpolationSchemes	Point-to-point interpolations of values
snGradSchemes	Component of gradient normal to a cell face
gradSchemes	Gradient $\nabla$
divSchemes	Divergence $\nabla \cdot$
laplacianSchemes	Laplacian $\nabla^2$
timeSchemes	First and second time derivatives $\partial/\partial t, \partial^2/\partial^2 t$
fluxRequired	Fields which require the generation of a flux

Gaussian integral form of the general transport equations to obtain the discretized forms. Additional source terms can be added to the conservation equations to model external sources or sinks for various dependent variables; a mass source or sink is an extra source term in the pressure correction equation, a heat source or sink can be added to the enthalpy equation, and an additional force can also be added to the momentum equation. There may exist complex sources that are usually dependent on other variables. OpenFOAM cases have a basic directory structure, containing the minimum set of files required to run an application. The interested reader should consult the OpenFOAM user manual for more information.

Numerical schemes for terms that appear in the application being run, such as derivatives, e.g. gradient  $\nabla$ , contained in the governing transport equations can be set through a specific dictionary. These terms, along with interpolations of values from one set of points to another, must be assigned a numerical scheme. This is the case for the linear interpolation, which is effective in many cases, and supplemented in OpenFOAM with a wide range of interpolation schemes for all interpolation terms. For the derivative terms, certain schemes are specifically designed for particular terms such as the convection divergence,  $\nabla \cdot$ , terms. Table 3 gives the OpenFOAM categories for the set of terms for which numerical schemes must be specified.

### 3.7.3 Solution of Discretized Equations

The discretized equations must then be set up at each of the nodal point to solve the problem. For the control volumes adjacent to the domain boundaries, the general discretized equation is modified to incorporate boundary conditions. A system of linear algebraic equations will then result, and be solved to obtain the distribution of the transported property at nodal points. For this purpose, any suitable matrix solution technique may be used and some matrix solution methods especially designed for CFD procedures exist to control the problem solution.

OpenFOAM uses an iterative, segregated solution method in which the equation sets for each variable are solved sequentially and repeatedly until a converged solution is reached. The linear discretized equations solvers, tolerances, and algorithms are controlled from another dictionary containing a set of subdictionaries specific to the application solver being run. At this point, it is important to distinguish between the linear solver and the application solver; the term linear solver refers to the method of number-crunching to solve the set of linear equations, as opposed to application solver, such as icoFoam, pisoFoam, simpleFoam that describe the set of equations and algorithms to solve a particular problem. The application solver icoFoam, for example, is a transient solver that can be used for laminar, isothermal, and incompressible flow of Newtonian fluids, whereas pisoFoam is a transient solver used for turbulent, isothermal, and incompressible flow. As for simpleFoam, it is a steady-state solver for incompressible, turbulent flow and all are considered standard solvers.

Table 2: An overview of the linear solvers used in OpenFOAM.

<b>Solver</b>	<b>Keyword</b>
Preconditioned (bi-)conjugate gradient Solver using a smoother	PCG for symmetric matrices/PBiCG for asymmetric matrices smoothSolver
Generalized geometric-algebraic multi-grid	GAMG
Diagonal solver for explicit systems	diagonal

### 3.7.3.1 Solvers

Table 2 gives the types of linear solvers available in OpenFOAM. The tolerances must be specified for all solvers, with the former representing the level at which the residuals are small enough to consider the solution sufficiently accurate. The latter limits the relative improvement from initial to final solution, since the sparse matrix solvers are iterative, i.e. they are based on reducing the equation residual over a succession of solutions. The residual is a measure of the error in the solution, and the smaller it is, the more accurate the solution. After each solver iteration, the residual is evaluated and the solver stops if either of the following conditions are reached:

- The residual falls below the solver tolerance;
- The ratio of current to initial residuals falls below the solver relative tolerance;
- The number of iterations exceeds a maximum number of iterations. The specification of the latter is optional

It is preferable to obtain a five order of magnitude reduction in the residual before declaring that the convergence has been achieved.

One of the objectives of the present work being to evaluate the reliability of the OpenFOAM Navier-Stokes codes. OpenFOAM is a  $C_{++}$  library used primarily to create executables, i.e. applications that are categorized either as solvers or utilities. The solvers are designed to solve specific problem in continuum mechanics and the

utilities are designed to perform tasks involving data manipulations and OpenFOAM comes with pre- and post-processing environments.

### 3.7.3.2 Relaxation parameter subdictionary

The convergence rate of the Jacobi and Gauss-Seidel point-iterative methods depends on the properties of the iteration matrix. These properties can be improved by introducing a relaxation parameter,  $\alpha$ , for which different values will yield different iterative sequences. If we consider  $0 < \alpha < 1$ , the procedure is an under-relaxation method; for  $\alpha > 1$  it is called over-relaxation. The relaxation parameter changes the iteration path without changing the final solution. The relaxation may be advantageous if an optimum value of  $\alpha$ , that minimizes the number of iterations required to reach converged solution, is selected. However, the optimum value of the relaxation parameter is problem and mesh dependent so that it is difficult to give precise guidance [40]. Fortunately, through experience with a particular range of similar problems, it is possible, in principle, to select a value of  $\alpha$  giving a better convergence rate. OpenFOAM uses this technique for improving stability of a computation, particularly in solving steady-state problems through the `relaxationFactors` subdictionary which controls under-relaxation. Under relaxation of dependent variables, and auxiliary variables such as  $\rho$ ,  $p$ ,  $T$ , and  $\mu$ , is used to constrain the change in the variable from iteration to iteration to prevent the divergence of the solution procedure. An under-relaxation factor,  $0 < \alpha \leq 1$  specifies the amount of under-relaxation from  $\alpha = 1$  for zero under-relaxation to  $\alpha = 0$ , representing a solution which does not change at all with successive iterations. An optimum choice is one that is small

enough to ensure stable computation, but large enough to move the iterative process forward quickly. Values of  $\alpha$  from 0.2 to 0.8 are common. Values as high as 0.9 can ensure stability in some cases and anything much below, for example 0.2, are highly restrictive in slowing the iteration process [18]. In very difficult problems, it may be necessary to use values of  $\alpha$  greater than 1. The process of searching for an optimum relaxation value may be considered as an optimization problem to get a better behavior.

### 3.7.3.3 PISO and SIMPLE algorithms

The iterative procedures for solving equations for velocity and pressure, i.e. pressure-implicit split-operator, PISO, or semi-implicit method for pressure-linked equations, SIMPLE algorithms, are used in most fluid dynamics solver applications in OpenFOAM. PISO is used for transient problems, and SIMPLE for steady-state ones. These algorithms evaluate some initial solutions and then correct them, with SIMPLE making only one correction and PISO making at most four corrections. In fact, for a given solver, the source code contains required parameters that may be needed to control the solver, algorithms, or anything else.

## CHAPTER 4: METHODOLOGY

Chapter four gives the basic procedures used to gain insights into the world of internal flow predictions through the CFD analysis tool, using the OpenFOAM solver, version 2.0.1. The Moody chart, which is a great correlation for tubes of different characteristics used to determine the flow properties, is only reliable for ducts of constant cross section. In the case of tapered duct diameter such as a diffuser, which is a thermal device with a variable cross section, experimentation and numerical methods, i.e. either boundary-layer theory or, now computational fluid dynamics, CFD, are vital parts of fluid mechanics and appropriate to determine flow properties [42]. In this chapter we shall describe the solution methodology adopted in our research to allow comparison of CFD predicted results with experimental data, as well as the problem setup. After conducting the literature review and defining the research problem, a workflow procedure has been devised as follows.

### 4.1 Research Workflow Procedure

In order to efficiently define and solve the research problem involving different physical principles and processes, the use of a systematic approach has been deemed important to guide our thinking. This workflow procedure is characterized by specific steps and was developed as described below:

1. Initial CFD analysis and CFD approach validation
2. Additional simulations varying selected inflow characteristics

3. Data collection, results analysis and interpretation, and summary of key findings.

## 4.2 Simulation Implementation

This section describes how a model for the simulation of a typical gas turbine exhaust diffuser flow was setup, solved, and post-processed using OpenFOAM 2.0.1. The selected approach consisted of carrying out 3-D steady-state CFD simulations using Reynolds Averaged Navier-Stokes (RANS) method. After an initial CFD study used to validate the CFD approach and address the management of any potential issues, we proceeded to analyze the effects of some inflow properties on the flow characteristics. For this purpose, the effects of selected turbulence models have been first investigated and the results compared to experimental data to establish the veracity of those models. Using the most robust turbulence model, we went on to investigate the effects of other inlet parameters as the turbulence intensity, temperature, flow angle, and mesh cell count. Ultimately, data collection and analysis have been performed, mainly using OpenFOAM utilities. Any CFD simulations require data for geometry, mesh, fields, properties, processes, control parameters, etc. In OpenFOAM, these data are stored in a set of files within three subdirectories of the case directory, contrary to other CFD packages which store data in a single case file. Three major steps are involved to perform a CFD simulation, i.e. the pre-processing, the analysis or solution, and the post-processing phases. Figure 12 gives an OpenFOAM overview of the CFD simulation process.

### 4.2.1 Pre-processing

The pre-processing phase itself may be divided into three subphases:

- The geometry modeling,
- The mesh generation, and
- The model setup.

#### 4.2.1.1 Geometry Modeling

The definition of the computational domain has been done based on Olaf Sieker et al. experiments [27], by considering the case without a spoke-wheel. The computer-aided design (CAD) model was drawn using the SolidWorks modeling software, for which the geometry is shown in figure 13 and the dimensions in 14. The model consists of one inlet section, one outlet section, and two walls consisting of the diffuser casing and hub. The computation domain has a length of about 1.9 m.

#### 4.2.1.2 Mesh Generation

The availability of a suitable grid is one of the most important requirement before a CFD computation can be performed because the grid extends the geometry information to the flow solver. Inability to construct a grid quickly and reliably often rules

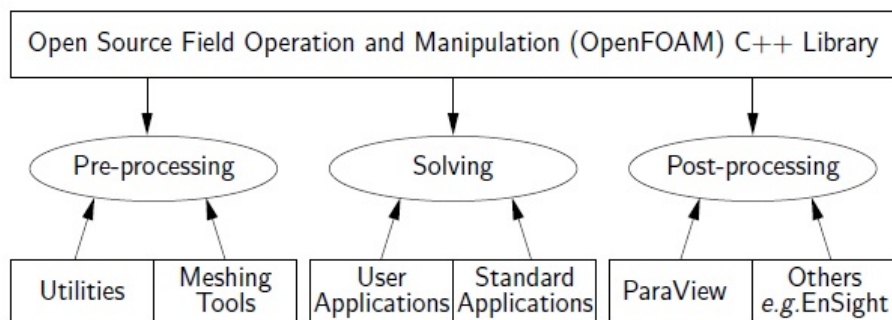


Figure 12: Overview of OpenFOAM structure

out a CFD analysis. Improper grid can affect the physics of the simulated flow, the stability of the computation, and the computation time. Our objective here was to mesh the gas turbine exhaust diffuser internal flow field region, i.e. for an internal aerodynamics simulation. We shall describe the mesh generation process and follow general gridding guidelines and best practices. Since the mesh is an integral part of the numerical solution, the CFD analyst must make sure that it is valid, to prevent the solution to be flawed or compromised before the analysis has even begun. After drawing the CAD geometry, the grid generation process started with the geometry surface meshing using ANSA, a surface meshing tool that produced a stereolithography file format (.stl). The .stl file has then been exported to the OpenFOAM. The generation of the solution-domain volume meshing has been done in two steps using OpenFOAM volume meshing utilities supplied with OpenFOAM.

First the *blockMesh* utility for generating simple meshes of blocks of purely hexahedral cells has been used to generate an initial or background mesh. Finding the appropriate base mesh size was very crucial to the convergence of the solution. The

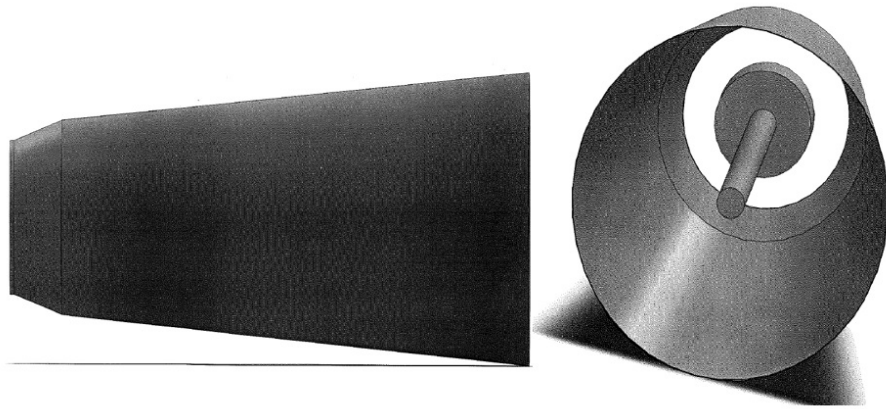


Figure 13: Analyzed gas turbine typical exhaust diffuser geometry

base mesh was generated from a description specified in an input dictionary, which also contains the extent of the computational domain as well as a base level mesh density. In creating the background mesh, there must be at least one intersection of a cell with the STL surface, consequently, a mesh of one cell will not work. Furthermore, the cell aspect ratio must be approximately 1 for a high convergence of the snapping procedure [18]. In using the standard  $k - \epsilon$  turbulence model, the  $20 \times 11 \times 11$  base mesh was used, with a cell count of 2420 cells. The SST  $k - \omega$  turbulence model, however, used a  $40 \times 22 \times 22$  base mesh with a cell count of 19360 cells.

The *snappyHexMesh* utility has then been used to generate 3-dimensional complex meshes containing hexahedra (hex) and split-hexahedra (split-hex) cells, automatically from triangulated surface geometry in STL format.

In OpenFOAM, the geometry can also be supplied through a bounding geometry entities. The *snappyHexMeshDict* dictionary has switches at the top level to control the various stages of the meshing process, with individual sub-dictionaries for each stage. During this process, the mesh approximately conforms to the surface by iteratively refining the starting mesh and morphing the resulting split-hex mesh to the surface. An additional phase shrinks back the resulting mesh before inserting cell

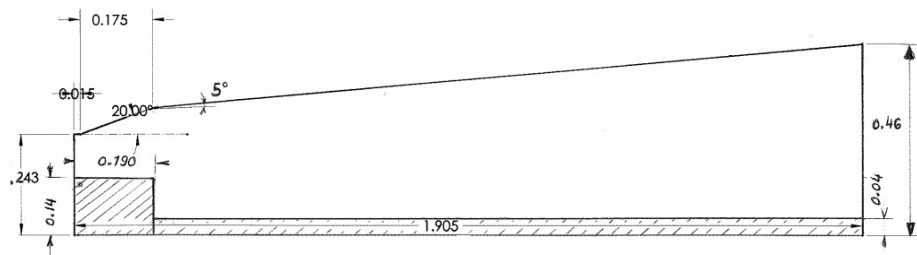


Figure 14: Analyzed GT exhaust diffuser dimensions

layers. The specification of mesh refinement level is very flexible and the surface handling is robust with a pre-specified final mesh quality [18]. The following individual processes are performed when generating the 3-D mesh using *snappyHexMesh*:

- Cell splitting at feature edges and surfaces,
- Cell removal,
- Cell splitting in specified regions
- Snapping to surfaces
- Mesh layers, and
- Mesh quality controls

The cell removal process allows to keep cells only in the solution domain, and the snapping process moves the cell vertex points onto the surface geometry to remove the jagged castellated surface from the mesh. In OpenFOAM, the addition of layers of hexahedral cells aligned to the boundary surface corrects some irregularities of cells along the boundary surfaces, and allows to resolve the near-wall boundary region. Cells are refined smoothly towards the hub and casing walls to achieve the correct values of the dimensionless wall distance for using standard  $k - \epsilon$  as well as the SST  $k - \omega$  turbulence models with wall functions. The resulting mesh, with about 47 million cells, used with the SST  $k - \omega$  turbulence model is shown in figure 15 with figure 16 showing its close up mesh in the annular portion of the diffuser.

Four elements are taken into account in the boundary layer generation, i.e., the boundary layer thickness, the growth factor, the number of cell layers, and the height of the first node. In OpenFOAM, the boundary layer thickness and the height of the

first node are computed based on the two other fixed elements and the size of the last cell layer in the boundary layer. The latter is determined as a fraction of the highest refinement level of the core region of the computational domain. Considerable amount of time was spent to try to generate thicker boundary layers at the hub and the casing. Therefore, we varied a certain number of parameters, mainly the boundary layer growth factor or expansion ratio, the size of the last cell layer in the boundary layer, and the number of cell layers, while keeping default values of all other parameters. The boundary layer mesh expansion ratio giving reasonable results was varied from 1.09 to 1.15, with 1.09 used for the best case using the standard  $k - \epsilon$  turbulence model and 1.14 for the SST  $k - \omega$  turbulence model. The wanted thickness of the last added cell layer was varied from 0.2 to 0.3 the size of the cell just outside the boundary layer mesh; with 0.3 used with the  $k - \epsilon$  turbulence model and 0.25 for the SST  $k - \omega$  turbulence model. As for the number of added boundary cell layers, it was varied between 10 to 18, with any values above 25 resulting in a sensible reduction in the overall cell count. OpenFOAM computed the near-wall cell layer thickness around 0.2 mm for the standard  $k - \epsilon$  turbulence model, giving an average boundary layer thickness of about 5 mm. The SST  $k - \omega$  turbulence model near-wall cell layer thickness was much lower, about 0.04 mm and a boundary layer thickness of about 2.4 mm. Since the flow in this exhaust diffuser is characterized by an increasing adverse pressure gradient, much greater number of cell layers in the boundary layer than used here is necessary to produce a much thicker boundary layer capable of capturing the boundary region flow. The generated boundary layers are illustrated in figures 17 and 18. Besides the refinement towards the wall regions, additional refinement through

defined boxes within the exhaust diffuser was done to ensure an accurate numerical solution. The region-wise refinement level varied from 0, which is the base mesh, to a refinement level value of 6 for most cases.

The numerical solution depending on the mesh, the latter must satisfy certain criteria ensuring a valid, and hence accurate, solution. To ensure that the solution is not flawed before the run has even begun, OpenFOAM adopts good practice of checking that the mesh satisfies a fairly stringent set of validity constraints and OpenFOAM will simply stop if these constraints are not satisfied. A small number of illegal faces may not prevent the solver from running successfully, however, this number increases the solution may diverge. The resulting cell count varied from six millions to seventeen millions when using the standard  $k-\epsilon$  turbulence model, and forty-seven millions for the SST  $k-\omega$  turbulence model. As for the time it took to generate the mesh, it varied from 2 to about 10 hours depending on the density of the mesh to be created.

By default OpenFOAM defines a mesh with a general structure representing the OpenFOAM mesh format known as *polyMesh*, made of arbitrary polyhedral cells in 3-D and bounded by arbitrary polygonal faces. Therefore these cells can have an unlimited number of faces having no limit on the number of edges nor any restriction on the alignment of each face. This type of mesh offers great freedom in mesh generation and manipulation especially with complex domain geometries or when the domain geometry changes over time. This mesh generality coupled with the OpenFOAM mesh validity checks make it difficult to convert meshes generated using conventional third-party meshing tools; and the user may experience some frustration in correcting a large mesh [18].

#### 4.2.1.3 Model Setup

It is important to select the engineering models, i.e. the assumptions or conditions under which the solution results will be valid before proceeding any further, and all of the model's physical and numerical settings shall be described in the remainder of this chapter. Another set of user activities at the pre-processing stage, that consisted of the input of the flow problem parameters to the OpenFOAM CFD program, involved:

- The selection of modeled physical and chemical phenomena,
- The definition of fluid properties, and
- The specifications of appropriate boundary and initial conditions.

The selected physical models consisted of steady-state isothermal, incompressible, turbulent, and 3-dimensional viscous flow inside the gas turbine annular-conical exhaust diffuser. The studied system material considered was air at standards conditions, i.e. 15 degrees Celcius and atmospheric pressure of  $1.01325 \times 10^5$  Pa. As for each control volume condition, structured or unstructured, the only physical material property to be specified in OpenFOAM was the air kinematic viscosity,  $\nu = 1.486 \times 10^{-5}$  m<sup>2</sup>/s stored in the *transportProperties* dictionary in the constant directory.

After generating the mesh, the initial fields for solved variables requiring initialization and for every cell in the computational domain, as well as the computational boundary conditions for each boundary condition patch needed to be set. Three types of boundaries were applied for our three-dimensional computation model, i.e. inflow, outflow, and solid walls (no flow). The following turbulent flow problem settings were specified at the inlet computational cells: The average velocity from the fixed

mass flow rate, the kinematic inlet and outlet pressures obtained from detailed measurements. The turbulent kinetic energy,  $k$ , and the turbulence dissipation rate,  $\epsilon$ , were calculated using generally known correlations. For the outflow boundary, except for the pressure, we used zero axial gradient for the other dependent variables, and OpenFOAM wall functions were used for all dependent variables on all internal walls.

The initial values and boundary conditions of each field must be set, and for all simulations, the initial fields are set to be uniform. The kinematic pressure,  $p/\rho$ , is used in our simulations, and the initial inlet and outlet pressures were determined from measurements, using the measured pressure recovery coefficient. As for the boundary field for velocity, the inlet velocity of 41.16 m/s in the flow direction was determined using the experiment mass flow rate of 6 kg/s, the inlet cross-section area, and the density of the air considered at standard conditions. Based on the continuity principle, the mass flow rate was kept constant throughout the diffuser. The internal velocity field was initialized as uniform zero. At the walls, a no-slip condition is assumed. The flow Reynolds number from the specified properties is thus given by  $Re = 2h \times U_x/\nu = 542,891$ , where  $h = 0.098$  m is the annular diffuser inlet height and  $2h$  is the inlet hydraulic diameter,  $U_x = 41.16$  m/s.

For the purpose of applying boundary conditions, a domain boundary is generally divided into a set of patches, each one associated with a boundary condition [18]. The patches can be characterized as of base type, which are described purely in terms of geometry or a data communication link. They are specified in OpenFOAM in the boundary file as `patch` or `wall`, `symmetryPlane`, `empty`, `wedge`, `cyclic`, `processor`. *Patch* is the basic patch type for a patch condition containing no geometrical or

topological information about the mesh, and examples include an inlet or an outlet. The wall base type name is used for wall functions in turbulent flows, and the processor name for inter-processor boundary when a code is being run in parallel on a number of processors. The mesh has been divided up to allow each processor to compute on roughly the same number of cells. The patches can also be characterized as of numerical type, i.e. primitive type, or derived type, and specified in OpenFOAM under the type keyword for each patch in a field file such as of pressure or velocity. Examples of the primitive patch fields type names include *fixedValue*, where the value of the variable is specified, *zeroGradient*, with the normal gradient of the variable considered as zero, and no data is specified in this case, or the *fixedGradient* where the normal gradient of the variable is specified. Example of the derived patch field types are the *totalPressure*, where the total pressure is fixed and p is adjusted when the velocity changes. We also have the *inletOutlet* type, which switches the velocity and the pressure between *fixedValue* and *zeroGradient* depending on the direction of the velocity.

For turbulent flows, mesh grading in the wall region is irrelevant when using the standard  $k - \epsilon$  turbulence model with wall functions. An adequate turbulence model will provide an accurate prediction. Therefore, to evaluate some turbulence models, we used those with near-wall resolution and with the less accurate wall functions. The flow in the near-wall cell is modeled instead of being resolved. The wall functions models are applied as boundary conditions on individual patches in different wall regions. These wall functions models were specified through the turbulent viscosity or kinematic eddy viscosity field. In OpenFOAM, in order to avoid the huge cost

of directly solving the turbulent behavior, the Reynolds-averaged simulation (RAS) turbulence models, which is OpenFOAM nomenclature of RANS approach, are used to solve for the mean flow behavior and also calculate the fluctuations statistics. The RAS turbulence modeling method provided in OpenFOAM is set through the *simulationType* keyword in the *turbulenceProperties* dictionary. For the steady-state cases, the additional equations and models for turbulent flows are implemented into a OpenFOAM solver called *simpleFoam*. The two extra variables or turbulence quantities to solve for, for which the initial and boundary conditions must be approximated and specified, are  $k$  and  $\epsilon$  or  $\omega$ , respectively the turbulent kinetic energy, the turbulent dissipation rate, and the turbulence frequency. The turbulent viscosity  $\nu$  and the turbulence dissipation rate  $\epsilon$  can be used to calculate Reynolds stresses. In addition  $k$  and  $\epsilon$  correspond to a turbulent intensity  $I$  and a turbulence length scale,  $l$ . Gas turbine diffuser inlet turbulence intensity is not generally measured during in test engines and is usually unknown when designing these devices. However, Feldcamp et al. in [6] state that the turbulence intensity is usually in the range of 5-10% depending upon the location of the device relative to the turbine exit. The initial values for  $k$  and  $\epsilon$  were set using the calculated Reynolds number, and calculated turbulence intensity  $I = 0.16(Re)^{-1/8} = 0.03$ , assuming the inlet turbulence to be isotropic. Therefore, the turbulence fluctuations were estimated to be 3% of the inlet velocity, i.e. about 1.23 m/s. The turbulence length has been estimated as  $l = 0.07L$ , where  $L = 2h$  is the characteristic length, here the annular diffuser hydraulic diameter, with  $h$  the annular diffuser inlet height. The turbulent kinetic energy and the turbulence dissipation rate were then calculated as:

Table 3: Summary of  $k - \epsilon$  baseline boundary conditions.

Boundary	$U_x \text{ ms}^{-1}$	$p \text{ m}^2\text{s}^{-2}$	TKE ( $k$ ) $\text{m}^2\text{s}^{-2}$	Dissipation ( $\epsilon$ ) $\text{m}^2\text{s}^{-3}$
Inlet	41.16	1.51	2.4	44.59
Outlet	Zero-gradient	377.1	Zero-gradient	Zero-gradient
Walls	No-slip	Zero-gradient	2.4 with Wall-function	44.59 with Wall-function

$$k = \frac{3}{2}(U_{avg}I)^2 \quad (74)$$

$$\epsilon = \frac{C_\mu^{0.75}k^{1.5}}{l}, \quad (75)$$

where  $C_\mu = 0.09$ , a constant of the  $k - \epsilon$  model. Substituting all the above values gives  $k = 2.4 \text{ m}^2\text{s}^{-2}$ , and  $\epsilon = 44.59 \text{ m}^2\text{s}^{-3}$ .

For isothermal cases with higher temperatures, as in real gas turbine exhaust diffusers, the following parameters needed to be changed to obtain more realistic predictions:

- The density, which in turn affect
- The velocity, thus changing the Reynolds and Mach numbers, and
- The turbulence parameters, i.e.  $k$ ,  $\epsilon$ , and  $\omega$ , which depend upon the Reynolds number of the flow.

#### 4.2.2 Analysis or Solution

The exhaust diffuser needs to be treated as a component of the whole system, not an isolated element, since a high level of turbulence with increased turbulent mixing and a swirl component exist at its inlet and need to be taken into account in the exhaust diffuser analysis. These result in a later flow separation that can improve its performance. The wakes behind the turbine distort the total pressure and produce

yaw and pitch angles that are significant.

A numerical method to solve the Partial Differential Equations (PDE's) or, in the control volume approach, the resulting integral equations governing a fluid-flow problem physics involves a numerical solution process consisting of:

- The discretization of the governing equations on a computational grid leading to a set or system of algebraic equations, and
- Their solution by an iterative method using a specific solver.

Before running the model solver, the numerical aspects of the solution and the solver output options, yielding discrete solutions for the fields at the cell centers, need to be specified in order to control the solvers, the tolerances or convergence criteria, and algorithms. The solution of the turbulent flow inside the exhaust diffuser is done by running the OpenFOAM *simpleFoam* application solver. This application solver describes the set of equations and algorithms designed to solve a steady-state, turbulent, isothermal, and incompressible flow. Most of the converged solutions ran for a number of iterations less than 2500, and in general around 1000 iterations, with the number of iterations being dictated by the overall residual reduction desired .

OpenFOAM uses the standard Gaussian finite volume integration for the discretization of the governing equations. The Gaussian integration is based on summing values on cell faces, which must be interpolated from cell centers. For the evaluation of a problem variable at the control volume faces, the spatial differencing schemes to control the spatial accuracy and the stability of the simulation, the *linear* interpolation for the central differencing scheme has been used for gradient (pressure source) terms, the *linear* interpolation and the *corrected* surface normal gradient scheme evaluated

at a cell face to evaluate the Laplacian (diffusion) terms, and the *upwind* interpolation for the upwind differencing scheme for the divergence (convection) terms in fluid flow. OpenFOAM has three generally recommended categories of interpolation schemes that can be used primarily in conjunction with the Gaussian discretization of convection (divergence) terms, i.e. upwinded, TVD, and NVD schemes. The first-order accuracy upwind scheme is one of the most stable schemes. The centered schemes such as the conventional and most used linear and second-order accurate central difference interpolation scheme, the cubic scheme, and the linear interpolation scheme with symmetry weighting constitute the only category for general field interpolation schemes used for other terms in the transport equation. The common choice *Gauss* keyword specified the standard finite volume discretization of Gaussian integration which requires the interpolation of values from cell centers to face centers. The first time derivative terms were specified in the *ddtSchemes* as *steadyState* since we are not solving for time derivatives.

The conjugate gradient types solvers, having many advantages over classic iterative methods, i.e. the suitability for vectorization and the lack of user-specified parameters [10], so that their algorithms have been incorporated in the OpenFOAM program. For the solution of the set of algebraic equations, the *Preconditioned Conjugate Gradient* (PCG) linear-equation solver has been used throughout the numerical investigations to solve for pressure, and the *Preconditioned bi-Conjugate Gradient* (PBiCG) solver to solve for the other dependent variables, i.e.  $U$ ,  $k$ ,  $\epsilon$ ,  $\omega$ ,  $R$ . The linear solver describes the method of number-crunching to solve the set of linear equations and their convergence rate has been accelerated by preconditioning the system with a precondi-

tioning matrix which approximates the linear equation system matrix. The tolerances or convergence criteria, the solver controlling parameters that control the amount of residual drop required for the linear solver to terminate were set to  $10^{-6}$  for pressure and  $10^{-5}$  for other dependent variables since it is desirable to see five order of magnitude reductions in the residuals before declaring that convergence has been achieved [10]. Since no governing PDE for pressure is present, the SIMPLE scheme, which is a pressure-based method utilizing the continuity equation to formulate an equation for pressure, has been used. The under relaxation factors, constraints on the change of a dependent variable from one solution iteration to the next, required to maintain the stability of the coupled, non-linear system of equations were set to 0.3 for pressure and 0.7 for the other dependent variables, preventing the divergence of the solution procedure. The progress of the job was monitored from the terminal window, where the current time and the initial and final residuals for all fields were displayed.

During our numerical simulations, our main focus was to try to correctly predict the separation point at the diffuser casing as predicted by the experiment, at the radius of about 0.255 m where the axial velocity becomes zero. Our best case CFD prediction using the SST  $k - \omega$  turbulence model gave a velocity value of about 4.1 m/s.

#### 4.2.3 Post-processing

The simulation results were written into time directories in the case directory. They were viewed using an OpenFOAM utility called *paraFoam*, the main post-processing tool and a reader module to run with *ParaView*, after loading the data of interest at

the required run time, typically the simulation end time. *ParaView* is an open-source and multi-platform data analysis and visualization application. *ParaView* uses the *Visualisation ToolKit* (VTK) as its data processing and rendering engine, and can therefore read any data in VTK format [18]. This post-processing tool allowed to display scalar, vector, and streamline plots. Flow visualizations, experimentally or numerically, enable to gain a qualitative understanding of the flow patterns.

To visualize the results as two-dimensional graphs along lines through the solution domain by extracting some scalar measure of velocity and pressure, we used two OpenFOAM utilities, i.e. *foamCalc* and *sample* utilities. These types of utilities perform specialized data manipulations and some simpler calculations. When *foamCalc components U* is performed, it reads in the velocity vector field from each time directory and writes scalar fields  $U_x$ ,  $U_y$ , and  $U_z$  of the three velocity components, and these can then be plotted as graphs in *ParaView*. The OpenFOAM *sample* utility allows the sampling of field data, either through a one-dimensional line for plotting line graphs, or a two-dimensional plane for displaying isosurface images. The sampling locations are specified in the *sampleDict* dictionary in the case[18] directory. Once a sample of field data such as that of velocity, pressure, or turbulent kinetic energy was obtained, it was exported to a spreadsheet software to produce graphs. In our case, we mainly used libreOffice 4.1 Calc spreadsheet.

For the purpose of validating the numerical results, the experimental graphs have been digitized using a tool called *Plot Digitizer* version 2.5.0. This is a Java program used to digitize scanned plots of functional data, i.e. X-Y type scatter or line plots in GIF, JPEG, or PNG format, and digitize values off the plot by clicking the mouse

on each data point. The numbers are then saved to a text file and used in any spreadsheet program. For an unbiased comparison of results obtained from different methods, we chose to normalize all the results and compare them while keeping a constant mass flow rate. To normalize the streamwise velocity scalar field data at a specific sampling cross section,  $A$ , the volumetric flow rate,  $\dot{V}$ , was calculated using a written MATLAB numerical integration program based on the X-Y line plot of the x-velocity component at that station. The volumetric flow rate through the annular diffuser was derived as:

$$\dot{V} = 2\pi \int_A U_x(r) \times r \times dr \quad (76)$$

From the numerically calculated volumetric flow rate, the average velocity used to normalize the velocity scalar field data, at the considered cross section, was obtained from the following formula:

$$U_{xavg}(A) = \frac{\dot{V}}{A} \quad (77)$$

Furthermore, for the different simulations, the mass flow rate,  $\dot{m}$ , was verified through the formula:

$$\dot{m} = \dot{V} \times \rho \quad (78)$$

For our best case solutions, the mass flow rate was around the experimental value of 6 kg/s, which predicted the radius separation point around the targeted value of 0.255 m. The analysis and interpretation of results were concluded by a brief summary of

key findings, the evaluation of the original assumptions, and an inference of trends obtained by varying the selected inlet parameters.

#### 4.3 Additional Simulations with Selected Inflow Characteristics

Once the initial CFD analysis and CFD approach validation have been completed, additional simulations were run varying the turbulence models, the inlet turbulence intensity, the inlet temperature, and the inlet flow velocity direction.

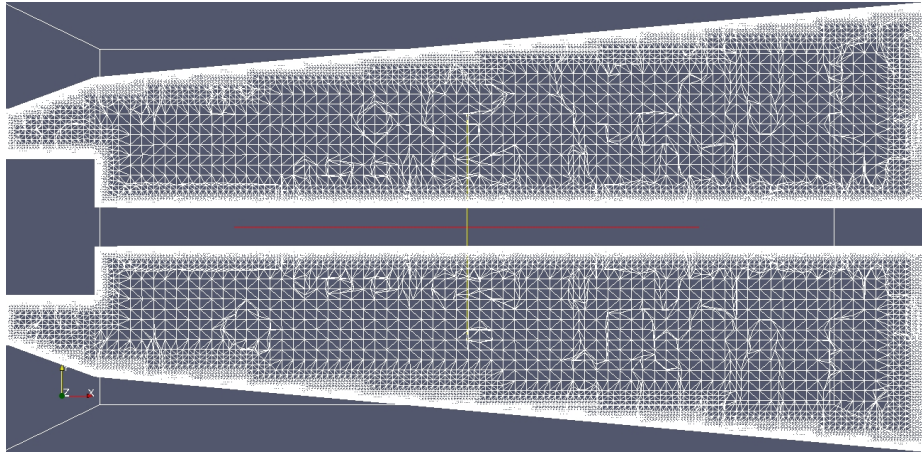


Figure 15: SST  $k - \omega$  best case mesh

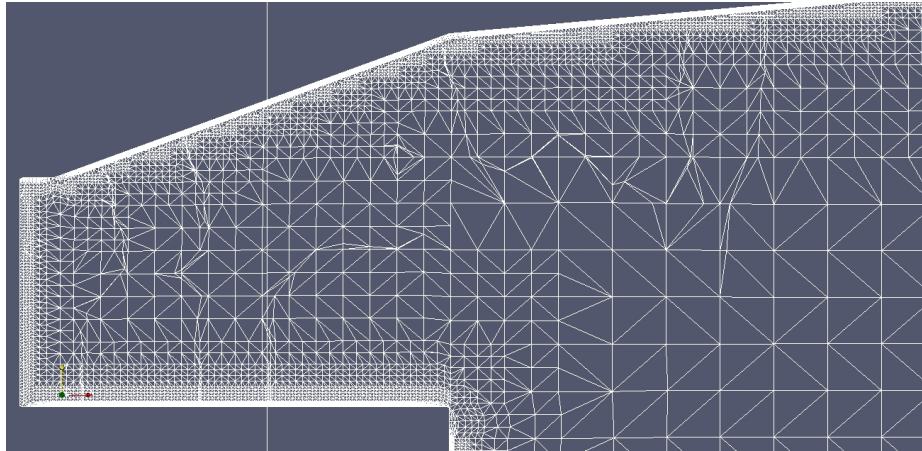


Figure 16: SST  $k - \omega$  annular diffuser closeup mesh

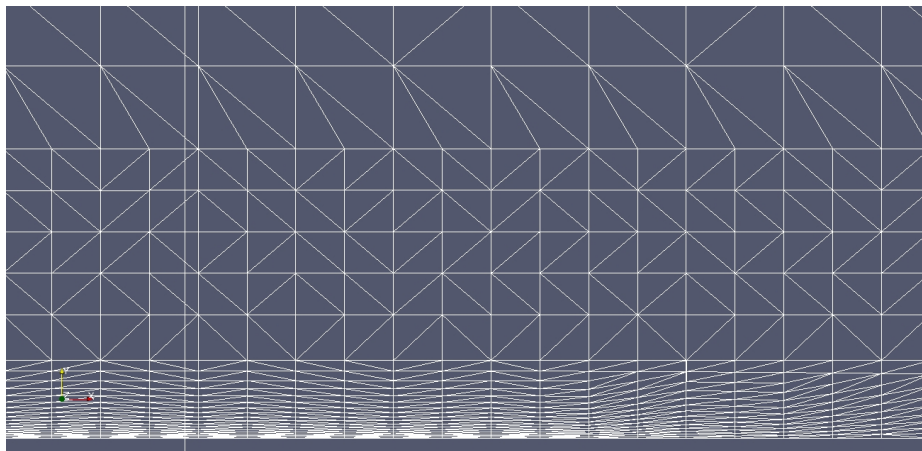


Figure 17:  $k - \omega$  annular diffuser hub 17-cells boundary layer mesh

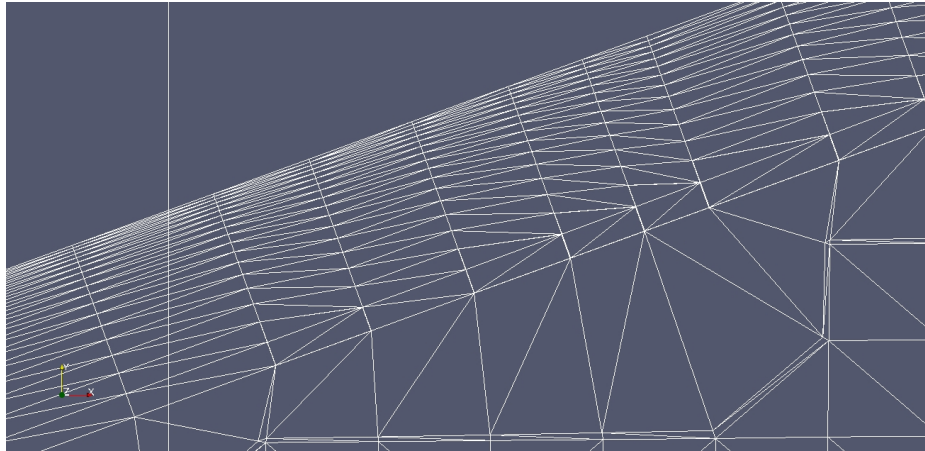


Figure 18:  $k - \omega$  annular diffuser shroud 18-cells boundary layer mesh

## CHAPTER 5: RESULTS AND DISCUSSION

This chapter focuses on the analysis of the results obtained from the numerical investigations of the turbulent flow inside a typical annular-conical gas turbine exhaust diffuser. The sampling of the simulation data was primarily done at seven stations as shown in figure 19. The veracity of various turbulence models in predicting such flows will be investigated first, followed by the examination of the impact of inlet flow parameters on the flow development. These parameters include inlet flow properties as the turbulence intensity, the inlet temperature, and the inlet velocity angle. The influence of turbulence models on the axial velocity prediction will be examined by comparing the CFD results against experimental data obtained from a test rig built at the university of Hannover, Germany. We shall discuss how the flow separation and its reversal are affected by the different parameters considered. Furthermore, the mesh dependence of the CFD solution will be investigated using the  $k - \epsilon$  and the  $k - \omega$  turbulence models. All the variables have been nondimensionalized to ensure sound comparisons. Normalized dimensions are defined as follows,  $r^* = r/h_1$ , with  $h_1$  the diffuser inlet height, and  $x^* = x/L$ , with  $L$  the total length of the exhaust diffuser.  $U_x^* = U/U_1$  is the normalized velocity, with  $U_1$  considered as the inlet velocity. The normalized turbulent kinetic energy is given by  $k^* = (k/U_1^2) \times 100$ .

## 5.1 Flow Development

This section examines flow developments predicted by some turbulence models, starting with the Renormalization Group, RNG, turbulence model. The very complex diffuser flow will be analyzed through plots that will illustrate flow patterns or physical phenomena. The interactions in an incompressible flow field are generally explained in terms of basic concepts such as inertia, pressure forces, gravity forces, viscous forces, vorticity, and energy. Furthermore, vorticity dynamics offers a method to separate a flow into viscous and inviscid effects and this is especially valuable where only a weak interaction exists between them [25]. At the investigated high Reynolds number,  $Re = 4.7 \times 10^5$ , a duct internal flow is characterized by steep velocity gradients producing important viscous effects confined to thin layers located in the wall regions, with the existing active forces generating vorticity. Many engineering processes of interest, such as shear stress, heat, and mass transfer, are controlled by these viscous regions, which frequently become turbulent and complicate the problem [25]. In the case of a fully developed flow, the developing boundary layers will spread through the entire flow field and meet downstream. However, White [41], asserts that tapered flow, such as the diffuser flow, does not become fully developed. Nonetheless, it is very important to know the details of the flow characteristics within these thin growing viscous layers, which reduce the diffuser cross section, and retard the axial flow at the wall.

Furthermore, the center core flow tendency to accelerate is offset by the diverging walls that decelerate the flow and recover pressure. The flow at the entrance and

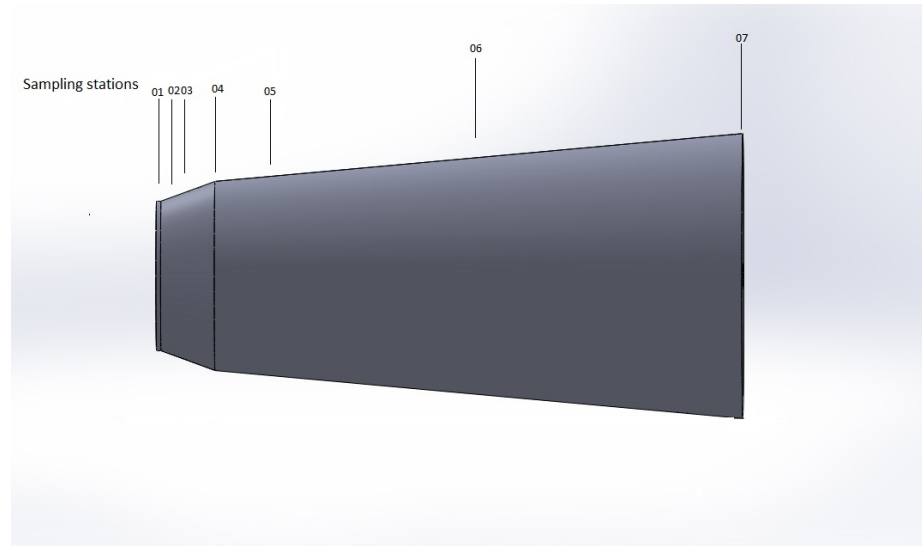


Figure 19: Sampling stations along the exhaust diffuser length

outside the boundary layers may be considered nearly inviscid. Normally, inviscid flows are dominated by the geometry of the walls, i.e. the shape and location of the walls of a duct or a closed body completely establish the velocities and streamlines so that velocities may be found without even using the momentum equation. The pressure field can then be found using the Bernoulli equation, integrated from the momentum equation using the known velocities [25]. From the boundary layer theory, the pressure on the inviscid side of the flow is integrally transmitted to the wall because pressure forces are not modified by the boundary layer. This principle is not applied in the case of the diffuser inclined wall or bluff bodies where regions of separated flows occur, and where the boundary layer theory is no longer valid. With the high diffuser angle in the annular portion of the diffuser, the head loss will be large due to the flow separation and reversal at the casing wall.

Figure 20 shows a region of very lower pressure, i.e. negative pressure, is generated at the diffuser kink, located at the inlet of the annular diffuser. Pressure variation

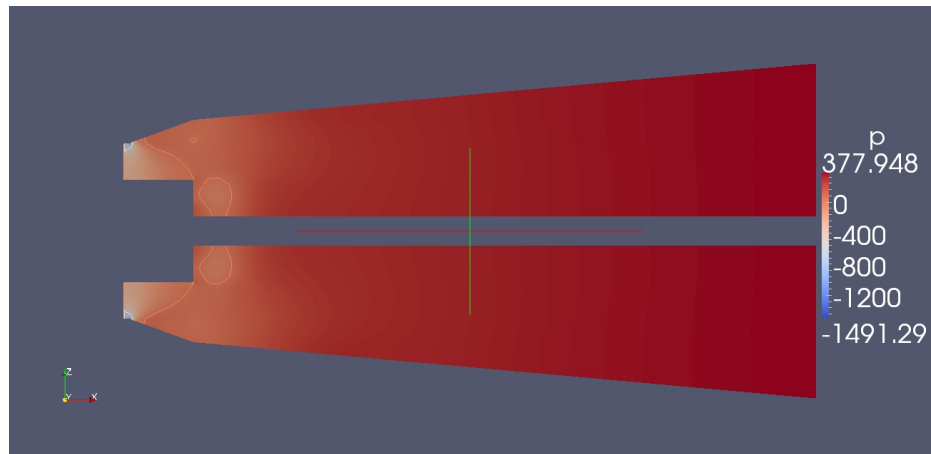


Figure 20: Pressure contour prediction using RNG  $k - \epsilon$  turbulence model

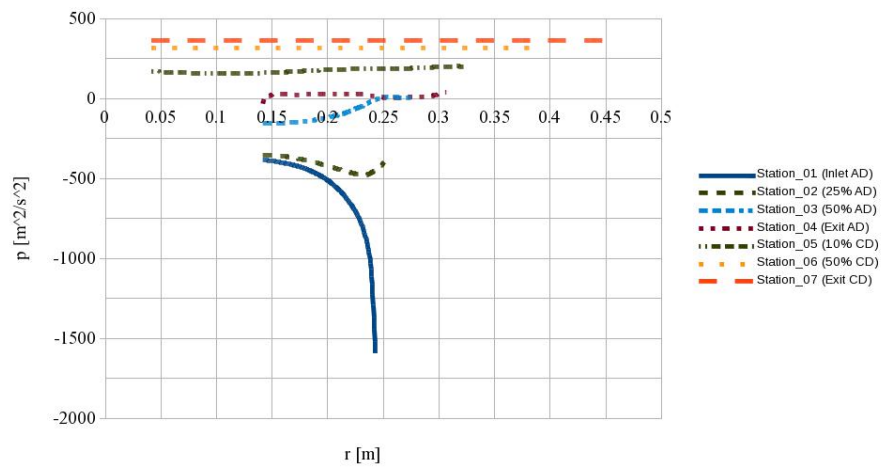


Figure 21: Flow development pressure profiles at different sampling stations

along the diffuser length is represented in figure 21, where it is observed a steady increase in pressure throughout the GT exhaust diffuser. In the core flow region, the rate of pressure increase is significant in the annular diffuser, due to its high apex angle, than in the conical portion of the exhaust diffuser, even though the latter is 11 times longer than the former. This means that, most of the diffusion is accomplished in the annular side of the diffuser. It is observed that between stations 03 and 04 of the annular diffuser, the pressure in the reversed flow region did not change along the diffuser. In general, however, it was observed that the pressure decreases in the boundary layers, i.e. the hub as well as the shroud separated boundary layers. In the core flow region, the pressure stays constant, except between stations 02 and 03 where it varies slightly. Between station 01 and 02, the effect of the diffuser kink, accelerating the flow velocity and considerably reducing pressure, is strongly felt, especially toward the casing region. In the reversed flow region, after the separated boundary layer, it has been observed that the pressure started to increase.

Furthermore, the boundary layer development at the hub, in the annular diffuser portion, is interrupted by the backward-facing step, creating a viscous wake similar to that of flows past immersed bodies. The sudden expansion will provoke a drop in the flow velocity and a sudden increase in the pressure as predicted in figure 20 representing the diffuser pressure field. A line of equal pressure going from the backward-step wall to the annular diffuser casing clearly shows the change in pressure value provoked by the backward step. The additional momentum loss and increase in pressure gradient,  $dp/dx > 0$ , will create conditions favorable to flow separation, reversal, and increased losses. Figure 20 also shows a region of lower pressure right after the

backward step that can justify the flow re-circulation observed at this location.

There will be strong interaction effects between the diffuser viscous boundary layers, the wake after the sudden expansion of the backward-facing step, the mainstream flow, and the separated flows. Such a flow is more suited to be studied experimentally and with CFD. The flow loss will be a combination of wall friction losses and stall losses that arise from boundary-layer separation. Figure 22, representing the velocity field predicted by the RNG  $k - \epsilon$  turbulence model, shows that the flow is symmetric. Stagnation and low velocity regions can be observed either within the flow or towards the diffuser shroud or casing.

At the diffuser inlet, which has a constant diameter section of 15 mm length, the flow velocity is uniform, with a velocity value around 41.16 m/s corresponding to the inlet velocity used in this CFD analysis. Along the outer wall of the constant diameter section, the flow is accelerating reaching a maximum velocity magnitude of about 59 m/s at the beginning of the diverging portion of the annular diffuser. The flow acceleration at the diffuser inlet, predicted by the standard  $k - \epsilon$  turbulence model, can be seen in figure 24. Just a short distance into the diffuser, at about 20% of the annular diffuser length (Station 02), the flow starts to separate from the wall. A region of slow-moving fluid is observed between the core flow region and the reversed region at the diffuser casing, representing the separated boundary-layer region and extending into the conical portion the exhaust diffuser. As we move along the diffuser, flow velocity diminishes, with the core flow moving at a velocity below 20 m/s after station 06 located in the conical portion of the exhaust diffuser. A big separated and reversed flow region is observed at the interface of the annular

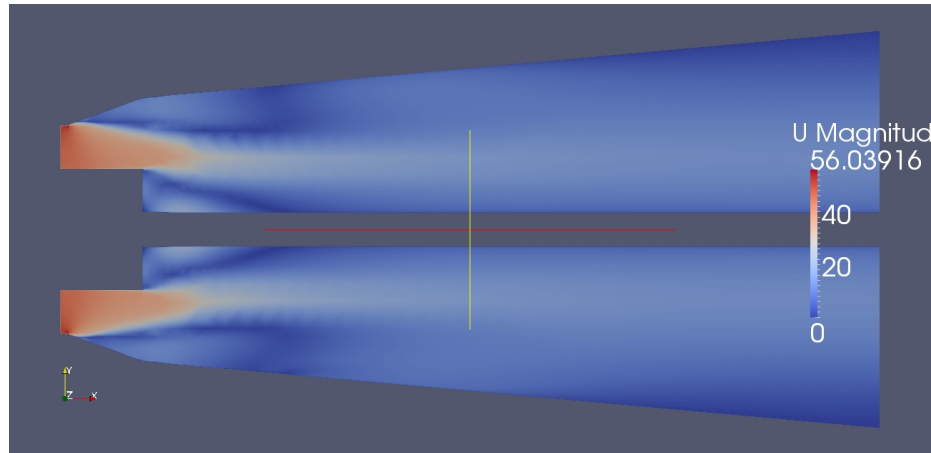


Figure 22: Flow field prediction from RNG  $k - \epsilon$  turbulence model

and conical diffuser (Station 04) before the reattachment of the flow to the diffuser walls in a big portion of the conical diffuser. There is a big velocity drop after the backward-facing step as observed at station 05. We can clearly see separating lines in the flowfield that distinguish the mainstream flow to the separated and reversed flow regions. The boundary layer behavior described previously is the main reason why the studied diffuser, with a high expansion angle has heavy, losses conducting to poor diffuser performance.

The RNG  $k - \epsilon$  turbulence model predicts two major regions where flow reverses, i.e. at the diffuser casing and at the backward-facing step region. At the exit of the conical section, the velocity magnitude looks uniform, with lower values observed at the casing. The  $k - \epsilon$  velocity field prediction shown in figure 23 is similar to that of RNG  $k - \epsilon$  with respect to the symmetry of the flow field. However, the predicted size of the reversed flow region at the casing is smaller compared to that predicted by the RNG turbulence model as exemplified in figure 45. On the contrary, the predicted size of the separation at the backward-facing step region is the same and corresponds

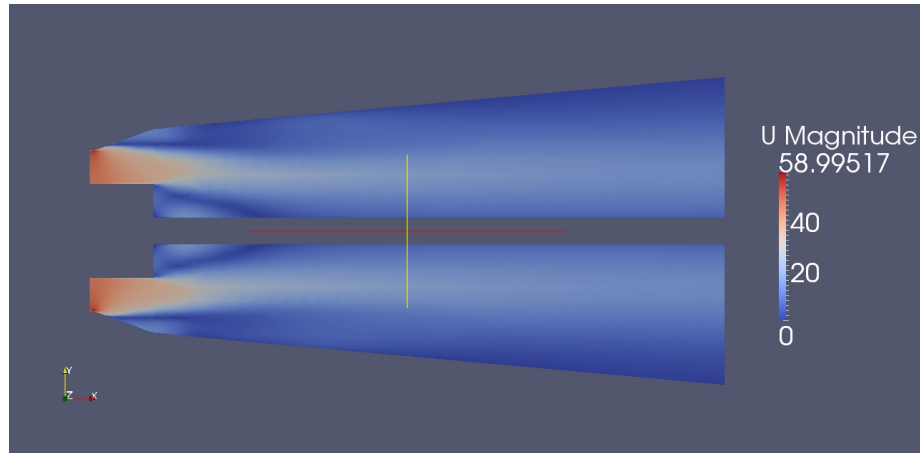


Figure 23: Flow field obtained from the standard  $k - \epsilon$  turbulence model

to that of the experimental value, with the RNG  $k - \epsilon$  turbulence model predicting a higher velocity magnitude within the reversed flow.

The standard  $k - \epsilon$  turbulence model also predicts a large region of slow-moving fluid at the casing, especially on the conical portion of the exhaust diffuser. Compared to the  $k - \epsilon$  turbulence model, the SST  $k - \omega$  predicts even higher velocities at the inlet constant diameter annular section. However, the flow field predicted by the SST  $k - \omega$ , is not symmetric. The line of separation is located towards the casing in the upper half of the diffuser as seen in figure 25, and is undulating along the diffuser length creating multiple separated regions at the top, and one big separated region at the lower wall of the diffuser. The non-symmetric prediction is clearly illustrated at the backward-facing step flow region. Moreover, lower velocity is observed in this region compared to the core flow region creating a shear flow region between them, especially in the upper side of the diffuser. The SST  $k - \omega$  turbulence model does not predict separation at 10% of the conical diffuser length, as well as at the diffuser casing as can be also seen in figure 45. At the exit of the conical portion, the velocity

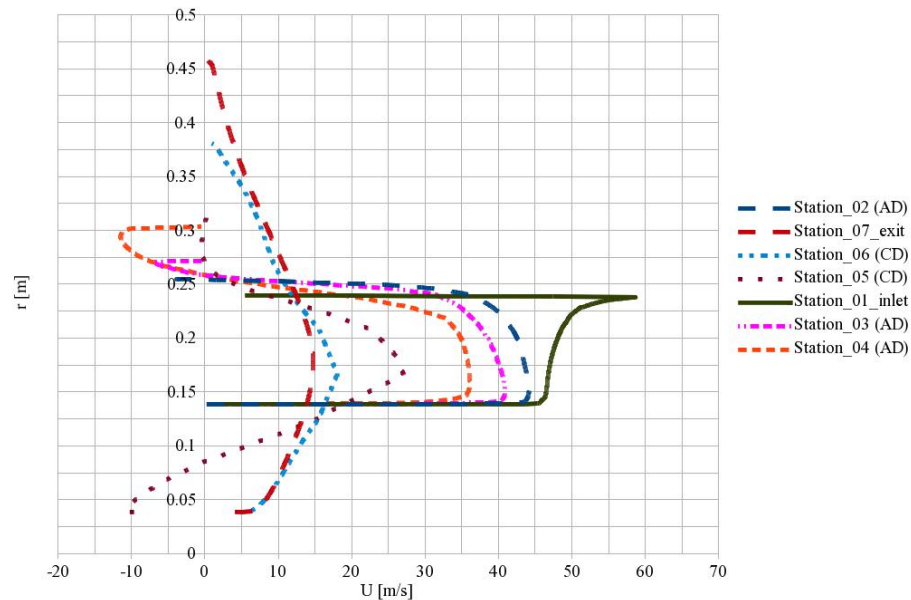


Figure 24: Flow development velocity profiles from the standard  $k - \epsilon$  turbulence model

looks lower over a large portion of the exit cross-section.

We are going now to examine flow streamlines for the RNG  $k - \epsilon$  and the  $k - \omega$  turbulence models. The symmetry of the flow is depicted in the backward-facing step region by the two streamlines covering the re-circulated flow field in this region, and moving along the smaller diameter hub. In the core flow region, seen between two streamlines, the velocity magnitude is noticeably higher than in other regions of the cross-section.

Figure 26, however, uses a larger number of streamlines to show regions of reversed flow, represented with red lines. These regions are localized near the casing, extending from the annular diffuser to about 20 % into the conical diffuser, and at the hub in the back-step region. The streamlines of the velocity field for the SST  $k - \omega$  are represented in figure 27, showing an asymmetric flowfield with a large separated region at the

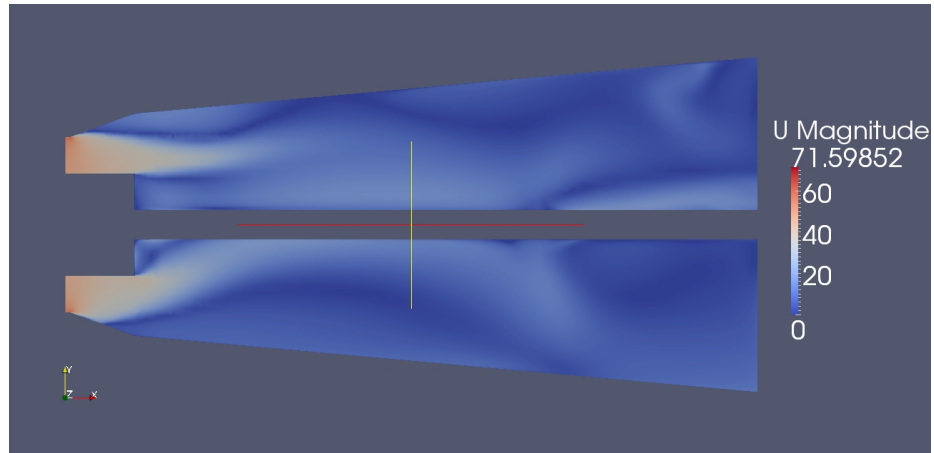


Figure 25: Flow field predicted by the SST  $k - \Omega$  turbulence model

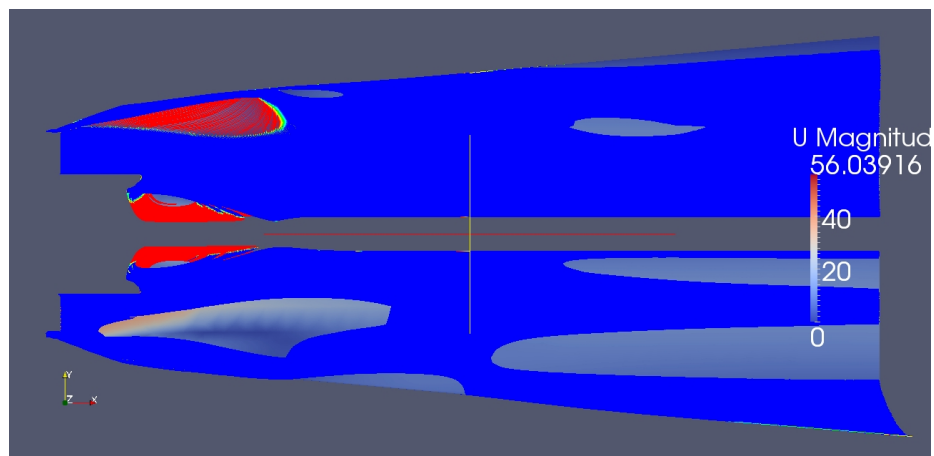


Figure 26: Higher resolution streamline predictions from the RNG  $k - \epsilon$  turbulence model

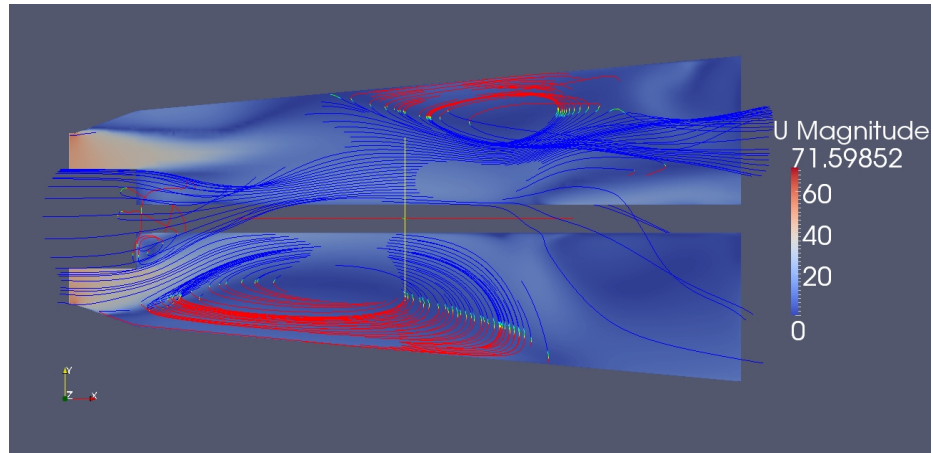


Figure 27:  $k - \omega$  predictions of streamlines

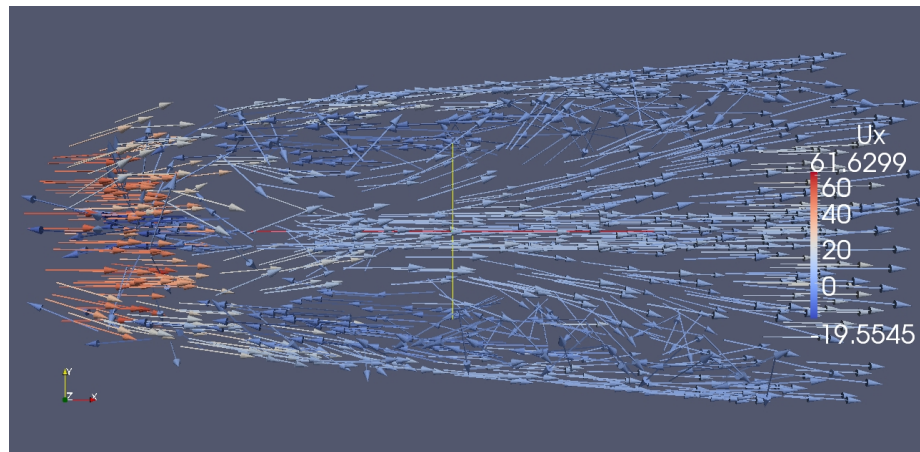


Figure 28: Low resolution  $U_x$  velocity vector from the RNG  $k - \epsilon$  turbulence model bottom and a small one on the top.

A stagnation region, that extends from the annular part of the diffuser to the conical one, separates the core flow and the reversed flow at the diffuser casing. Also a high velocity region exists at the diffuser kink that accelerates the flow. Furthermore, two recirculation regions have been observed in the backward-facing step region. Obviously a high mixing region between these recirculation regions and the reversal flow region exists at the casing, making the flow really irregular at the exit of the annular portion of the diffuser.

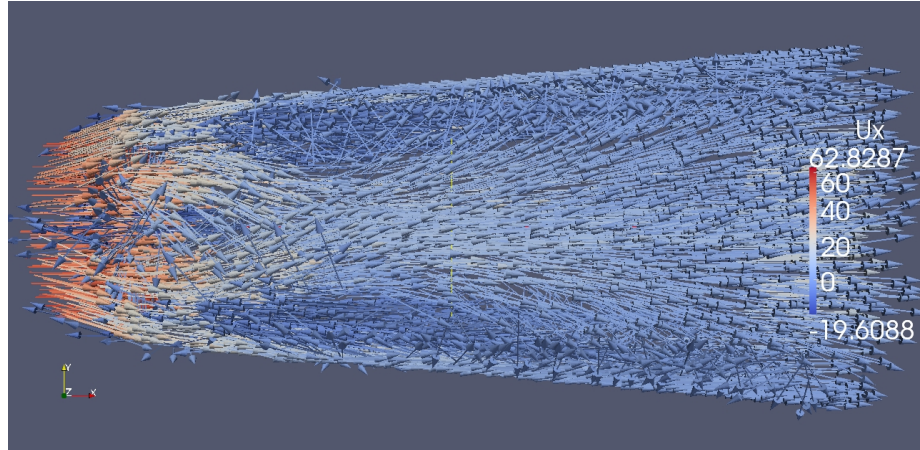


Figure 29: High resolution  $U_x$  velocity vector from the RNG  $k - \epsilon$  turbulence model

A further closer look at the velocity vector plot of figure 28 reveals that towards the center of the diffuser, the two divided streamlines converge in the middle of the diffuser halves to extend the reversed flow region. It is likely that, this side of the reversed region is formed by some of the streamlines pulled earlier by the main flow and thus are being reversed twice. These suggest that the region of reversed flow is mainly made up of fluid from the casing part of the divided flow. Since the pressure is growing toward the end of the diffuser, the adverse pressure gradient is playing a major role in reversing this flow to form a big turbulent bubble with regions of higher mixing, friction, and instabilities.

According to Panton [25], in many situations, it is advantageous to interpret the events occurring in a flow in terms of vorticity and interacting dynamic events producing a certain vorticity distribution. the difference of vorticity indicates that viscous effects are important since a fluid particle can only be set into motion by an unbalanced shear stress [25]. Let us now analyze the axial vorticity magnitude at the middle of the annular diffuser channel height  $r = 0.1915$  m. Figure 30 represents

the magnitude of the vorticity along the exhaust diffuser length on a sampling path. It can be observed that vorticity persists along the diffuser length, representing the vortex interaction on the performance. All three turbulence models predict a sudden increase of vorticity at the backward-facing step, followed by a steady decrease in the conical portion. Since the existence of vorticity is the best way to decide whether a fluid is turbulent [25], it has been concluded that the presence of the backward step is responsible for the high turbulence in this region. The vorticity fluctuations predicted by the SST  $k - \omega$  turbulence model are probably the reason of the nonsymmetry observed in the prediction of the flow field by this turbulence model. The RNG  $k - \epsilon$  turbulence model predicts higher values of vorticity over a long portion of the conical diffuser length. This may explain the higher value of the predicted pressure recovery coefficient as we shall see later, closely followed by the SST  $k - \omega$  turbulence model, then the standard  $k - \epsilon$  turbulence model. Panton also gives a relationship linking the pressure gradient to the vorticity flux across the wall into the fluid. He states that a pressure gradient along the wall is necessary to sustain a flux of vorticity into the fluid. He concluded by indicating that despite the fact that pressure does not directly influence vorticity, the pressure gradient-vorticity flux relations give a coupling whereby pressure forces associated with inviscid motions can introduce vorticity into the fluid.

Figures 32 and 33 show that vorticity is higher very close to the casing wall, reaching a value of 62523.1 right after the kink (Not shown on figure 32 , accompanied with a very low value of the TKE as can be seen on figure 33. The TKE starts to increase when vorticity decreases.

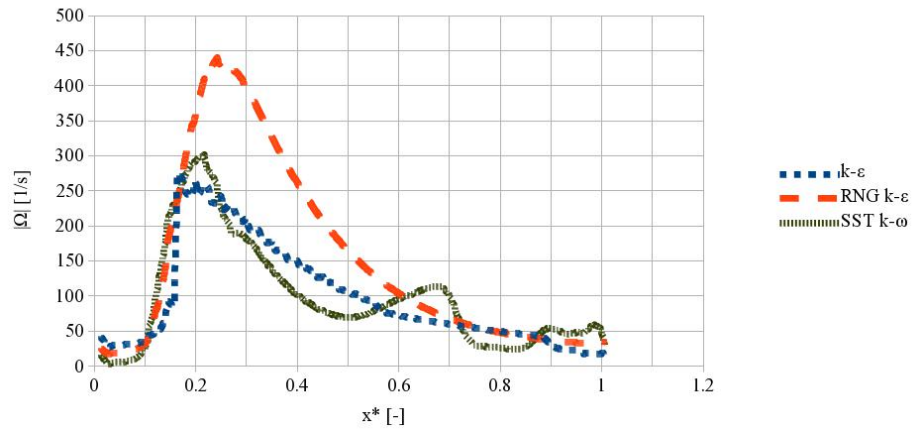


Figure 30: Vorticity magnitude variation along the exhaust diffusion length as a function of turbulence models

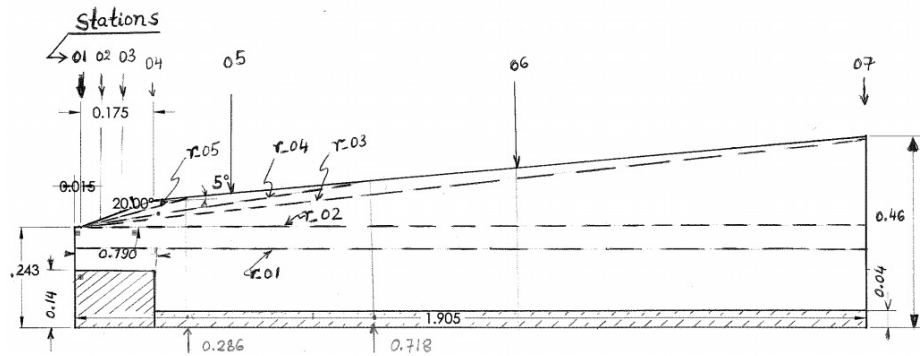


Figure 31: Sampling stations in the shroud reversed flow region and separated boundary layer

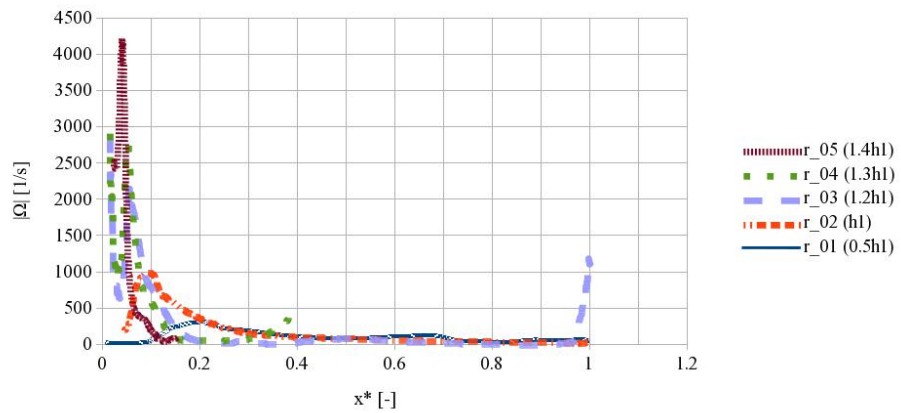


Figure 32: Vorticity variations in the reversed flow region versus diffuser reduced length

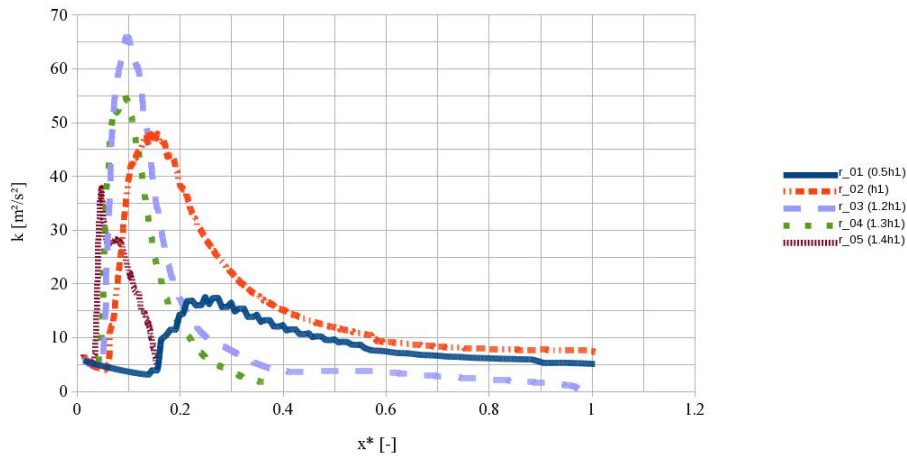


Figure 33: TKE variations in the reversed flow region versus diffuser reduced length

In analyzing the flow development in terms of vorticity at six sampling stations, it was found that the energy of turbulence in the separated boundary layer at the casing was coming from the high vorticity generated near the shroud wall, in the diffuser kink region. Figures 35 and 34 clearly show that along the diffuser length, the TKE becomes maximum in the separated boundary layer when vorticity is minimum. The maximum value of the energy of turbulence and the minimum of vorticity magnitude are located at the separated boundary layer velocity profile point of inflection, P.

The decrease of vorticity in the shroud separated boundary layer along the exhaust diffuser length, accompanied by the increase of the turbulent kinetic energy, are observed only in the annular diffuser portion of the hybrid diffuser. However, in the conical portion of the analyzed diffuser, both vorticity and TKE decrease. In the core flow region, the TKE remains constant at a specific sampling station in the annular diffuser while slightly decreasing along the diffuser length. It then increases slightly at the backward-facing step, with high TKE within the step region before station 04,

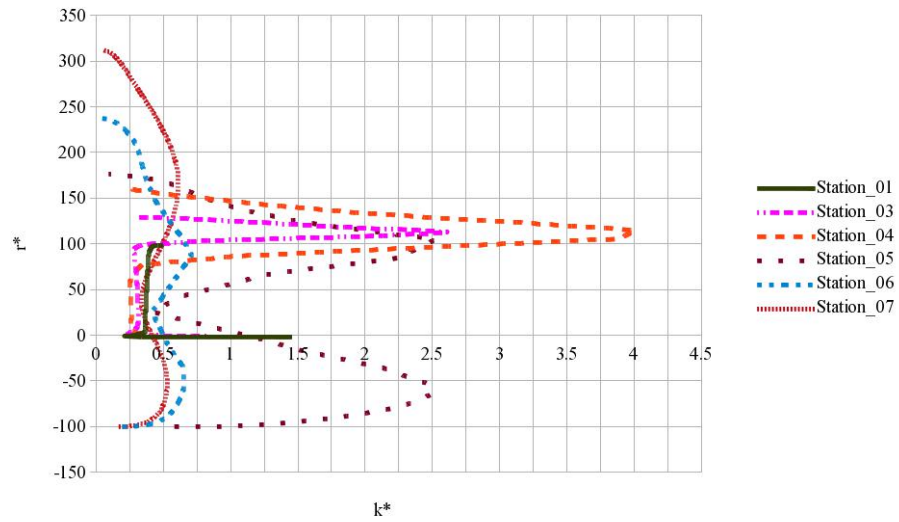


Figure 34: TKE variations along diffuser length at different stations

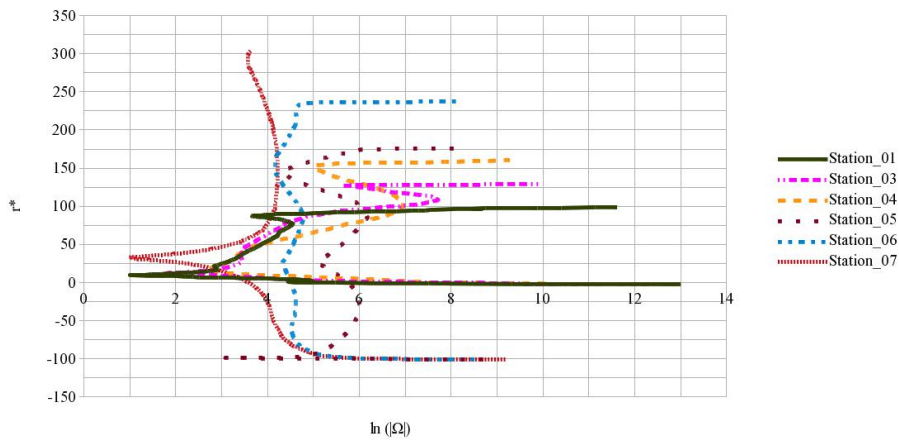


Figure 35: Vorticity variations along diffuser length at different stations

and decreases steadily in the conical diffuser.

## 5.2 The Effects of Mesh Resolution on the Flow Characteristics

Analyses performed in the previous section gave us good feelings for the three-dimensional behavior of the complicated turbulent flow existing in the gas turbine exhaust diffuser. The present section will analyse the effects of increasing the number of cells on the problem solution. Two flow characteristics shall be considered, i.e. the axial distribution of velocity at 50% of the annular diffuser length, and the pressure recovery coefficient throughout the diffuser. The results of gradual increase of the computational cell count on the axial velocity distribution are presented in figure 36. The present analysis starts with a lower mesh resolution case where flow reversal, at the considered diffuser cross section, is not predicted, and concludes with the two best cases of our investigations that required high-resolution meshes. The CFD results presented were obtained using the standard  $k - \epsilon$  and the SST  $k - \omega$  turbulence models, with the number of computational cells varying from 7.4 to 47.3 million cells. While running the simulations, solution mesh independence was tested using successive higher density meshes, and observing the resulting variation in mean flow properties, namely, the predicted mean flow velocity and the predicted pressure recovery coefficient. The simulated mean flow velocity profile, at 50% of the annular diffuser length and a radius of 0.273 m, has been compared to the experimental one to ensure that they closely match, and that the predicted axial velocity approaches a value of zero at the flow reversal point, estimated at a radius of 0.255 m. Comparing the resulting CFD predictions to experimental results, it has been observed that the

solution progressively improved with the gradual increase in cell count until we could not observe any further enhancements. At the beginning, for 2.2 million difference in the number of cells, the standard  $k - \epsilon$  turbulence model predictions show a significant improvement of the solution. The change in the solution then decreased as the number of cells increased, with the solution approaching the experimental results. It is worthwhile noting here that another major improvement in the predicted solution has also been obtained when switching from the standard  $k - \epsilon$  turbulence model to the SST  $k - \omega$  turbulence model. The latter requires a higher number of cells and a higher mesh resolution in the boundary layer region, producing a  $y^+$  value well below 1 at certain regions of the geometry boundary. One of the foci of the approach validation process was to achieve credible predictions using appropriate turbulence models and wall functions, ensuring that  $y^+$  values remained within the range of the applicability of those models. The standard  $k - \epsilon$  turbulence model predicted an average  $y^+$  value of about 6.4 at the hub of the diffuser, and  $y^+ = 13.2$  has been predicted at the casing. Using the SST  $k - \omega$  turbulence model, the average  $y^+$  value of 1.62 was predicted at the diffuser hub, and about  $y^+ = 2.58$  at the casing of the diffuser. Even though the average  $y^+$  for both turbulence models considered were within acceptable ranges, the maximum at some points of the geometry boundary reached 232.7 for the standard  $k - \epsilon$  turbulence model and 153.8 for the SST  $k - \omega$  turbulence model.

The improvements of the solution have been observed and tracked at two different levels. Firstly, as the number of cells was increased, the normalized predicted maximum velocity approached the normalized maximum velocity obtained from ex-

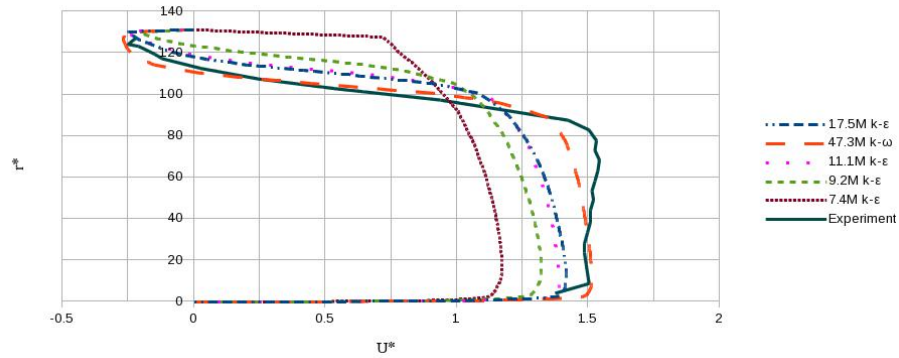


Figure 36: Axial distribution of velocity varying cell count

perimental data. Secondly, the separated region and the separation point improved from no separation to conditions approaching experimental results, with the standard  $k - \epsilon$  turbulence model best results underpredicting the size of the separated region, while the SST  $k - \omega$  turbulence model best results overpredicted it. In the reversed flow region, The maximum normalized axial velocity predicted by the standard  $k - \epsilon$  turbulence model is in very good agreement with experiment, whereas the SST  $k - \omega$  turbulence model slightly overpredicts the normalized reversed region maximum velocity. The latter, however, better predicts the axial velocity profile that is in good agreement with experiment in the casing boundary layer region, where a high velocity gradient exists.

In figure 37, the axial distribution of the pressure recovery coefficient is also analyzed by varying the number of cells. The simulation results show that the predicted pressure recovery coefficient is dependent on the number of cells used in the computational domain. This is clearly shown in the conical portion of the exhaust diffuser. However, in the annular part of the studied exhaust diffuser, all CFD predictions coalesce with the ideal pressure recovery coefficient until they reach a  $C_p$  value of

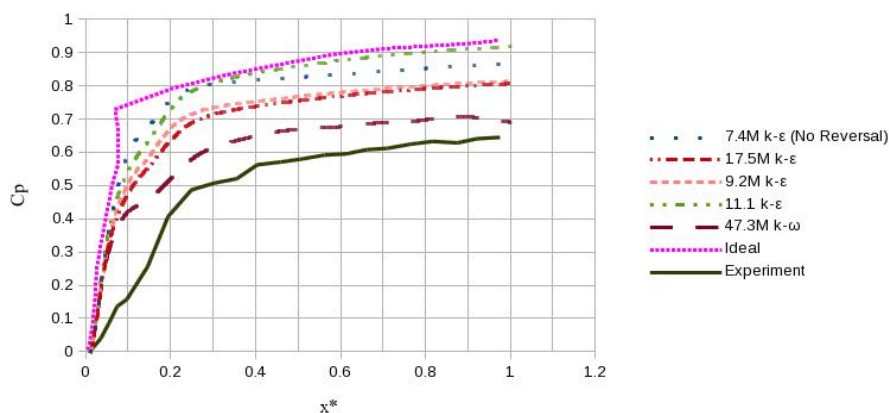


Figure 37: Axial distribution of pressure recovery coefficient varying cell count

about 0.45, before taking different paths. For the selected cases, the pressure recovery coefficients are overpredicted as compared to experiment due to the use of the standard  $k - \epsilon$  turbulence model. At the end of the conical diffuser portion, the non-reversed case, which had 7.4 million cell count, predicts a lower value of  $C_p$  than the case with 11.1 million cell count, which is of course an unrealistic prediction since the actual flow physics, i.e. flow reversal at the casing was not captured. The 11 million case, however, follows the ideal  $C_p$  calculation curve except for the region between the exit of the annular diffuser and the inlet of the conical part. There is also some inconsistencies between the 9 million case and the 11 million case with the latter, though having more cell count, predicts poor results compared to the former. The difference may be due to the mesh quality between the two cases. In summary, it can definitely be concluded that as the number of cells increases, the pressure recovery coefficient will approach the experimental results and, for lower mesh resolution, the predicted  $C_p$  will tend to follow the ideal pressure recovery coefficient curve.

The numerical solution described in this chapter illustrates the gas turbine fluid

flow behavior, and the practical results function of some inlet flow properties using the CFD analysis tool. Even though these results are approximate digital computer solutions, they have shed a light on the changes that these inlet flow characteristics may produce in a typical diffuser fluid flow behavior. A successful CFD design of a diffuser should endeavor to alleviate the harmful effects of adverse pressure gradient and those of flow separation and reversal.

### 5.3 The Effects of Turbulence Model on the Flow Characteristics

Six different turbulence models have been evaluated during our investigations. Figure 38 shows the computed normalized axial velocities, at 50% annular diffuser length, obtained from four turbulence models. These turbulence models are the  $k - \epsilon$ , the RNG  $k - \epsilon$ , the SST  $k - \omega$ , and the Spalart-Allmaras turbulence models.

One prominent feature in Fig. 38 is the flow separation with backflow at the diffuser casing. This important effect is caused by excessive momentum loss in the outer-wall boundary layer trying to move forward against increasing adverse pressure gradient,  $dp/dx > 0$ , as the diffuser area expands. A geometric argument about the second derivative of the velocity profile at the wall can help elucidate this phenomenon. Let us consider the x-momentum relation of the equation of motion:

$$\rho\left(\frac{\partial u}{\partial t} + u\frac{\partial u}{\partial x} + v\frac{\partial u}{\partial y} + w\frac{\partial u}{\partial z}\right) = -\frac{\partial p}{\partial x} + \mu\frac{\partial^2 u}{\partial x^2} + \mu\frac{\partial^2 u}{\partial y^2} + \mu\frac{\partial^2 u}{\partial z^2} \quad (79)$$

At the wall, the velocity components  $u = v = w = 0$ . Prandtl, 1904, showed that for a large Reynolds number, the shear layer at the wall must be very thin so that  $v$  and  $w \ll u$ , and can be neglected. Furthermore, the rates of change of  $u, v, w$  in

the streamwise direction are very small compared to the rates of change in the y- and z-directions. With these approximations in mind, the y- and z-momentum equations can be neglected, and the pressure will vary only with x so that we can replace the partial derivation by the total derivation. The above equation, for a steady-state two-dimensional incompressible flow, then simplifies to:

$$0 = -\frac{dp}{dx} + \mu \frac{\partial^2 u}{\partial y^2} \quad (80)$$

with:

$$\frac{1}{\mu} \frac{dp}{dx} = \frac{\partial^2 u}{\partial y^2} \quad (81)$$

This equation shows that in an adverse pressure gradient, the second derivative of the velocity will be positive at the wall. Since the flowing core has favorable pressure gradient, the second derivative of the velocity must be negative outside the boundary layer for smooth merging of these two portions of the flow. Thus, the second derivative must pass through zero somewhere between the backflow and the mainstream flow. On the velocity profile, this happens at a point of inflection, giving any boundary layer profile, in case of an adverse pressure gradient, a characteristic S-shape. This point of inflection is located in the boundary layer, with its distance from the wall increasing as the adverse pressure gradient increases [42]. The flow profiles of figure 38 illustrate this fact, with the point of inflection located at about  $r^* = 100$  and  $Ux^* = 0.7$ . All tested turbulence models predict this point of inflection except the Spalart Allmaras turbulence model, which did not predict flow separation and reversal. The analysis

allows us to conclude that the separated boundary layer actually moved down, and is located between the normalized radii of about  $r^* = 80$  and  $r^* = 112$ , as shown on the experimental data velocity profile. The high velocity gradient at the casing is thus located within the casing boundary layer, and the backflow will be accompanied with increased losses, unsteadiness, and decreased pressure recovery. White [41], asserts that tapered flow, as the one in a diffuser, does not become fully developed, i.e. wall boundary layers do not merge downstream. This assertion is confirmed here, where the limits of both wall boundary layers are visible, showing high velocity gradients within short distances in the wall regions. The velocity profile in the core flow, however, tends not to vary much, especially as shown by experiment.

It can be observed that the SST  $k - \omega$  turbulence model shows better agreement with experimental results compared to the three other turbulence models. However, it slightly overpredicts the size of the separation region at the casing and the magnitude of the velocity in this separated and reversed flow region. In general, all our CFD computations fail to reproduce a vertical velocity profile in the middle of the diffuser channel as obtained experimentally, since flow separation usually results in flow acceleration in the middle of the channel due to mass continuity [27]. Furthermore, notwithstanding using more than 15 prism layers to resolve the boundary layer at the diffuser hub, the boundary layer thickness obtained through experimentation could not be appreciably well reproduced in this region by any of the turbulence models, except with the RNG  $k - \epsilon$  results where we can observe a slight thickness of the hub boundary layer. The use of more than 20 prism layers caused the reduction in the overall cell count, and subsequently reduced the accuracy of the computation. The

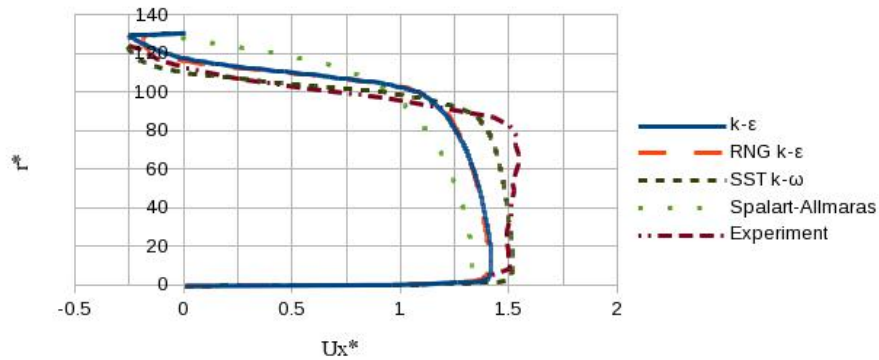


Figure 38: Combined normalized axial velocities at  $x/h_1 = 1.01$ , 50 % annular diffuser varying turbulence models

$k - \epsilon$  and RNG  $k - \epsilon$  turbulence models gave essentially the same results, with the former producing almost the same velocity magnitude in the reversed region as the experiment; however, both underpredict the size of the reversed region.

Moreover, variants of the  $k - \epsilon$  turbulence models underpredict the axial velocity in the middle of the diffuser channel where the core flow develops. They, however, overpredict the axial velocity in the region closer to the reversed flow region. As for the Spalart-Allmaras turbulence model, its results were far off from the experiment, seriously underpredicting the size of the separated region and the axial velocity magnitude.

Figure 39 shows the normalized axial velocity distributions at the middle of the annular diffuser portion, and compares the computed  $k - \epsilon$  results to the experiment and another CFD computation by David et al.[14], also using the standard  $k - \epsilon$  turbulence model. Our results match the results of David et al. towards the casing region before the flow reversal, but our CFD approach better predicted the axial velocity magnitude in the reversed region, which is much more closer to experimental

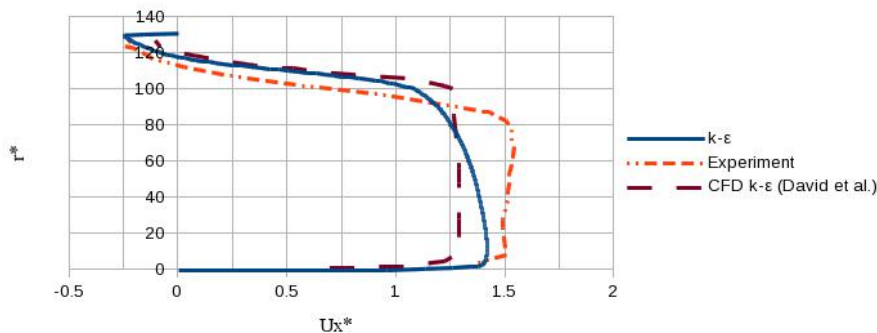


Figure 39: Normalized  $U_x$  at  $x/h_1 = 1.01$ , 50 % annular diffuser

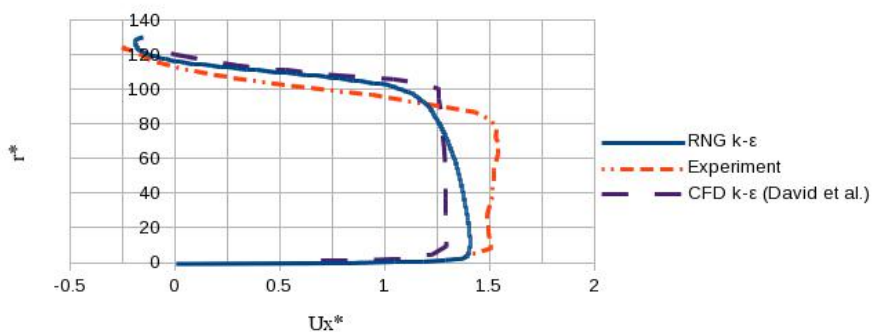


Figure 40: Normalized RNG  $k - \epsilon$   $U_x$  at  $x/h_1 = 1.01$ , 50% annular diffuser

results. Both, nevertheless, underpredict the size of the reversed region. It can be seen from the figure 39 that our predictions of the axial velocity profile from the hub to the middle of the channel is located mid-way between the experiment and David et al. CFD computation. Our  $k - \epsilon$  CFD predictions thus produces a better axial velocity magnitude in the middle of the diffuser channel with velocity values closer to experiment than the CFD predictions of David et al.

In figure 40, the computed axial velocity obtained with the RNG  $k - \epsilon$  is presented. The results are similar to the standard  $k - \epsilon$ , except in the reversed flow region where the former underpredicts the magnitude of the reversed flow velocity with

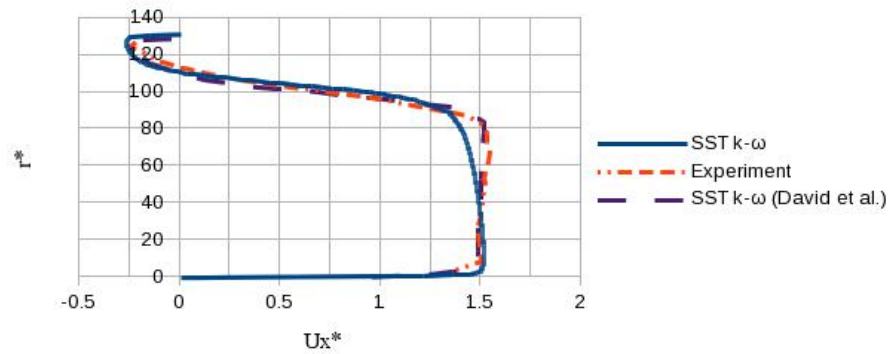


Figure 41: Normalized SST  $k - \omega$   $U_x$  at  $x/h_1 = 1.01$ , 50% annular diffuser

a slightly bigger reversed region extending towards the separation point obtained experimentally.

Now let us analyze computed results obtained using the SST turbulence model shown in figure 41. This turbulence model combines the benefits of both  $k - \epsilon$  and  $k - \omega$  turbulence models, with the former applied in the outer turbulence wall region and the latter in the near-wall region to capture a realistic boundary layer flow without wall function implementations. In this manner, the strong sensitivity of  $\omega$  to freestream condition is avoided. The predicted results are compared to experiment and those of David et al. SST calculations. Both CFD calculations show better agreement with experiment, however, David et al. used the SAS-SST (Scale Adaptive Simulation with the Shear Stress Transport turbulence model) model for unsteady simulation with features comparable to LES. The SAS model is an improved URANS-type model [14]. predictions closely match experiment results in the channel core flow region. The two SST  $k - \omega$  numerical simulations slightly overpredict the size of the separated region, while predicting the same separation point.

The velocity trend in the separated boundary layer at the casing is well predicted

by all the tested turbulence models, but with different level of accuracy. At 50% of the annular diffuser length, where the total height is about 133.2 mm, the flow field is divided into four regions, i.e., the hub boundary layer region which is only 6% of this height, or about 8.112mm, the core flow region which makes up 55% of the height, or 73 mm, the separated boundary layer region towards the diffuser shroud, 26% or 26 mm, and the reversed flow region, 13% or 17 mm. Comparing the boundary-layer thickness of the constant diameter hub to that of the inclined diffuser wall, the latter is four times thicker than the former. This difference is due to the high value of the diffuser opening angle producing an adverse pressure gradient that thickens the boundary layer to the point of separating it from the wall. This thickness will thus vary with the diffuser opening angle until a regime similar to that of a jet flow is reached for a specific diffuser angle. How this boundary-layer thickness varies, for this type of diffuser, would be something that can be investigated. The hub boundary-layer mesh created to resolve this region has an average thickness of 4 mm, while experiment shows a boundary layer thickness of about 8mm. All the attempts to add more prism layers, at the hub as well as at the casing, resulted in a diminished overall cell count as mentioned before. It is important to note that the OpenFOAM implementation of the SST  $k - \omega$  turbulence model, version 2.0.1, uses some type of wall function contrary to what has been said earlier about the particularity of the SST turbulence model to not use any wall function.

The next analysis evaluates predictions of the normalized turbulent kinetic energy, TKE, at the same location as previously, i.e. the middle of the annular diffuser section. First, let us look at the predictions of the turbulent kinetic energy, obtained

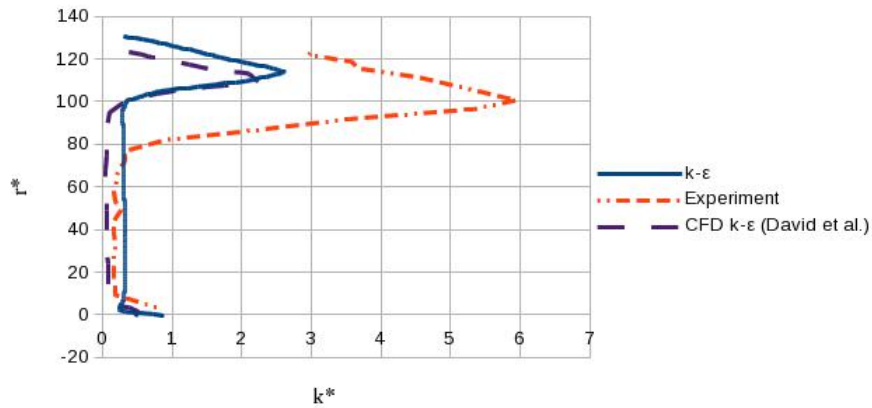


Figure 42: Normalized  $k - \epsilon$  turbulent kinetic energy at  $x/h_1 = 1.01$ , 50% annular diffuser

by the standard  $k - \epsilon$  turbulence models used in the current study and in David et al. Figure 42, shows good agreement in the core flow region of the diffuser, where very low TKE values are observed. However, in the region towards the casing wall, both CFD calculations significantly underpredict the TKE, with their maximum values almost one third of that of the experimental results. The poor predictions of turbulent kinetic energy infer that the tested turbulence models are very dissipative in this region, and, thus, prone to over-predicting flow reversal, high level of mixing and friction. The dissipation is generated by viscous shear stresses performing deformation work that increases the internal energy of the fluid and decreases the turbulent kinetic energy [33]. These poor predictions of the TKE can also be observed in the diffuser hub boundary layer as well, but to a less extent. In the core flow region, the turbulence model used by David et al. is more dissipative than the  $k - \epsilon$  used in OpenFOAM, which slightly overpredicts TKE; it is even more dissipative in the reversed flow region, starting from the velocity inflection point. The experiment also gives higher

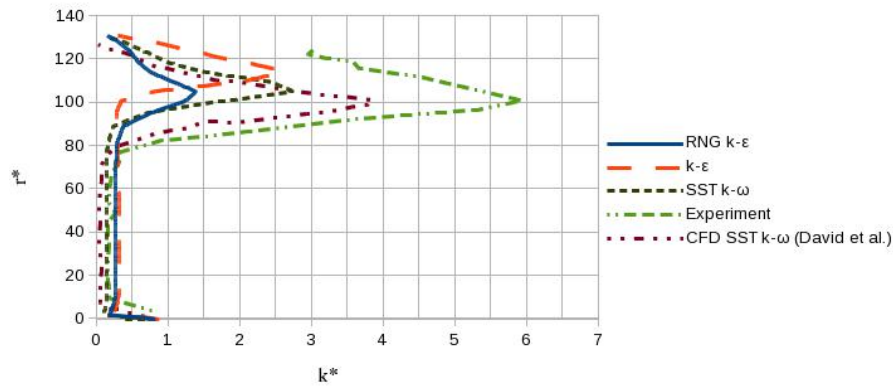


Figure 43: Normalized turbulent kinetic energies at  $x/h_1 = 1.01$ , 50% annular diffuser values of the turbulent kinetic energy over a wider region towards the diffuser casing than CFD. Our CFD calculations closely predict the TKE trend in the hub boundary region, with slightly lower values than experiment.

Figure 43 represents computed turbulent kinetic energy obtained from different turbulence models compared to experiment and David et al. CFD simulations. The SST  $k - \omega$  turbulence model used by David et al. is less dissipative than that of the current study. It predicts the TKE close to experiment up to 76% of the annular diffuser height, at the measuring station located at 50% of the annular diffuser length. Furthermore, the location of the maximum value predicted is exactly the same as the one obtained from experiment. This maximum is also located at about 76% of the measuring station annular diffuser height, right in the middle of the separated boundary layer towards the diffuser casing. The OpenFOAM SST  $k - \omega$  turbulence model comes next in terms of being less dissipative, with its maximum TKE prediction slightly greater than that of the OpenFOAM  $k - \epsilon$ . The RNG  $k - \epsilon$  turbulence model along with the OpenFOAM SST  $k - \omega$  turbulence model predict the same location

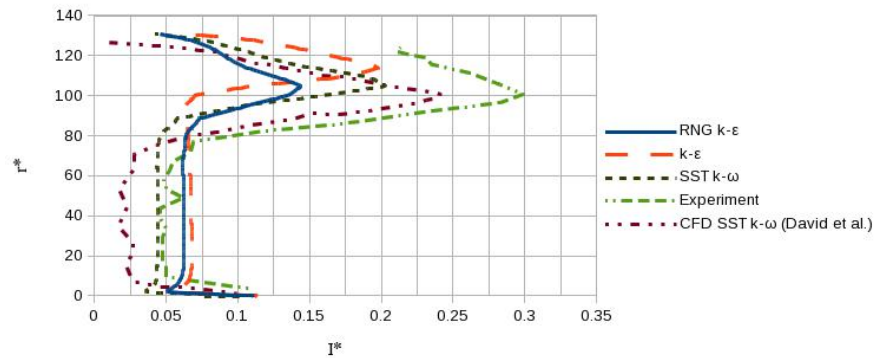


Figure 44: Normalized turbulence intensities at  $x/h_1 = 1.01$ , 50% annular diffuser

of the maximum value of the turbulent kinetic energy. The former, however, is very dissipative, and the location of the maximum value predicted by the OpenFOAM  $k - \epsilon$  turbulence model is located more towards the diffuser casing. It is observed that the turbulent kinetic energy starts to depart considerably from experiment at the beginning of the third region, which is the separated boundary layer, all the way to the flow reversal region. Towards the casing reversed flow region, very low values of the turbulent kinetic energy are obtained compared to experiment. The same thing is observed in the hub boundary layer region where we also have a high velocity change in the height direction.

At the casing wall, the TKE increases throughout the reversed flow region. This increase continues in the casing boundary layer until the point of inflection of the velocity profile in this region is reached. As we move beyond this point and toward the core flow region, the steady increase of velocity is accompanied by a sharp decrease in TKE, which remains constant and low in the mainstream flow. Thus, it has been observed that the flow is more turbulent, with high TKE, in the reversed region and

the boundary layers, i.e. towards the walls, than in the diffuser core flow. In figure 44, we represent the normalized turbulence intensities calculated from the turbulent kinetic energy obtained using the tested turbulence models. The trends are the same as for the predicted TKEs, which have been multiplied by a certain factor. It can be seen here that all the turbulence intensity predictions tend to converge to the same values at the hub and casing walls.

Theoretical analysis predicts that the diffuser performance, in terms of the pressure recovery, depends on the uniformity of the flow characteristics at the diffuser exit. Figure 45 represents axial velocity distributions at the exit of the annular diffuser, which is the inlet of the conical diffuser, characterized the presence of a backward-facing step. It is observed that the axial velocity profile, at this measuring station, is not uniform, and is even negative in some regions as predicted by experiment and some turbulence models. This observation infers that the diffuser pressure recovery coefficient shall have lower values in the annular diffuser portion of the studied hybrid diffuser. For all the turbulence models represented, only the OpenFOAM standard  $k - \epsilon$  turbulence model reasonably predicts the trend obtained by experimental investigations. The RNG turbulence model considerably overpredicts the axial velocity magnitude in the core flow region, while predicting huge separation and reversal of flow at the diffuser wall regions. The size of the separated flow at the hub backward-facing step has been, however, well predicted by all the considered turbulence model except the OpenFOAM SST  $k - \omega$  turbulence model, which did not predict, at this location, any separation or reversal of flow from the diffuser hub or the outer wall.

With the last observation, it seems like the accuracy of a turbulence model along

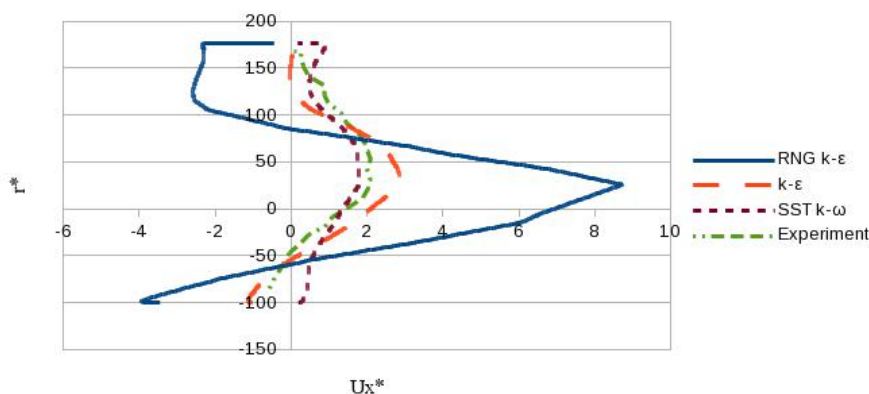


Figure 45: Axial velocities at  $x/h_1 = 1.92$ , 10 % conical diffuser length

the diffuser length, in predicting the relevant flow characteristic, depends upon the actual physics existing at a specific location of the exhaust diffuser. The predicted velocity profiles present at least two inflection points, where it is observed a peaking of the TKE profiles at the hub and casing walls. Figure 46 shows the effect of the backward-facing step on the turbulence generation, at the inlet of the conical diffuser, on the turbulence kinetic energy distribution function of the turbulence model used. The first observation is that all turbulence models predict doubled maximum values of the TKE. However, its location at the casing remains the same despite the abrupt geometrical change of the diffuser hub radius. Secondly, it can also be observed that from the virtual hub in the conical portion, which has the same radius as that of the annular portion of the diffuser, the predicted TKE profiles coalesce in the core flow region for all tested turbulence models. Their values are identical to the predictions in the annular portion of the exhaust diffuser, and remain constant only over a portion of the previously observed core flow height. This creates a wider region towards the casing where a high gradient of the turbulence kinetic energy, and likely high mixing

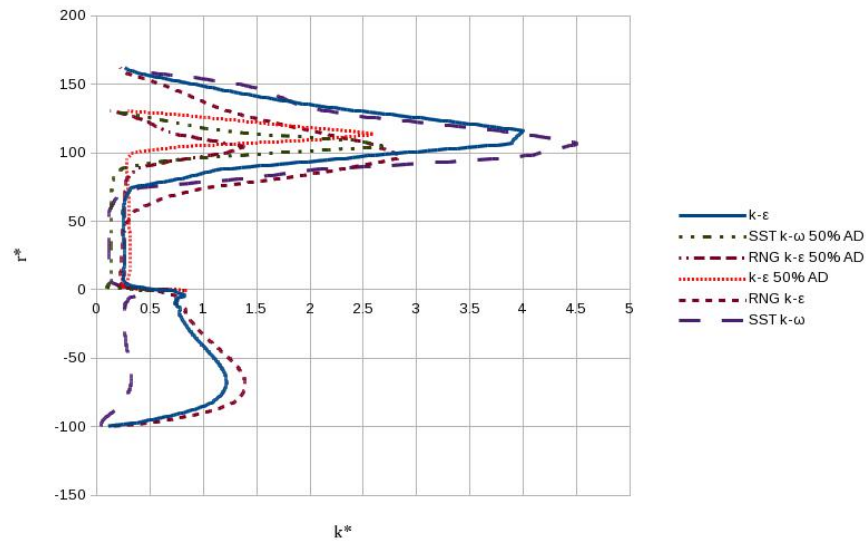


Figure 46: Normalized turbulent kinetic energy at  $x/h_1 = 1.92$ , inlet conical diffuser and shear exist as can be seen in figure 29, where two big recirculation regions towards the casing in the backward-facing step region..

When analyzing predictions by the three turbulence models considered, i.e., the standard  $k - \epsilon$ , the RNG  $k - \epsilon$ , and the SST  $k - \omega$  turbulence models, it was observed that the latter predicts higher values of the turbulence kinetic energy in the casing boundary layer region, slightly below half of the experimental value, closely followed by the standard  $k - \epsilon$ , and then the RNG  $k - \epsilon$ . On the contrary, in the recirculation flow region of the backward-facing step and in a large portion of the core flow region, the SST  $k - \omega$  is the one that predicts lower values of the TKE, followed by the standard  $k - \epsilon$ , and finally the RNG  $k - \epsilon$ . For the turbulence models considered in figure 46, the predictions at the virtual hub are identical before departing from each other as we move towards the conical diffuser hub. These virtual hub predictions

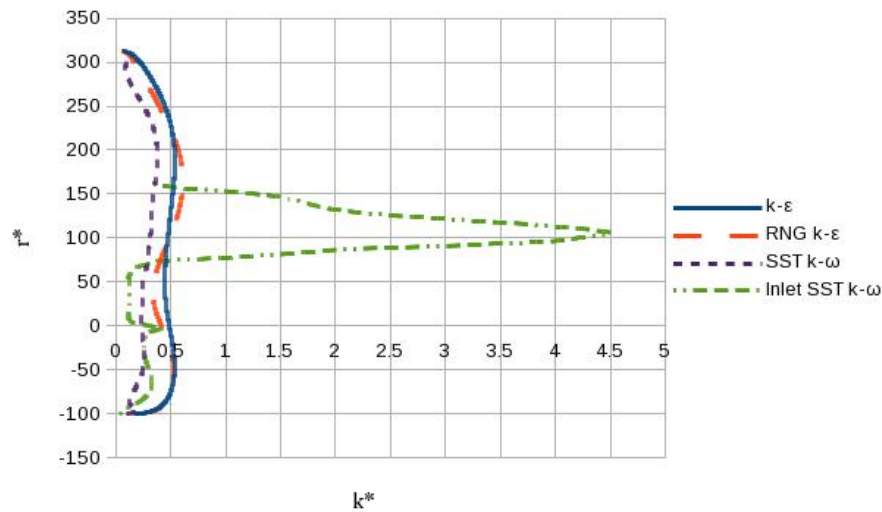


Figure 47: Normalized turbulent kinetic energy at  $x/h_1 = 18.69$ , exit conical diffuser after the backward-facing tend to increase due to the shear layer existing between the backward-facing step reversed flow and the main flow. The turbulence kinetic energy at the exit of the conical diffuser has also been examined and compared to the predictions at the inlet as depicted in figure 47. The TKE profiles at the exit of the conical diffuser, produced by the different turbulence models show some uniformity of values than at the inlet, where a great peak value, almost eighteen times, is predicted by the SST  $k - \omega$  turbulence model. According to the relevant existing theory, this uniformity of flow properties may explain why the predicted pressure recovery coefficient is greater in the conical diffuser portion than in the annular portion of this type of exhaust diffuser.

Finally, let us consider the effects of turbulence models on the basic output of a diffuser, the pressure-recovery coefficient,  $C_p$ ; the higher the value of  $C_p$ , the better is the diffuser performance. Figure 49 represents the ideal, experimental, and predicted

axial distributions of pressure recovery coefficients. The plotted predicted profiles were calculated using equation (26) and predicted pressure values from the three turbulence models at the middle of the exhaust diffuser. The pressure recovery coefficient can be calculated this way using the axial distribution of static pressure along the whole diffuser. No area averaged static pressures are used in this case [27]. Figure 48 shows reduced pressure distributions predicted at station 04 by the four turbulence models, where the predicted pressures are divided by the centerline pressure,  $p_c$ . Except for the RNG  $k - \epsilon$  turbulence model, the remaining turbulence models predict a nearly constant pressure within the core flow region. Furthermore, the standard  $k - \epsilon$ , the RNG  $k - \epsilon$ , and SST  $k - \omega$  turbulence models predict an increase in the reversed flow region as previously observed. In addition, the standard  $k - \epsilon$  and SST  $k - \omega$  turbulence models predict the same location of the starting edge of the separated boundary layer, where the observed constant core flow pressure starts to decrease as seen in figure 48. By closely observing the predictions obtained with the RNG  $k - \epsilon$ , this turbulence model also predicts the decrease of the pressure at the same location in the shroud region, i.e. the beginning of the separated boundary layer. The pressure decreases across the separated boundary layer before increasing at the onset of the flow reversal. The Spalart-Allmaras turbulence model shows a constant value across the cross section since it did not predict flow reversal. These predictions have been compared to the experimental distribution, which is the arithmetic mean value of the axial distribution of pressure recovery coefficients measured along the shroud and the hub. Equation (82) is the estimated frictionless pressure-recovery coefficient, obtained from the incompressible Bernoulli equation, giving the diffuser performance in terms

a basic diffuser design parameter, the area ratio  $AR = A_2/A_1 = 1.9$ . This area ratio concerns only the annular diffuser portion of the hybrid GT exhaust diffuser.

$$C_{p,frictionless} = 1 - \left(\frac{1}{AR}\right)^2 = 1 - \left(\frac{1}{1.9}\right)^2 = 0.72 \quad (82)$$

This theoretical value assumes nearly full pressure head recovery of the flow. However, for a value of  $x^* = 0.1$ , representing the length of the annular diffuser portion, experimental data show only a very low value of the pressure recovery coefficient around 0.2. The main reasons for this low value, compared to the ideal one, are the flow separation and reversal observed in the diffuser, due to increasing unfavorable pressure gradient, causing the viscous boundary layers to break away from the diffuser casing wall and to significantly reduce the annular diffuser performance. The present CFD analysis well predicts this behavior as can be seen on figure 49. Another important parameter explaining the low value of the pressure recovery coefficient is the inlet boundary layer blockage factor,  $B_t = A_{BL}/A_1$ , which varies from 0.03 to 0.12. The parameter  $A_{BL}$  is the inlet wall area blocked by the retarded boundary layer flow. At the exit of the annular diffuser portion, the RNG  $k - \epsilon$  turbulence model predicts a better value compared to the standard  $k - \epsilon$  and SST  $k - \omega$  turbulence models with a value of about 0.35. All the turbulence models overpredict the pressure recovery coefficient compared to experimental data. However, they predict values close to the ideal data from the inlet of the annular diffuser up to  $x^* = 0.03$ . The ideal pressure recovery coefficient was obtained by assuming a one-dimensional inviscid flow in the annular diffuser giving a value of 0.75 at its exit [27].

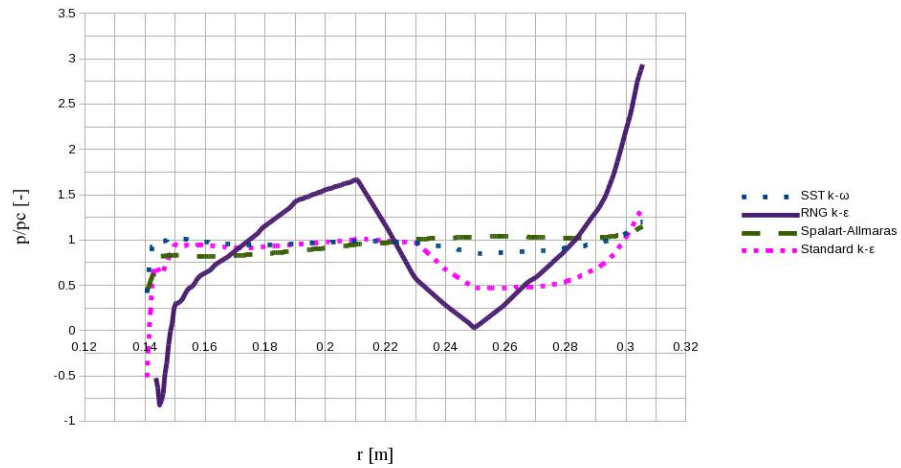


Figure 48: Reduced pressure distributions at station 04 function of turbulence models

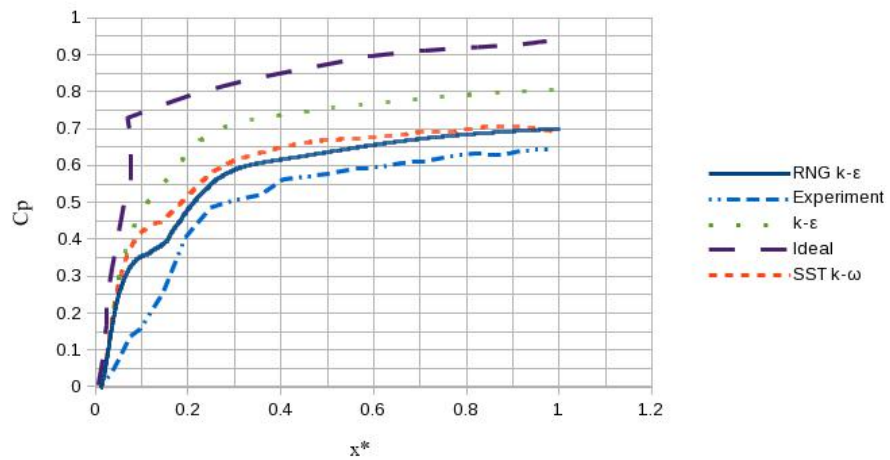


Figure 49: Axial distributions of pressure recovery coefficients varying turbulence models

Along the conical portion of the investigated diffuser, the pressure recovery coefficient profiles predicted by two of the considered turbulence models, i.e. the RNG  $k - \epsilon$  and the SST  $k - \omega$  turbulence models closely converge to a  $C_p$  value of 0.70 at the exit against 0.65 from experiment, which is an overprediction of 7%. On the contrary, the standard  $k - \epsilon$  ostensibly overpredicts values midway between the ideal and the experimental profiles, leaning more towards the ideal profile at the inlet portion of the conical diffuser. The results show that the OpenFOAM RNG  $k - \epsilon$  turbulence model slightly overpredicts results closer to experiment than the OpenFOAM SST  $k - \omega$  turbulence model.

#### 5.4 The Effects of Inlet Turbulence Intensity Variations on the Flow Characteristics

In this section we are considering the change in turbulence intensity at the diffuser inlet, and its impact on the axial velocity profile, the turbulence kinetic energy, the flow-field turbulence intensity, and the pressure recovery coefficient. Eight different turbulence intensity values have been considered in these studies, i.e., 1%, 1.5%, 2%, 3%, 5%, 6%, 7.5%, and 10%. These cases were run using the RNG  $k - \epsilon$  turbulence model with a mesh resolution of 17,505,415 cells, as this turbulence model gave us the best prediction of pressure recovery. Additionally, this turbulence model was the only one that showed robustness, i.e. performed without failure over a wide range of values and conditions using the same mesh, except for the turbulence intensity of 1%, which gave unrealistic convergence. The turbulence intensity of 3% was the baseline value used with all the turbulence models tested in these investigations. As

shown in figure 50, the computation overpredicts the maximum value of the axial velocity in the diffuser channel for values of turbulence intensity below 7%. However, for values of turbulence intensity above 7%, viz. 7.5%, and 10%, the maximum axial velocity is underpredicted and the flow remains attached to the casing wall, with no flow reversal. However, this is not unexpected as a high level of TI enhances momentum exchange in the flow which, in turn, delays the flow separation. This leads to a conjecture, similar to circular cylinder drag crisis phenomenon, that there exists an optimal turbulence intensity at which the turbulence losses are offset by longer flow attachment, and thus a better pressure recovery within a shorter diffuser. Analyses to be presented later appears to support this conjecture. It can thus be concluded that higher values of turbulence intensity allow a stabilization of the flow. It can be seen that towards the diffuser casing, above 69% of the flow passage height, the effect of varying the turbulence intensity depend on whether the turbulence intensity value is below or above 7%, with all the predictions coalescing in either case. At 50% of the annular diffuser and for turbulence intensity below 7%, the change of turbulence intensity does not change the size of the reversed flow region, which occupies 15% of the flow passage, about 20 mm, even though the magnitude of the reversed axial velocity changes very slightly. The maximum value of the axial velocity profile will be reduced for high values of turbulence intensity.

Now, let us consider the effect of varying the inlet turbulence intensity on the turbulent kinetic energy. The results are represented on figure 51 and compared to experimental data. It is clear that for inlet turbulence intensities of 7.5% and 10%, the turbulent kinetic energy profiles visibly departure from the experiment trend.

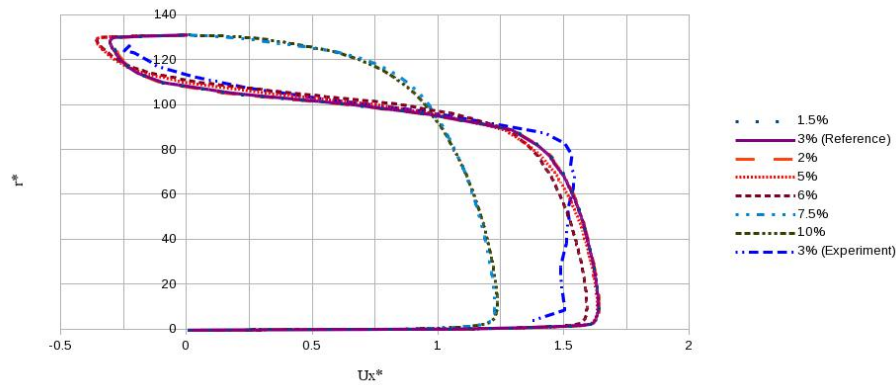


Figure 50: Axial velocities at  $x/h_1 = 1.01$ , 50 % annular diffuser varying inlet turbulence intensity

The change in the TKE profile shape actually starts with a value of inlet turbulence intensity around 5%; although both 5% and 6% display peak values at slightly the same location as experimental data, with values almost one third of the experimental one. In the region right after the hub boundary layer, the values are overpredicted compared to experiment starting from a turbulence intensity of 3% to 10%. However, the turbulent kinetic energy values are underpredicted for values of 2% and 1.5%. Reducing the inlet turbulence intensity below 3% reduces the turbulent kinetic energy in the core flow region, which displays constant values. The values in the region closer to the diffuser casing are sensibly the same as for an inlet turbulence intensity of 3%. Towards the diffuser casing region, starting from the casing separated boundary layer, the RNG  $k - \epsilon$  as well as all the investigated turbulence models underpredict the turbulent kinetic energy, even when the inlet turbulence intensity is varied up to the investigated value of 10%.

The effect of inlet turbulence intensity variations on the flow-field turbulence intensity distribution at 50% annular diffuser is considered next. It has been observed from

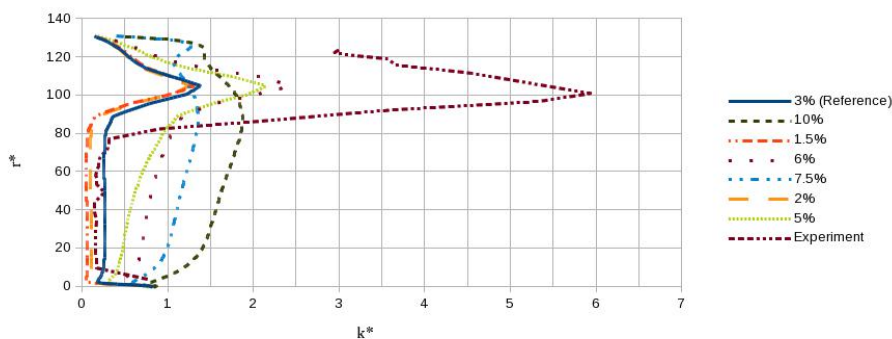


Figure 51: RNG  $k$ - $\epsilon$  normalized turbulent kinetic energy distributions at  $x/h_1 = 1.01$ , 50 % annular diffuser varying inlet turbulence intensity

figure 52 that the maximum value of the turbulence intensity, when varying its inlet value, occurs sensibly at the same diffuser channel height location for all inlet values below about 7%, with a very sharp peak of the turbulence intensity profiles. This maximum is the same for all inlet turbulence intensities below 3% and increases with values between 3% and 7%. But above a turbulence intensity of 7%, the maximum drops and display a dull peak. The different values at the hub, however, are almost the same for all inlet turbulence intensities, depending on whether the inlet turbulence intensity is above or below 7%, with the same observation applicable at the casing. It can also be observed that in the core flow, in spite of the fact that the turbulence intensity profile at a specific diffuser length location varies with the inlet turbulence intensity, the values tend to stay constant outside the boundary layer to a certain channel heighth, for turbulence intensities below 3%. For turbulence intensities above 3%, the values increase with channel height and then drop towards the casing after reaching a maximum. Within the boundary layer, the turbulence intensity decreases from the hub before slightly peaking up, and remains constant as specified earlier

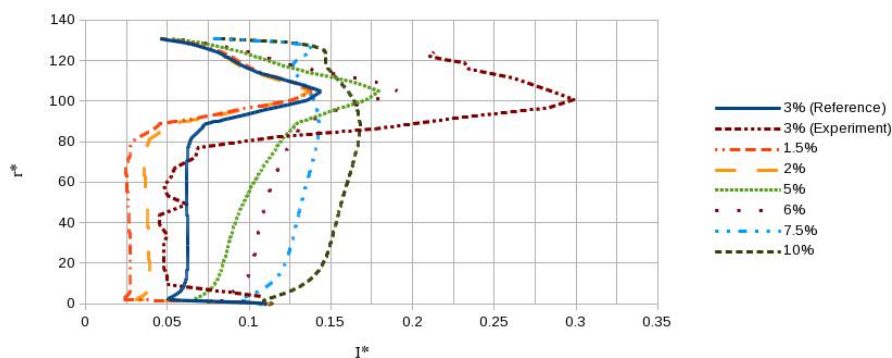


Figure 52: RNG  $k-\epsilon$  normalized turbulence intensity distributions at  $x/h_1 = 1.01$ , 50 % annular diffuser varying inlet turbulence intensity

for values below 3%. The turbulence intensity then increases sharply in the casing boundary layer followed by a drop from the velocity profile point of inflection to the wall. It has been observed that as long as we have a sharp peak of the turbulence intensity in this region, the flow reversal will occur at the casing. However, if the turbulence intensity profile displays a dull peak in the diffuser casing region, the flow reversal is suppressed. The peak values for our CFD predictions are lower than the experimental value.

In figure 53, we are going to consider the effect of varying the turbulence intensity on the pressure recovery coefficient, still using the RNG  $k - \epsilon$  turbulence model. It has been observed that for low values of turbulence intensities, the predicted pressure recovery coefficients tend to be high compared to experimental values. They decrease as the turbulence intensity increases up to about 5% before the pressure recovery coefficient starts to increase anew. The ideal turbulence intensity giving a closer agreement to experimental results is vraiseemblably located around 4%. The value of the turbulence intensity of 5% actually was the only one that undepredicted the

pressure recovery coefficient in the conical portion of the diffuser, while all other values overpredicted the recovery up to a reduced diffuser length  $x^* = 0.2$ . In the annular diffuser all predictions varying the turbulence intensity collapse from the diffuser inlet to 50% of the annular diffuser, where separation and reversal have been observed for most cases. In general, it has been observed that lower values and higher values tend to overpredict the recovery. For the studied diffuser configuration with a high opening angle, it is observed that increasing turbulence intensity to about 7.5% actually increases the diffuser performance by increasing the pressure recovery coefficient. An increase of 42% has been observed in the annular diffuser, characterized by lower values of  $C_p$ , going from a pressure recovery coefficient of about 0.35 to 0.50, which is a major increase. At the exit of the conical diffuser, a 14% increase has been observed with  $C_p$  changing from 0.66 to 0.75. However, if the turbulence intensity is increased above 7.5%, 10% for example, the performance decreases. Thus, means of generating increased turbulence in the casing boundary layer region can be devised so that this short exhaust diffuser can be used more efficiently. In this situation, increased TKE stabilizes the boundary layer so that it does not separate.

### 5.5 The Effects of Inlet Temperature on the Flow Characteristics

We are now considering the effects of the diffuser inlet temperature change on the flow characteristics, at 50% annular diffuser length, starting with the impact on the velocity profile. For this purpose, three isothermal cases were run using respectively 15, 227, and 427°C fluid-flow temperatures. In conformity with the continuity equation, the mass flow rate of 6 kg/s was kept constant, and an inlet turbulence intensity

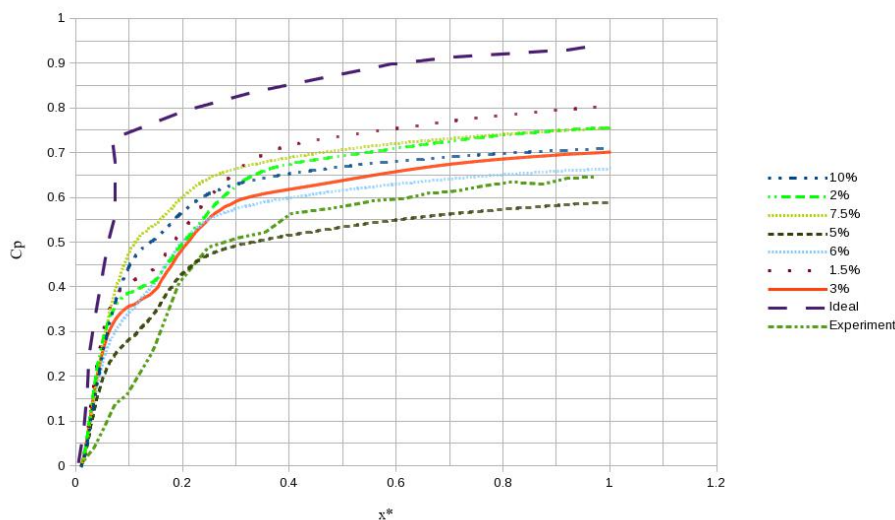


Figure 53: Axial distribution of pressure recovery coefficients varying turbulence intensities

of 3% was considered for all three cases. The fluid density and kinematic viscosity, however, were varied with temperature, and consequently the flow velocity and the Reynolds number. The results of the three isothermal CFD computations represented in figure 54 show that non-dimensionalized velocity profiles perfectly match and overlap. However, when plotting the dimensionalized velocity profiles shown in figure 55, it has been observed that, although the velocity magnitudes changed based on temperature, all three simulations predicted the same size of the separation region as well as the thickness of the separated boundary layer.

In changing the temperature, an effort was made to keep the flow as incompressible in all our numerical simulations. A numerical integration of the resulted velocity profiles for the simulated flow temperatures, respectively gave the following mass flow rates 5.92 kg/s , and 6.02 kg/s. These results match the constant reference value of 6 kg/s, with a margin of error of less than 1.3%. Figure 55 shows that the velocity

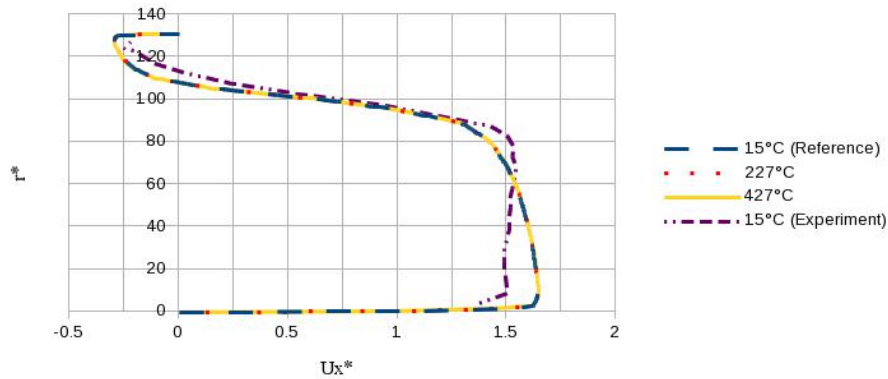


Figure 54: RNG  $k-\epsilon$  normalized axial velocity distributions at  $x/h_1 = 1.01$ , 50 % annular diffuser varying inlet temperature

magnitude in the reversed flow region at the casing also changed with temperature, while the three predictions clearly reproduced the same size of the separation region. For a temperature change of about fifteen times the initial temperature, the velocity almost doubled in order to keep the same mass flow rate, and thus satisfy the continuity equation. This observation is made for both the core and the shroud reversed flow regions. It is important to look at the performance of the diffuser, namely the pressure recovery coefficient, as will be done later, to see whether it is affected by a drastic change in temperature. As noticed previously, at the maximum velocity in the core flow region, a vertical and constant-value velocity profiles failed to be reproduced as obtained experimentally. However, contrary to the experiment where it is difficult to measure very closer to the wall, CFD predictions produced values in these near-wall regions, showing its potentialities where physical access is prohibited. In the next step we are going to consider how the turbulent kinetic energy profiles changed with varying inlet temperature, followed by its effect on the pressure recovery coefficient. Using the experimental results as reference, figure 56 shows the distribu-

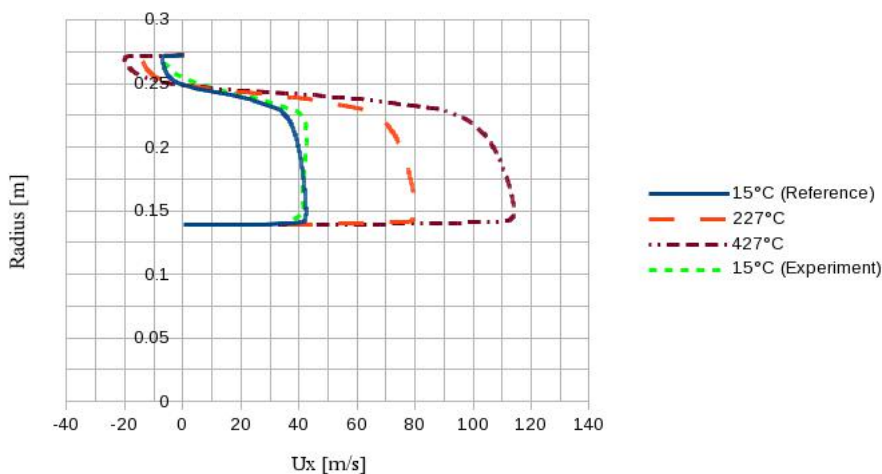


Figure 55: RNG  $k-\epsilon$  axial velocity distributions at  $x/h_1 = 1.01$ , 50 % annular diffuser varying inlet temperature

tions of turbulent kinetic energy at 50% annular diffuser using the robust RNG  $k - \epsilon$  turbulence model.

Clearly it can be seen in figure 56 that the turbulent kinetic energy significantly increased with increasing temperature. The TKE predictions show a big increase of about four times, in its maximum value, in the separated boundary layer and at the hub wall. The values at the casing wall being considerably lower than at the hub. On the contrary, with the change in inlet temperature, the turbulent kinetic energy did not change much in the core flow region, where the profiles remain sensibly constant from outside the hub boundary layer to about 70% of the diffuser channel height. It can be seen that as the temperature gets very high, the TKE profile starts to slide down, but the size of the core flow region of constant value remained the same as well as the thickness of the separated boundary layer, for all the considered temperatures. In general, the RNG turbulence model slightly overpredicts the turbulent kinetic

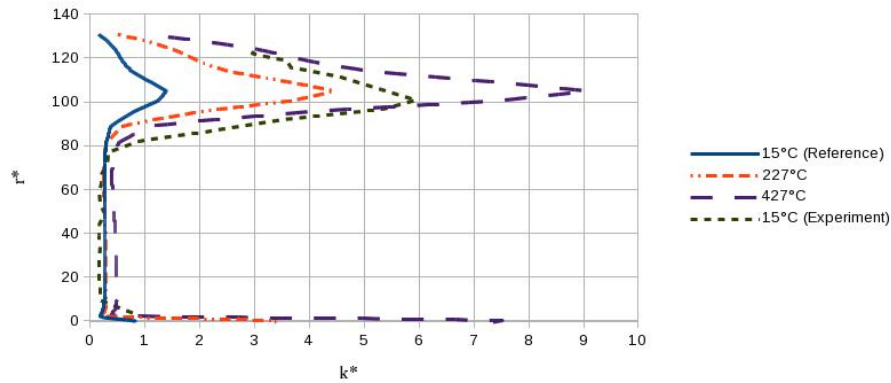


Figure 56: RNG turbulent kinetic energy distributions at  $x/h_1 = 1.01$ , 50 % annular diffuser varying inlet temperature

energy in the core flow region even though the predictions are reasonably in good agreement with experimental data. The high values of the turbulent kinetic energy at the hub wall sharply drop inside the subsequent thin boundary layer before becoming constant. The predictions show that the location of the maximum turbulent kinetic energy remains the same for all considered temperatures, about 80% of the diffuser channel height and within the casing separated boundary layer. As concluded before, the turbulence intensity profiles should display exactly the same trend as the turbulent kinetic energy since they are related mathematically just by a factor.

The pressure recovery coefficient throughout the diffuser, varying inlet temperature has also been investigated. When the temperature varies, a certain number of parameters will also vary, among which we have the volumetric flow rate, which usually increases with the temperature. The computed values changed from about  $4.9 \text{ m}^3\text{s}^{-1}$  for a reference  $15^\circ\text{C}$  temperature to  $8.49 \text{ m}^3\text{s}^{-1}$  at  $227^\circ\text{C}$ , and  $11.886 \text{ m}^3\text{s}^{-1}$  for  $427^\circ\text{C}$ . Since the inlet cross section does not change, from the volumetric flow rate equation, the velocity will increase with an increase in the volumetric flow rate, but the mass

flow rate will remain the same due to the decrease in the fluid density with increasing temperature. In figure 57, the pressure recovery coefficient profiles are plotted as a function of fluid temperature, and compared to the experimental and ideal pressure recovery coefficient profiles.

For the two increased temperatures considered, the pressure recovery coefficient profiles coincide with the 15°C pressure recovery coefficient profile. With these findings, it has been concluded that the increase of the fluid temperature has no effect on the gas turbine exhaust diffuser performance, expressed through the pressure recovery coefficient. When calculating the pressure recovery coefficient at the middle of the diffuser channel, it is important to note that with increasing temperature,  $C_p$ , must be evaluated using the numerically predicted static pressures and total pressure at the sampling station considered from the diffuser inlet to outlet as expressed by equation (83).

$$C_p = \frac{p_2 - p_1}{p_{tot1} - p_1}, \quad (83)$$

At higher temperatures and thus higher inlet velocities, considering the available initial kinetic energy or dynamic pressure,  $q_1$  in the denominator, at the diffuser inlet is misleading since the final predicted inlet velocity profile is not uniform. Using the available inlet dynamic pressure for a 15°C fluid-flow temperature slightly overpredicted the pressure recovery coefficient, leading to a calculation error of about 3%. When the temperature is significantly increased as in the current investigations, this error also grows to the point of predicting  $C_p$  values above 1, which is unrealistic.

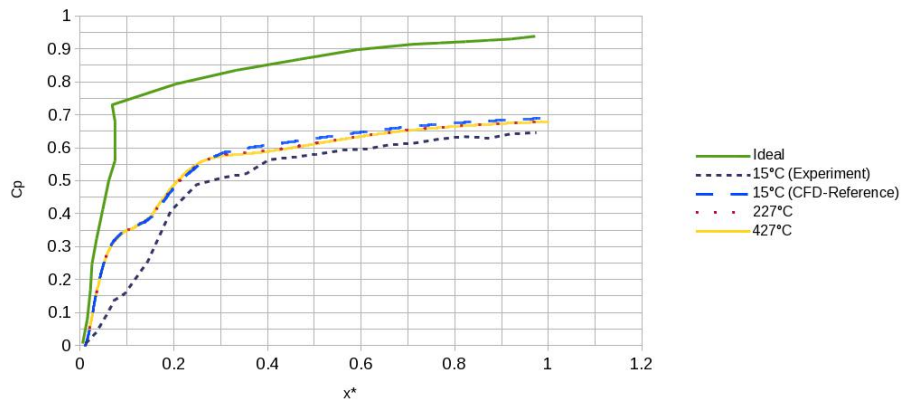


Figure 57: Axial distributions of pressure recovery coefficient varying inlet temperature

Figure 58 shows the axial variation of the TKE predicted by the three turbulence models. The RNG  $k - \epsilon$  and the SST  $k - \omega$  predict higher values of the TKE at the backward-facing step, with the former predicting persisting higher values than the latter in the conical portion of the diffuser. This confirms the higher values of the pressure recovery coefficient predicted by the RNG  $k - \epsilon$  turbulence model. However, the SST  $k - \omega$  turbulence model predicts fluctuating values of the TKE as in the case of the vorticity predictions. The RNG  $k - \epsilon$  and the SST  $k - \epsilon$  predict smoothly decreasing TKE profiles. In the annular portion of the exhaust diffuser, both  $k - \epsilon$  models predict a steady decrease of the TKE along the annular diffuser length.

In the next section, we are going to consider the effect of changing the inlet flow angle on the velocity, the turbulent kinetic energy, and the pressure recovery coefficient profiles at 50% annular diffuser length.

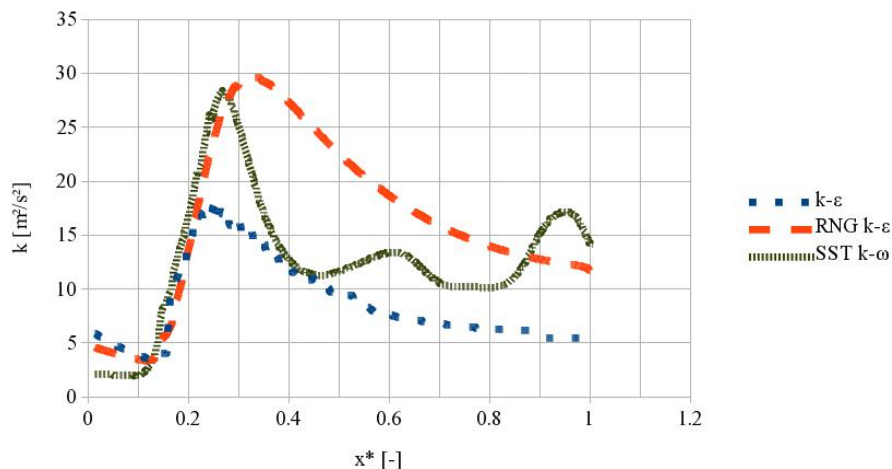


Figure 58: Axial variations of the TKE varying the turbulence models

### 5.6 The Effects of Velocity Inlet Angle on the Flow Characteristics

The effect of the velocity inlet angle on the exhaust diffuser flow characteristics is being analyzed in this section. Let us first consider the effects of adding one or two inlet velocity radial components on the axial velocity distribution, using a  $15^\circ$  velocity inlet angle, as shown in figure 59. It can be observed that using some configurations of velocity radial components with this specific inlet angle, a range of axial velocity profiles have been predicted that are clearly different from the one obtained from experiment. One striking observation made is that a vertical velocity profile in the core flow region has been predicted by adding a positive y-radial component or a combination of positive y- and z-radial components. This observation infers that, in a numerical simulation, an actual appropriate angle of inlet velocity coupled with some inlet swirl may generate a vertical velocity profile in the core flow region as observed experimentally, which was not predicted using simple uniform inlet conditions.

With these two radial component configurations, the figure shows that the flow

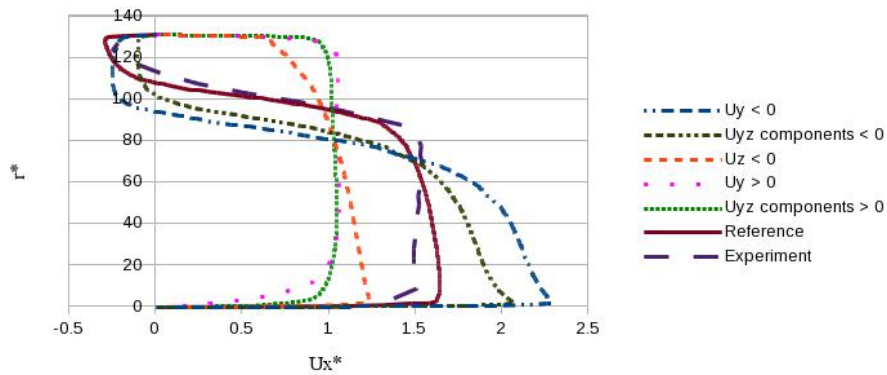


Figure 59: Normalized axial velocity distributions at  $x/h_1 = 1.01$ , 50% annular diffuser length by adding radial inlet velocity components

reversal has been suppressed at the casing, predicting a boundary layer velocity profile similar to that obtained at the diffuser hub. Furthermore, the velocity magnitude in the vertical portion of the velocity profile has been seriously underpredicted to about 66% of the experimental value. Figure 59 also shows that when considering a negative  $y$ -velocity component, a velocity profile overpredicting velocity in the core flow region is produced. Under this condition, the shroud separated boundary layer is moved towards the core flow region, and the predicted velocity profile is parallel to the experimental profile, substantially underpredicting the velocity and increasing the size of the reversed flow region. It is important to recall here that in order to obtain reliable CFD predictions, it is critical to endeavor to properly model boundary conditions as close as possible to the conditions existing in real life situations, and these can be obtained through accurate measurements.

When considering an inlet velocity angle, predictions in figure 60 show that the turbulence kinetic energy peak tends to become less prominent, and even flattens when flow reversal is suppressed, with high values occurring at the walls. On the

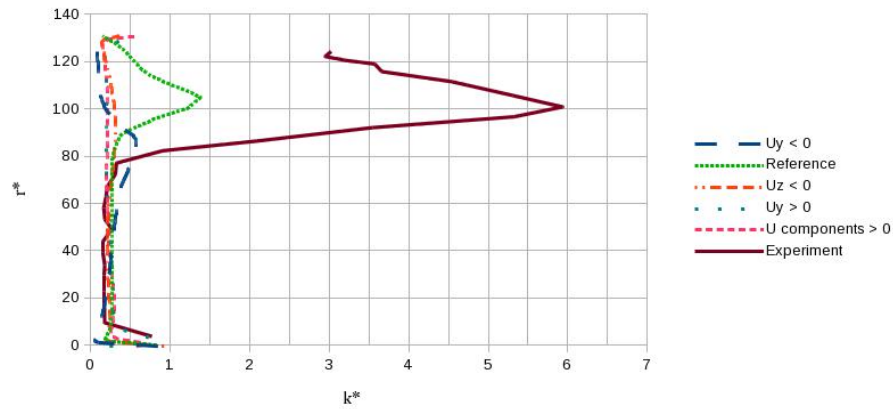


Figure 60: Normalized turbulence kinetic energy at  $x/h_1 = 1.01, 50\%$  annular diffuser length adding radial inlet velocity components

contrary, whenever flow reversal is predicted, the turbulence kinetic energy displays a peak, that becomes very sharp with zero inlet flow angle and uniform conditions. The turbulent kinetic energy in the core flow region does not vary much with inlet velocity angle consideration, though CFD predictions using the RNG  $k-\epsilon$  turbulence model are slightly above experiment data.

Figure 61 represents the axial distributions of the pressure recovery coefficient varying radial velocities at the diffuser inlet. In all the different simulations, the stream-wise velocity component at the inlet, i.e. in x-direction, has been maintained positive and we considered the radial components of the inlet velocity in the y- and/or z-directions. For a 3-dimensional simulation, with positive radial velocity components, relatively higher predictions of the pressure recovery coefficient have been observed compared to the case where both radial components are kept negative; however, those predictions are below experimental results. Let us consider two cases; one in which the y-velocity component is positive and the z-velocity component is kept equal to

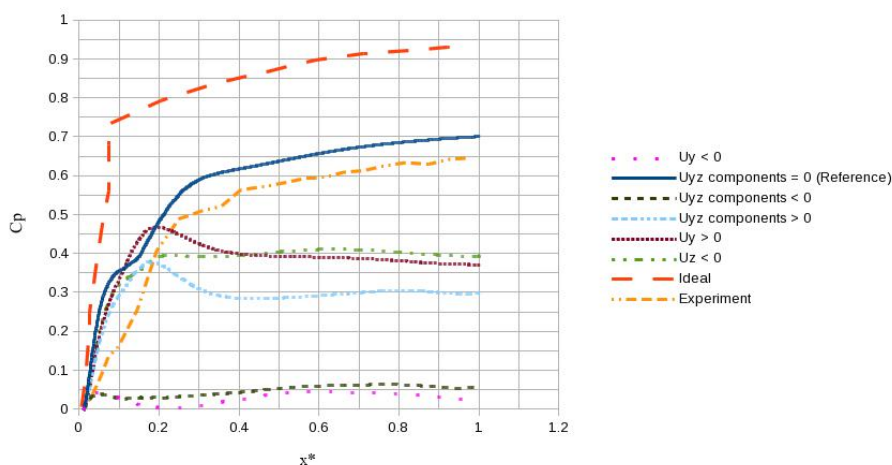


Figure 61: Axial distribution of pressure recovery coefficients adding radial inlet velocity components

zero. In the second one, the  $z$ -velocity component is negative and the  $y$ -velocity component is zero. The two cases produce relatively high values of the pressure recovery coefficient compared to a case where the  $y$ -velocity component is negative and  $z$ -component equal to zero. Also the combination of the positive  $y$ - and  $z$ -velocity components produces a lower value of the pressure recovery coefficient than when only the positive  $y$ -velocity component was used. This analyse suggests that the combination that would produce a relatively high value of the pressure recovery coefficient should be made of combination of positive  $y$ -velocity component and negative  $z$ -velocity component. Besides, the fact that the predicted pressure recovery coefficient with only the streamwise velocity component is close to experimental results suggests that the actual inlet velocity angle is probably very low, and possibly below the  $15^\circ$  angle considered in these investigations.

Figure 62 shows distributions of the pressure recovery coefficient when only one radial component of velocity, positive or negative, is considered. The predicted results

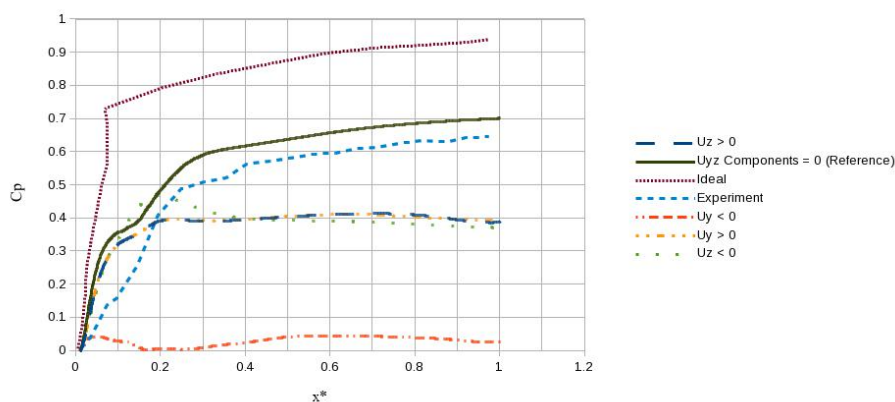


Figure 62: Axial distribution of pressure recovery coefficients considering one radial velocity component

show that positive y- or z-velocity radial component results are sensibly identical. The negative z-velocity component also produces identical results, except in the region right after the inlet of the conical portion of the hybrid diffuser, where values of the pressure recovery coefficient are a bit higher before coalescing with results of positive radial velocity components. The negative y-velocity component considerably reduces the pressure recovery coefficient to value less than 0.05. This component should thus be avoided when including radial velocity components of the diffuser inlet velocity.

Let us next consider four cases represented in figure 63, each using a specific combination of positive and/or negative radial velocity components. As before, the positive streamwise x-velocity is used in all the cases. The results are compared with experimental data considered as a reference case, with zero radial velocity components, and the ideal pressure recovery coefficient profile. As earlier, it can be seen that relatively higher predictions are obtained with cases where the y-velocity component is positive. Furthermore, when the negative y-velocity component is considered, the pressure recovery coefficient predictions are very low, underpredicted throughout the

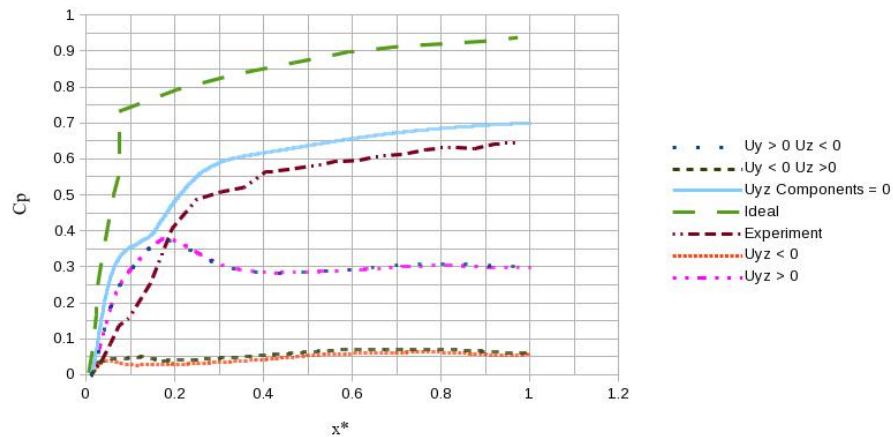


Figure 63: Axial distribution of pressure recovery coefficients considering both radial velocity component

whole hybrid diffuser from the annular to the conical portions. Combining all the observations on the angular orientation of the diffuser inlet velocity, it can be concluded that in a 3-dimensional case, relatively lower values of the pressure recovery coefficient are predicted every time the radial  $y$ -velocity component is negative.

In figure 64, axial distributions of the pressure recovery coefficient are plotted varying the inlet velocity angle from  $0$  to  $15^\circ$ . In the annular diffuser part, the computed pressure recovery coefficient is overpredicted for all considered angles. However, CFD results show that as the inlet angle increases the pressure recovery coefficient in the conical part starts to decrease, and is underpredicted for higher values of inlet velocity angle, here between  $7$  and  $15^\circ$ . In general, it is concluded that increasing inlet velocity angle above a certain angle, say  $6^\circ$ , will decrease the diffuser performance considerably. For small angles close to zero, i.e.  $0$  to  $3^\circ$ , the CFD results using the RNG  $k - \epsilon$  turbulence model do not change much in the conical as well as in the annular diffusers. Compared to a  $0^\circ$  inlet velocity angle, it is observed, however, that

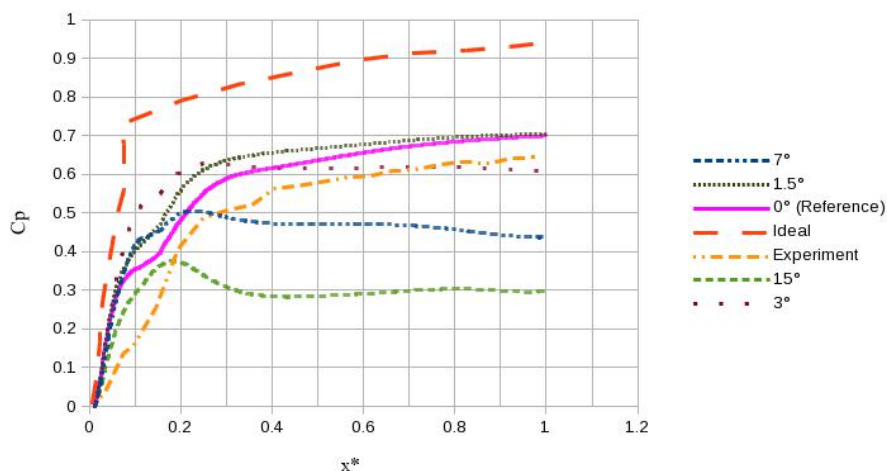


Figure 64: Axial distribution of pressure recovery coefficients varying inlet velocity angle

for these angles, the predicted pressure recovery coefficient is higher in the region of the annular diffuser exit and the inlet of the conical portion. From the velocity inlet angle of  $3^\circ$  and above, the pressure recovery coefficient tends to remain constant in the last portion of the conical diffuser, i.e. about 60 percent of the conical diffuser length. Another observation is that, at the inlet of the exhaust diffuser, all the CFD predictions collapse, and the pressure recovery coefficient increases linearly before displaying a kink region in the profile. From the diffuser inlet velocity angle analysis, the optimum value producing reasonable pressure recovery coefficient predictions is located between  $2$  and  $2.5^\circ$ .

## CHAPTER 6: CONCLUSIONS

Nowadays, gas turbines, GT, are widely used in electric power generation to provide mechanical power necessary to drive power plant alternators, and electricity is in great demand in many aspects of life worldwide. This growing world demand in energy challenges engineers to devise new ways of increasing GT efficiency and reduce the carbon footprint on the environment. The overall efficiency of a combined-cycle GT can be enhanced by improving the performance of some of its individual components, among which the GT turbine exhaust diffuser. The performance of a GT exhaust diffuser, in terms of the pressure recovery coefficient, is a function of the diffuser geometry and inlet flow characteristics. Improving the exhaust diffuser performance by increasing the pressure recovery produces a much lower pressure at the turbine exit, resulting in an increase of the GT output work, and consequently an increase in its thermal efficiency. However, the flow at the inlet of the exhaust diffuser, generated by the GT last stage, is very complex, i.e. turbulent, distorted, unsteady, with non-uniform flow properties. Furthermore, complicated flow patterns and conditions inside a diffusing subsonic duct, characterized by separation, backflow, and unsteadiness make the mathematical or theoretical analysis very complicated, since the theory of the turbulent flow condition in a tapered diameter duct, for which the tapered flow does not become fully developed, is not well formulated.

For this purpose, the diffuser angle of divergence as well as several inlet flow param-

ters, known to influence the diffuser performance, have been identified and numerical investigations to predict their effects on a typical annular-conical exhaust diffuser flow-field behavior and properties, were conducted. Computational fluid dynamics, CFD, has been used to calculate the flow field inside this hybrid diffuser characterized by a very large diverging angle,  $40^\circ$ .

In reviewing the relevant literature, it has been observed that the data on the effects of varying the turbine exit flow turbulence characteristics, the temperature, as well as the flow angularity at the inlet of the exhaust diffuser were scant. The current studies sought to further gain a better understanding of the influence of these parameters on a typical GT annular-conical exhaust diffuser performance. The investigations also sought to evaluate the simplified numerical approach using uniform inlet flow conditions compared to real-life inlet conditions of the experimentation, especially in effectively predicting of the pressure recovery coefficient. The accuracy of selected turbulence models were tested by comparing predicted flow characteristics such as the velocity profiles, static pressure recoveries, the turbulent kinetic energy distributions, and the turbulence intensity distributions at specific locations of the diffuser length to experimental results. Some additional numerical issues associated with discretization had to be specifically considered such as consistency and stability, which are necessary and sufficient conditions for convergence. Results from extensive experimental studies, previously subjected to a diffuser test rig at the Leibniz university of Hannover in Germany, were used to validate the adopted numerical approach. The obtained numerical results and relevant information could be used toward the design of an optimum annular-conical diffuser, for performance improve-

ment of combined-cycle gas turbines. The investigation procedures took advantage of the free CFD software OpenFOAM, to assess its embedded flow physics models and its potentials in cutting CFD analyses costs by users in industry as well as in academia.

Four major objectives were set as follows:

- Perform initial CFD analyses based on experimental investigations involving an exhaust diffuser using the standard  $k - \epsilon$  turbulence model,
- Establish the fidelity of the CFD approach through results validation,
- Test the accuracy of additional selected turbulence models,
- Carry out additional simulations by varying selected diffuser inflow parameters.

These introductory remarks shall be followed by some limitations in the research defining the research scope, followed by a discussion of the keys findings. The dissertation will end with some recommendations of future research works.

## 6.1 Research Limitations

A more simple version of the diffuser geometry used in the test rig investigations at the Leibniz university of Hannover, and uniform inlet flow properties were considered in this numerical analysis. The numerical approach consisted of isothermal and incompressible steady-state turbulent flow investigations, testing only some eddy-viscosity turbulence models. In order to satisfy the continuity equation, the mass flow rate was kept constant for all the numerical simulations.

## 6.2 Key Findings and Concluding Remarks

From a good agreement between the CFD simulations of the present study and the experiment , it appears that our simple, fast, and affordable steady-state CFD approach was able to predict with a reasonable accuracy the complicated flow-field inside a gas turbine featuring regions of adverse pressure gradients that caused flow separation and its reversal, flow recirculation at the backward-facing step, developing boundary layers with large gradient of flow properties normal to the flow direction, and streamline curvatures.

Due to the complex nature of the aforementioned flow-field conditions, special attention was given to the generation of the computational grid. Knowing the velocity profile from experiment results was instrumental in providing guidance for the mesh design. At 50% of the annular portion of the analyzed GT exhaust diffuser, available experimental data showed high velocity gradients near the walls, i.e. in the boundary layers, so that grading of the mesh for an optimum solution was required. A tremendous amount of work and time was spent at this phase to design a grid distribution that included very fine meshes, capable of predicting the actual flow-field behavior in those regions of high property gradients. In general, correctly meshing regions of high shear is very critical in achieving accurate numerical predictions of varying flow properties. The flow from the annular diffuser passing over the backward-facing step generated high shear on the fluid below that produced a standing vortex requiring fine mesh resolution for its accurate prediction.

The use of turbulence models enabled us to gain useful insights into the highly

turbulent and three-dimensional nature of the investigated diffuser flow. Four different regions of flow have been observed at 50% annular diffuser length measuring station. Of the four tested turbulence models, only the SST  $k - \omega$  turbulence model better predicted the size as well as the location of the separated boundary layer at the casing. It has been concluded that the thickness of the shroud boundary layer will vary with the diffuser opening angle until, for a specific high angle, a condition of jet flow regime is generated at the casing wall. The SST  $k - \omega$  turbulence model also predicted asymmetric diffuser flow, which seems to substantiate theoretical knowledge in the open literature. This asymmetry is mainly due to the non-uniformity of the velocity profile at the diffuser exit. The standard and the RNG  $k - \epsilon$  turbulence models equally under-predicted the size and the location of the separated boundary layer. The Spalart-Allmaras turbulence model did not, however, predict any flow separation or reversal at the casing. Despite using more than 15 prism layers to resolve the boundary layers, none of the used turbulence models was able predict the correct size of the hub boundary layer, and a vertical velocity profile in the core flow region. A better mesh distribution would probably resolve these two problems. To obtain credible predictions with the tested turbulence models and wall functions, an effort has been made to obtain  $y^+$  values within the range of applicability of the turbulence models. An average  $y^+ = 2$  has been achieved when using the SST  $k - \omega$  turbulence model, and  $y^+ = 9.8$  with the standard  $k - \epsilon$  turbulence model. The comparison between computed and measured velocity profiles at 50% of annular diffuser shows that these were poorly predicted in the core flow region of the flow. Overall, the SST  $k - \omega$  turbulence model, which combines advantages of the standard  $k - \epsilon$  and  $k - \omega$

turbulence models, showed better agreement with experimental data, in predicting the velocity profile, even though it slightly overpredicted the size and the velocity magnitude of the separated flow; it also closely predicted the separation point at the casing.

In predicting the TKE in regions of low TKE values, i.e. the diffuser core flow and the hub boundary layer where there is no separation or flow reversal, relatively good agreement with experiment has been obtained by all tested turbulence models, including those tested in David et al. numerical calculations [14]. However, all these turbulence models underpredicted the TKE in the casing boundary layer, and in the reversed flow region. An important conclusion has been reached about the location of the maximum TKE value in the separated boundary layer. It has been observed that this maximum was reached within the separated boundary layer at the velocity profile point of inflection where the upward concavity, which started from the casing reversed flow region, smoothly merges with the core flow velocity profile which has a downward concavity. This means that since the position of the casing boundary layer depends on the diffuser opening angle, the location of the maximum turbulent kinetic energy will also vary with this angle, moving this point downward as the opening angle increases. The TKE started to increase steadily in the reversed flow region until the velocity profile point of inflection is reached within the separated boundary layer, before starting to decrease sharply to reach a lower value in the core flow region where the velocity profile has its maximum value of the flow velocity. In the core flow region, the TKE did not vary much when considering the effects of the inlet flow velocity angle of  $15^\circ$ , by adding one or two radial components of velocity. However,

the TKE and the velocity magnitudes changed with increasing fluid temperatures in the reversed flow region at the casing and the subsequent separated boundary layer. Besides, changing the inlet turbulence intensity, for the considered diffuser opening angle, did not also change the location of the maximum turbulent kinetic energy for turbulence intensity values below 6%. The maximum value, however, increased with the increase of the turbulent intensity. For values of the turbulent intensity above 7%, the maximum TKE value started to decrease, and its location moved downward.

The flow reversal region at the casing, due to increasing pressure gradient, grew along the diffuser length, pushing the boundary layer away from the wall. The presence of the backward-facing step generated a fully developed vortex stretching into the conical portion of the diffuser, and a sudden increase of pressure that had affected flow reversal at the casing, as well as the non-uniformity of flow characteristics at the annular diffuser exit. The boundary layer separation and reversal due to high diffuser opening angle, coupled with the effects of the backward-facing step were the main reasons of diffuser stall losses and poor predictions of the annular diffuser performance. It was concluded that, with an inlet turbulence intensity of 3%, changing the inlet temperature did not have any effects on the size of the separated and reversed flow region, the position and thickness of the separated boundary layer, and consequently the velocity profile point of inflection. Therefore, the location of the maximum turbulent kinetic energy for a fixed value of the diffuser opening angle did not change. Numerical predictions by changing the turbulence intensity at the diffuser inlet, however, showed that for values above 7%, the flow separation at the casing was suppressed and the flow stabilized, with the maximum of the axial velocity reduced in

the core flow region. Yet, at 50% of the annular diffuser length and for values below 7%, the change of turbulence intensity did not change the size of the reversed flow region, while slightly increasing the velocity magnitude in the reversed flow region. In investigating the three-dimensional inlet flow velocity, it was concluded that the positive y-velocity component has a tendency to suppress the flow reversal at the diffuser casing, generating a flattened TKE profile.

Compared to the ideal value, the pressure recovery coefficient at the exit of the annular portion of the hybrid GT exhaust diffuser was found to be very low, both by experiment and numerical predictions. This fact may be explained by the non-uniformity of flow properties at the exit of the annular portion of the analyzed hybrid diffuser due to the observed flow phenomena generated by the diffuser high inclination angle. However, all the eddy-viscosity turbulence models were found to overpredict the pressure recovery coefficient, with the standard  $k - \epsilon$  turbulence model giving the worse predictions. The RNG  $k - \epsilon$  turbulence model better predicted the pressure recovery coefficient profile than the other two tested turbulence models. The study also showed that the turbulence intensity producing a pressure recovery profile closer to experiment was around 4%, and both lower and higher values tend to overpredict the pressure recovery coefficient. Therefore, setting the right turbulence intensity value in a CFD analysis is critical to obtaining accurate predictions of the flow characteristics. In considering radial components of inlet flow velocity, it was observed that relatively lower pressure recovery coefficients were predicted with negative y-velocity component. Nevertheless, to obtain a relatively high pressure recovery coefficient, the combination of positive y-velocity component and negative z-velocity component

is preferable, with a small inlet flow velocity angle, estimated in the present investigations between 2 and 2.5°. Furthermore, the inlet fluid temperature had no effect on the pressure recovery coefficient, with higher temperatures predicting pressure recoveries equal to the 15°C reference case.

The CFD analysis using OpenFOAM showed that predicted flow characteristics were dependent on the number of cells in the computational domain. The tested turbulence models were found to be very dissipative in the separated boundary layer as well as in the reversed flow region. For a geometry presenting different features at some locations that generate specific flow patterns, the accuracy of a turbulence model varied according to the specific physics of the flow pattern. It has been concluded that the diffuser opening angle has the most influence on the flow development and properties inside a GT exhaust diffuser. Inlet flow angularity as well as inlet turbulence also have influence of the diffuser flow. Therefore, adopting appropriate inlet velocity angle, turbulence characteristics, and an optimal diffuser angle of divergence, and designing a progressively diminishing hub diameter will improve the overall performance of the GT exhaust diffuser and ultimately the overall efficiency of the combined-cycle gas turbine.

### 6.3 Recommendations for Future Research

The demand in the world energy consumption and the need for highly performing GT to power all aspects of people lives will continue to grow as the world population increases. Consequently, there will still be a need for more research in this area to meet these challenges. In predicting radial-axial velocity distributions, the steady-

state calculation with SST turbulence model, as well as the unsteady calculation with SAS-SST model showed good agreement with the experimental LDV-measurement values in the middle of the annular diffuser, with the former giving a closer prediction of the separated region. Unsteady calculations is probably more suited to accurately predict diffuser flow characteristics. Following are some recommendations for future research that can shine some light on how we can improve diffuser performance for an overall efficiency improvement of combined-cycle gas turbines:

- Investigate other turbulence models than eddy-viscosity ones, such as the detached eddy simulations (DES),
- Perform similar investigations using inflow conditions similar to the gas turbine outflow, with a typical industrial gas turbine exhaust diffuser, exhibiting the essential characteristics including the presence of row of struts that would cause additional unsteady wakes in the flow field, and non-uniform outlet flow characteristics that can further affect diffuser performance,
- Investigate the change in turbulence models coefficients: The OpenFOAM  $C_{++}$  library is primarily used to create executables or applications. As an open-source CFD code, modifications to the code to explore the effects of changing turbulence coefficients may lead to more accurate turbulence models,
- Conduct non-isothermal simulations with different inlet temperatures to investigate their effects on the pressure recovery coefficient.

Analyses of the CFD results showed that the pressure recovery coefficient of the investigated diffuser was improved by increasing the inlet turbulence intensity and using a certain inlet flow angle. it was observed that increasing the inlet turbulence

intensity was accompanied by an increase in the level of turbulence observed in the casing boundary layer region. Thus, it is concluded that one way of improving the diffuser performance is to increase the level of turbulence in the inclined wall region that would suppress flow separation and reversal, and achieve a rapid and increased diffusion. One practical solution to this problem is to introduce a plan shear layer or mixing layer in this region that will generate a free turbulence. The mixing layer can be generated by injecting, at the diffuser entrance and through a splitter plate, a fluid stream of a different velocity. In examining the different types of existing diffuser solutions, this principle has been used by the vortex-controlled diffuser, which bleeds the boundary layer to produce the same effect.

## REFERENCES

- [1] R. C. Adkins, D. S. Matharu, and J. O. Yost. The hybrid diffuser. *Journal of Engineering for Power*, 103:229–236, 1981.
- [2] R. D. Blevins. *Applied Fluid Dynamics Handbook*. Van Nostrand-Reinhold, New York, 1984.
- [3] J. Carrotte, D. Bailey, and C. Frodsham. Detailed measurements on a modern dump diffuser. *Journal of Engineering for Gas Turbines and Power*, 117:678–685, 1995.
- [4] A. B. Cocanower, S. J. Kline, and J. P. Johnston. *A Unified Method for Predicting the Performance of Subsonic Diffusers of Several Geometries*. Stanford University PD-10, 1965.
- [5] D. L. Cochran and S. J. Kline. The use of short flat vanes as a means for producing efficient wide-angle two-dimensional subsonic diffusers. *NACA TN 4309*, 1958.
- [6] G. K. Feldcamp and A. M. Birk. A study of modest cfd models for the design of an annular diffuser with struts for swirling flow. In *ASME Turbo Expo 2008: Power for Land, Sea, and Air*, volume 5:Turbo Expo 2008, Parts A and B, pages 1–10, 2008.
- [7] H. U. Fleige, W. Riess, and J. Seume. Swirl and tip leakage flow interaction with struts in axial diffusers. In *ASME Turbo Expo 2002: Power for Land, Sea, and Air*, volume 5:Turbo Expo 2002, Parts A and B, pages 871–878, 2002.
- [8] R. Hestermann, S. Kim, A. B. Khaleb, and S. Wittig. Flow field and performance characteristics of combustor diffusers: A basic study. *Journal of Engineering for Gas Turbines and Power*, 117:686–694, 1995.
- [9] J. Hoffmann and G. Gonzalez. Effects of small-scale, high intensity inlet turbulence on flow in a two-dimensional diffuser. *Journal of Fluids Engineering*, 106:121–124, 1984.
- [10] E. C. Inc. *CFD-ACE+ V2009.0 User Manual*. ESI-Group, 2008.
- [11] J. D. A. JR. *Computational Fluid Dynamics: The Basics With Applications*. McGraw-Hill, Inc, 1995.
- [12] A. Klein. Characteristics of combustor diffusers. *Progress in Aerospace Science*, 31:171–271, 1995.
- [13] S. Kline, D. Abbott, and R. Fox. Optimum design of straight-walled diffusers. *Journal of Basic Engineering*, 81:321–331, 1959.

- [14] D. Klub, H. Stoff, and A. Wiedermann. Effect of wakes and secondary flow on re-attachment of turbine exit annular diffuser flow. *Journal of Turbomachinery*, 131:041012–1–041012–12, 2009.
- [15] E. Kreyszig. *Advanced Engineering Mathematics*. John Wiley & Sons, Inc., 2006.
- [16] B. Lakshminarayana and B. Reynolds. Turbulence characteristics in the near wakes of a compressor rotor blade. *AIAA Journal*, 18:1354–1362, 1980.
- [17] A. H. Lefebvre and D. R. Ballal. *Gas Turbine Combustion: Alternative Fuels and Emissions*. CRC Press, New York, 2010.
- [18] O. Limited. *OpenFOAM, The Open Source CFD Toolbox*. OpenCFD Limited, 2011.
- [19] R. Lohmann, S. Markowski, and E. Brookman. Swirling flow through annular diffusers with conical walls. *Journal of Fluids Engineering*, 101:224–229, 1979.
- [20] F. R. Menter and Y. Egorov. Revisiting the turbulent length scale equation. *IU-TAM Symposium: One Hundred Years of Boundary Layer Research, Gottingen, Germany*, 2003.
- [21] F. R. Menter and Y. Egorov. A scale-adaptive simulation model using two-equation models. pages Paper No. AIAA–2005–1095, 2005.
- [22] F. R. Menter, M. Kuntz, and R. Bender. A scale-adaptive simulation model for turbulent flow prediction. *International Journal of Heat and Fluid Flow*, pages Paper No. AIAA–2003–0767, 2003.
- [23] C. Moore and S. Kline. Some effects of vanes and of turbulence in two-dimensional wide-angle subsonic diffusers. *NACA TN 4080*, 1958.
- [24] M. J. Moran, H. N. Shapiro, D. D. Boettner, and M. B. Bailey. *Fundamentals of Engineering Thermodynamics*. John Wiley & Sons, Inc., 2011.
- [25] R. L. Panton. *Incompressible Flow*. John Wiley and Sons, Inc., Hoboken, New Jersey, 2005.
- [26] A. M. Pradeep, B. Roy, V. V., and S. D. Study of gas turbine exhaust diffuser performance and its enhancement by shape modifications. In *ASME Turbo Expo 2010: Power for Land, Sea, and Air*, volume 7:Turbo Expo 2010, Parts A, B, and C, pages 1101–1110, 2010.
- [27] O. Sieker and J. R. Seume. Influence of rotating wakes on separation in turbine exhaust diffusers. *Journal of Thermal Science*, 17:42–49, 2008.
- [28] T. Sonoda, T. Arima, and M. Oana. The influence of downstream passage on the flow within an annular s-shaped duct. *Journal of Turbomachinery*, 120:714–722, 1998.

- [29] P. Spalart, W.-H. Jou, M. Strelets, and S. R. Allmaras. Comments on the feasibility of LES for wings, and on a hybrid/LES approach. *Advances in DNS/LES, First AFOSR International Conference on DNS/LES*, 1997.
- [30] S. Stevens and G. Williams. The influence of inlet conditions on the performance of annular diffusers. *Journal of Fluids Engineering*, 102:357–363, 1980.
- [31] S. J. Stevens. The performance of annular diffusers. *Poc Instn Mech Engrs*, 182:58–70, 1967–68.
- [32] B. K. Sultanian, S. Nagao, and T. Sakamoto. Experimental and three-dimensional CFD investigation in a gas turbine exhaust system. *Journal of Engineering for Gas Turbines and Power*, 121:364–374, 1999.
- [33] H. Tennekes and J. L. Lumley. *A First Course in Turbulence*. MIT Press, 1972.
- [34] D. Unger and H. Herzog. Comparative study on energy R & D performance: Gas turbine case study. Final report, Massachusetts Institute of Technology Energy Laboratory, August 1998. Prepared for Central Research Institute of Electric Power Industry.
- [35] V. Vassiliev, S. Irmisch, S. Abdel-Wahab, and A. Granovskiy. Impact of the inflow conditions on the heavy-duty gas turbine exhaust diffuser performance. *Journal of Turbomachinery*, 134:041018–1–041018–9, 2012.
- [36] V. Vassiliev, S. Irmisch, and M. Claridge. Experimental and numerical investigation of the impact of swirl on the performance of industrial gas turbines exhaust diffusers. In *ASME Turbo Expo 2003: Power for Land, Sea, and Air*, volume 6:Turbo Expo 2003, Parts A and B, pages 19–29, 2003.
- [37] V. Vassiliev, S. Irmisch, and S. Florjancic. CFD analysis of industrial gas turbine exhaust diffusers. In *ASME Turbo Expo 2003: Power for Land, Sea, and Air*, volume 5:Turbo Expo 2002, Parts A and B, pages 995–1013, 2002.
- [38] V. Vassiliev, N. Mooslechner, M. Kostege, and A. Granovskiy. Aerodynamic characteristics of a redesigned turbine. In *ASME Turbo Expo 2007: Power for Land, Sea, and Air*, volume 6:Turbo Expo 2007, Parts A and B, pages 609–619, 2007.
- [39] V. Vassiliev, M. Rothbrust, and S. Irmisch. Refitting of exhaust diffuser of industrial gas turbine. In *ASME Turbo Expo 2008: Power for Land, Sea, and Air*, volume 6:Turbo Expo 2008, Parts A, B, and C, pages 979–987, 2008.
- [40] H. K. Versteeg and W. Malalasekera. *An Introduction to Computational Fluid Dynamics: The Finite Volume Method*. Pearson Education Limited, Harlow, England, 2007.
- [41] F. M. White. *Viscous Fluid Flow*. Mc Graw Hill, New York, 2006.
- [42] F. M. White. *Fluid Mechanics*. Mc Graw Hill, New York, 2008.